

# ENERGY TRANSFER IN NANOSTRUCTURED MATERIALS

by

Chelsea Haughn

A dissertation submitted to the Faculty of the University of Delaware in partial fulfillment of the requirements for the degree of Doctor of Philosophy in Materials Science and Engineering

Fall 2014

© 2014 Chelsea Haughn  
All Rights Reserved

UMI Number: 3685115

All rights reserved

INFORMATION TO ALL USERS

The quality of this reproduction is dependent upon the quality of the copy submitted.

In the unlikely event that the author did not send a complete manuscript and there are missing pages, these will be noted. Also, if material had to be removed, a note will indicate the deletion.



UMI 3685115

Published by ProQuest LLC (2015). Copyright in the Dissertation held by the Author.

Microform Edition © ProQuest LLC.

All rights reserved. This work is protected against unauthorized copying under Title 17, United States Code



ProQuest LLC.  
789 East Eisenhower Parkway  
P.O. Box 1346  
Ann Arbor, MI 48106 - 1346

**ENERGY TRANSFER IN NANOSTRUCTURED MATERIALS**

by

Chelsea Haughn

Approved: \_\_\_\_\_

Darrin Pochan, Ph.D.

Chair of the Department of Materials Science and Engineering

Approved: \_\_\_\_\_

Babatunde Ogunnaike, Ph.D.

Dean of the College of Engineering

Approved: \_\_\_\_\_

James G. Richards, Ph.D.

Vice Provost for Graduate and Professional Education

I certify that I have read this dissertation and that in my opinion it meets the academic and professional standard required by the University as a dissertation for the degree of Doctor of Philosophy.

Signed: \_\_\_\_\_

Matt Doty, Ph.D.  
Professor in charge of dissertation

I certify that I have read this dissertation and that in my opinion it meets the academic and professional standard required by the University as a dissertation for the degree of Doctor of Philosophy.

Signed: \_\_\_\_\_

David Martin, Ph.D.  
Member of dissertation committee

I certify that I have read this dissertation and that in my opinion it meets the academic and professional standard required by the University as a dissertation for the degree of Doctor of Philosophy.

Signed: \_\_\_\_\_

Michael Mackay, Ph.D.  
Member of dissertation committee

I certify that I have read this dissertation and that in my opinion it meets the academic and professional standard required by the University as a dissertation for the degree of Doctor of Philosophy.

Signed: \_\_\_\_\_

James Kolodzey, Ph.D.  
Member of dissertation committee

## ACKNOWLEDGEMENTS

I would like to acknowledge Prof. Matthew Doty for advising and supporting me in this research. His mentorship and guidance have been invaluable in my development as a scientist. This dissertation could not have been completed without his instruction, encouragement and support. I would also like to acknowledge Prof. Bruce Chase, Prof. Robert Opila, and Prof. Joshua Zide for their discussions, thoughts and mentorship that have made this work possible. Additionally, I would like to acknowledge our collaborators: Dr. Kurt Eyink, Dr. Elizabeth Steenbergen, Dr. Luke Bissel, Chris Ebert, Dr. Allen Barnett, Dr. Ken Schmieder, Dr. Louise Bradley, Dr. Sylvain Cloutier, Dr. Fan Xu, Dr. Xin Ma, Graham Murphy. Also many thanks to the my colleagues and friends who made this journey not only enlightening but enjoyable: Dr. Diane Sellers, Dr. Weiwen Liu, Xinran Zhou, Laura Vanderhoef, Anagha Kulkarni, Eric Chen, Xiangyu Ma, Dr. Nicole Kotulak, and Nandita Bhagwhat.

## TABLE OF CONTENTS

<b>LIST OF TABLES</b> . . . . .	<b>viii</b>
<b>LIST OF FIGURES</b> . . . . .	<b>ix</b>
<b>ABSTRACT</b> . . . . .	<b>xiii</b>
 <b>Chapter</b>	
<b>1 INTRODUCTION</b> . . . . .	<b>1</b>
<b>2 OPTOELECTRONIC PROPERTIES OF SEMICONDUCTORS</b> .	<b>3</b>
2.1 Bulk Semiconductor Materials . . . . .	3
2.1.1 Fabrication . . . . .	3
2.1.1.1 Bulk Processes . . . . .	3
2.1.1.2 Epitaxial Processes . . . . .	4
2.1.2 Band structure . . . . .	6
2.1.3 Energy Transport & Loss in Bulk Materials . . . . .	9
2.1.3.1 Minority Carrier Lifetime . . . . .	10
2.1.3.2 Shockley-Read-Hall Recombination . . . . .	12
2.1.3.3 Debuf Model . . . . .	19
2.2 Nanostructured Self-Assembled Materials . . . . .	25
2.2.1 Fabrication of Self-Assembled Quantum Dots . . . . .	25
2.2.2 Band Structure in Nanostructured Materials . . . . .	25

2.2.3	Energy Transport & Loss in Nanostructured Materials . . . . .	27
2.3	Colloidal Quantum Dot Materials . . . . .	30
2.3.1	Fabrication of Colloidal Quantum Dot Materials . . . . .	31
2.3.1.1	Synthesis . . . . .	31
2.3.1.2	Monolayer Film Formation . . . . .	32
2.3.2	Band Structure of Colloidal Quantum Dot Materials . . . . .	33
2.3.2.1	Quantum Confinement . . . . .	33
2.3.2.2	Type I and Type II Band Alignment . . . . .	34
2.3.3	Energy Transport & Loss in Colloidal Quantum Dot Materials	35
2.3.3.1	Surface Passivation . . . . .	36
2.3.3.2	Förster Resonance Energy Transfer . . . . .	37
<b>3</b>	<b>OPTICAL CHARACTERIZATION OF PHOTOVOLTAIC</b>	
	<b>MATERIALS . . . . .</b>	<b>39</b>
3.1	Photoluminescence . . . . .	39
3.2	Time Resolved Photoluminescence . . . . .	39
3.2.1	Mira-900 femtosecond laser . . . . .	40
3.2.2	Second Harmonic Generator System . . . . .	41
3.2.3	ConOptics Pulse Modulation system . . . . .	42
3.2.4	Spectrometer . . . . .	43
3.2.5	Avalanche Photodiode . . . . .	43
3.2.6	PicoHarp 300 Time-Correlated Single Photon Counting system	46
3.2.7	Data analysis . . . . .	48
3.2.7.1	Exponential Fitting . . . . .	48
3.2.7.2	Deconvolution of IRF . . . . .	49
<b>4</b>	<b>TIME-RESOLVED PHOTOLUMINESCENCE FOR ASSESSING</b>	
	<b>MATERIAL QUALITY IN SEMICONDUCTORS . . . . .</b>	<b>51</b>
4.1	Application of TRPL to Quantification of Trap Densities in GaAs . .	51
4.2	Gallium Arsenide Double Heterostructures Grown by MOCVD . . . . .	52
4.3	Intensity-dependent time-resolved photoluminescence . . . . .	52

<b>5 ENERGY TRANSFER DYNAMICS IN SELF-ASSEMBLED InAs QUANTUM DOT ErAs NANOINCLUSION SUPERLATTICES</b>	<b>61</b>
5.1 Nanocomposite Materials . . . . .	61
5.2 Sample Structure . . . . .	62
5.3 Temperature Dependent Photoluminescence and Time-Resolved Photoluminescence . . . . .	64
<b>6 ENERGY TRANSPORT AND RECOMBINATION IN COLLOIDAL QUANTUM DOT STRUCTURES</b>	<b>73</b>
6.1 Colloidal QD Cascade Structures . . . . .	73
6.1.1 Cascade Structure Fabrication . . . . .	74
6.1.2 Energy Transport Mechanisms & Characterization . . . . .	75
6.2 Type I & II Structures . . . . .	83
6.2.1 Structure Formation . . . . .	83
6.2.2 Energy Transport Mechanisms & Characterization . . . . .	84
<b>7 CONCLUSIONS</b>	<b>89</b>
<b>BIBLIOGRAPHY</b>	<b>92</b>
<b>Appendix</b>	
<b>A MATHEMATICA CODE FOR DEBUF MODEL</b>	<b>98</b>
<b>B RIGHTS AND PERMISSIONS</b>	<b>105</b>

## LIST OF TABLES

2.1	Photoluminescence emission ranges for chalcogenide colloidal quantum dots. . . . .	34
4.1	Estimated trap density for GaAs/InGaP double heterostructures grown by MOCVD at varying rates. . . . .	58
6.1	Lifetimes of donor-only and donor-acceptor film structures. . . . .	82
6.2	Lifetimes of lead chalcogenide quantum dot structures [1]. . . . .	86

## LIST OF FIGURES

2.1	The potential model of a super lattice for the Kronig-Penny Model	8
2.2	Allowed energies as a function of the Bloch wavenumber, $k$ , computed from Equation 2.3. Note the emergence of bandgaps, ranges of energy in which there are no allowed states [2]. . . . .	9
2.3	“The basic processes involved in recombination by trapping: (a) electron capture, (b) electron emission, (c) hole capture, (d) hole emission.” [3]. . . . .	13
2.4	Cross-sectional SEM of self assembled quantum dots stacked along the growth direction [4]. . . . .	25
2.5	A potential step with a wave incident from the left. The potential is $V = 0$ on the left, $V = V_0$ on the right. . . . .	28
2.6	Solutions of CdSe colloidal quantum dots of varying sizes [5]. . . . .	30
2.7	PL emission ranges of various sizes and materials of colloidal quantum dots [6]. . . . .	33
2.8	Types of heterojunction alignment [7]. . . . .	35
3.1	Cartoon of the functional concept of a spectrometer. . . . .	44
3.2	Schematic of an avalanche photodiode [8]. . . . .	46
3.3	Schematic of a photomultiplier tube [9]. . . . .	47
3.4	This figure shows an example of a simple, single exponential tail fit [10]. . . . .	49
3.5	This figure shows an example of a double exponential fitting model with a deconvolution of the instrument response function (red) from the data (blue) [10]. . . . .	50

4.1	Schematic of the GaAs double heterostructure sample with 100 nm InGaP window layers and 10 $\mu\text{m}$ active region . . . . .	52
4.2	Fluence dependent time resolved photoluminescence decay curves for MOCVD GaAs grown at 14 $\mu\text{m/hr}$ [11]. . . . .	54
4.3	Measured minority carrier decay time as a function of excess minority carrier density as calculated from laser fluence [11]. . . . .	55
4.4	Measured minority carrier decay time as a function of excess minority carrier density as calculated from laser fluence. Solid lines show the fit calculated from the Debuf et. al. model [11]. . . . .	57
4.5	Minority carrier lifetime as a function of doping computed using the estimated trap densities and the SRH model [11]. . . . .	59
5.1	Schematic physical structure of one period of InAs quantum dots and ErAs nanoinclusions. . . . .	63
5.2	Schematic band diagram of one period of InAs quantum dots and ErAs nanocomposite [12]. . . . .	63
5.3	Temperature dependent photoluminescence of InAs self-assembled QDs. Inset: PL decay curves of InAs QD measured at 1060 nm and 10 K for four samples including the Control sample without ErAs MNPs, and GaAs spacer layers of 40 nm, 12 nm, and 10 nm [12]. . . . .	65
5.4	Temperature dependence of photoluminescence lifetime of samples with GaAs spacer layers of 40 nm, 12 nm, 10 nm [12]. . . . .	66
5.5	Schematic band diagram of one period of InAs quantum dots and ErAs nanocomposite including an AlGaAs spacer layer instead of GaAs to rule out FRET as an energy transfer mechanism. . . . .	67
5.6	Comparison of donor emission and acceptor absorption spectra. a) Absorption spectra for ErAs nanoparticles embedded in GaAs with varying volume fractions of ErAs [13]. b) InAs quantum dot PL emission spectra. . . . .	68
5.7	Fluence dependence of the PL lifetime in InAs QDs with varying distances from the ErAs nanocomposite region [12]. . . . .	69

5.8	Dependence of PL lifetime on the thickness of the GaAs spacer layer with tunneling model [12]. . . . .	71
5.9	Dependence of PL lifetime on the thickness of the GaAs spacer layer with tunneling model and FRET model. . . . .	71
6.1	Cartoon of the colloidal quantum dot cascade structure [14]. . . . .	74
6.2	a) Steady-state photoluminescence of the OA, EDT and BDT-treated QD monolayers. b) Three sizes of PbS CQDs with 980 nm (blue) absorption solid line, emission dotted line, 1055 nm (green), 1240 nm (red) [14]. . . . .	76
6.3	a) Steady-state PL measurement of 980nm and 1055nm CQD films using BDT ligand exchange. Monolayers (blue and green) and bilayer (black). b) Gaussian fit to the bi-layer PL spectrum showing a quenching of the 980 nm and an enhancement of the 1055 nm emission [14]. . . . .	77
6.4	PL spectrum of the 1240 nm monolayer (pink), 1240 nm-1055 nm bilayer (green), 1055 nm-1240 nm-1055 nm cascade structure (blue), and 980 nm-1055 nm-1240 nm-1055 nm-980 nm cascade structure (black) [14]. . . . .	78
6.5	Absorption spectra of monolayer-by-monolayer assembly of PbS CQD solid treated with BDT [14]. . . . .	79
6.6	Photoluminescence of the five layer BDT-treated cascade structure (red), five layers of BDT-treated 1240 nm emission acceptor CQDs (black) and a single monolayer of 1240 nm acceptors. Inset: The absorption spectra of the 5-layer 1240 nm acceptor CQDs (black) and the 5-layer cascade [14]. . . . .	80
6.7	Photoluminescence of the five layer EDT-treated cascade structure (red), five layers of EDT-treated 1240 nm emission acceptor CQDs (black) and a single monolayer of 1240 nm acceptors [14]. . . . .	81
6.8	Time-resolved photoluminescence of PbS CQD films measured at the donor peak of 980 nm. a) OA capped untreated PbS CQD film (blue), donor-only BDT-treated PbS film (black), and BDT-treated donor-acceptor bilayer (red). b) Donor-only EDT-treated PbS film (black), and EDT-treated donor-acceptor bilayer (red) [14]. . . . .	82

6.9	Photoluminescence emission from the three layer type-I CQD structure (blue), two layers of PbSe (black), PbSe-PbS bilayer (red) and a monolayer of PbS CQDs [1]. . . . .	85
6.10	Time-resolved photoluminescence taken at 950nm of PbS BDT-treated film (black with blue fit line) and a BDT treated type-I structure (red with green fit line) [1]. . . . .	86
6.11	PL from a four layer PbSe film (blue), a four layer PbS film (green), and a type-II PbS-PbSe-PbS-PbSe four layer heterostructure. The arithmetic average between the PbS (green) and PbSe (blue) four layer films is shown for comparison with the heterostructure [1]. . .	87
6.12	Time-resolved photoluminescence decays of BDT treated type-I and type-II heterostructures showing the reduced PL lifetime in the type-II structure [1]. . . . .	88

## ABSTRACT

Energy transport and loss are critical to the performance of optoelectronic devices such as photovoltaics and terahertz imaging devices. Nanostructured materials provide many opportunities to tailor transport and loss parameters for specific device applications. However, it has been very difficult to correlate specific nanoscale structural parameters with changes in these performance metrics. I report the development of new ways of using time-resolved photoluminescence (TRPL) to probe charge and energy transport and loss dynamics. These techniques are applied to several types of nanostructured materials, including bulk semiconductors with defects, self-assembled quantum dots and colloidal quantum dots. First, GaAs/InP double heterostructures grown via metal organic chemical vapor deposition (MOCVD) were characterized with TRPL. TRPL is typically used to extract minority carrier lifetimes, but we discovered that the measured lifetime depended critically on the intensity of the exciting laser. We developed a Shockley-Read-Hall model to extract trap state densities from intensity-dependent TRPL measurements. Second, we characterized energy and charge transfer between InAs quantum dots and ErAs nanoinclusions within III-V heterostructures. Using intensity- and temperature-dependent TRPL, we confirmed tunneling as the dominant mechanism of charge transport and characterized the electronic structure of the ErAs nanoparticles. Finally, we characterized energy transport in colloidal quantum dot cascade structures. These cascade structures utilize Förster Resonance Energy Transfer and trap state recycling to funnel excitons from donor layers to acceptor layers and suggest a promising method for avoiding losses associated with surface trap states. Collectively, the analysis of these disparate material types advances our understanding of energy dynamics in nanostructured materials and improves our ability to design the next generation of photovoltaic and optoelectronic materials and devices.

# Chapter 1

## INTRODUCTION

Optoelectronic devices, from lasers to photovoltaic cells, are fundamental technologies that rely on an understanding of semiconductor material properties. For example, photovoltaic devices are a promising technological solution to the challenge of finite fossil fuel resources and their concomitant environmental consequences. Nanoscale materials provide a new set of properties that have been, and continue to be, used to advance optoelectronic device performance. Quantum confinement in colloidal and self-assembled quantum dots, for example, allows energy absorption and transfer to be tailored based on the size and composition of the particles. Understanding the properties of these materials, particularly the dynamics of energy transfer and loss, is critical to enabling improved optoelectronic device performance.

Previous work to understand carrier dynamics in semiconductors used lifetime and mobility measurements. For example, measuring the photoconductance lifetime in bulk semiconductors can be used to obtain a minority carrier lifetime that provides one measure of material quality that has been used for many years to characterize semiconductor materials [15]. Mobility can be determined by four point probe or field effect transistor measurements. These techniques can be useful in providing a basic understanding of how energy and carriers are transported through a material, but they do not, by themselves, provide a way to characterize the complex dynamics of carrier and energy transfer and loss that occur in nanostructured materials.

Time-resolved photoluminescence is another technique commonly used to understand lifetime and carrier dynamics in semiconductor materials. Ahrenkiel has developed a process using careful control of experimental conditions and the structure of

bulk semiconductors to extract detailed recombination rates using time-resolved photoluminescence (TRPL) [16], [17]. In its simplest form the PL lifetime can be considered a single parameter,  $\tau_{PL}$ , that is a characteristic lifetime representing the time at which  $1/e$  of the optically generated carriers have recombined or been lost to nonradiative energy or charge transfer processes. Ahrenkiel noted that the PL lifetime is limited not only by non-radiative recombination ( $\frac{1}{\tau_{PL}} = \frac{1}{\tau_R} + \frac{1}{\tau_{nR}}$  where  $\frac{1}{\tau_R}$  is the radiative lifetime and  $\frac{1}{\tau_{nR}}$  is the non-radiative lifetime), but that the non-radiative component itself can be made up of contributions from surface recombination, Auger recombination, and defect recombination. Ahrenkiel also defined how reabsorption processes like photon recycling affect the measured lifetime [18]. By defining the impact of these processes on measured PL lifetime, Ahrenkiel gave us a blueprint for interpreting time-resolved photoluminescence data in a manner that goes beyond the assumption that measured PL lifetime is the same as the intrinsic minority-carrier lifetime.

We build upon these techniques for isolating and controlling multiple recombination pathways that influence TRPL results by applying them to nanostructured materials. In the same vein as the work by Ahrenkiel, we first examined bulk GaAs double heterostructures for high efficiency PV applications, applying a novel model to overcome the challenge of measuring low-doped materials in the middle and high injection regimes. We then examine the PL lifetimes of InAs quantum dots to probe the electronic properties of and charge transfer to ErAs metal nanoparticles in a semiconductor nanocomposite with possible THz device applications. Finally, we apply our techniques of separating recombination mechanisms to colloidal nanoparticles and use control over heterostructure composition and formation conditions to trigger different recombination and carrier transfer pathways. By applying this approach to nanostructured materials, we develop a more detailed understanding of energy transfer dynamics that enables the rational application of more sophisticated nanostructuring techniques in the design of optoelectronic devices.

## Chapter 2

### OPTOELECTRONIC PROPERTIES OF SEMICONDUCTORS

This chapter provides an overview of the previous work in characterizing the properties of semiconductor materials both in the bulk and in nanostructures. We begin with a basic review of fabrication methods and properties of optoelectronic materials. We then provide an experimental and theoretical basis for understanding how TRPL can be used to characterize the energy transfer and loss dynamics in nanostructured materials.

#### 2.1 Bulk Semiconductor Materials

##### 2.1.1 Fabrication

Bulk semiconductor materials can be fabricated through a variety of techniques. The method of fabrication often plays a critical role in the nature and density of defects that influence optoelectronic device performance and the various techniques are reviewed below.

###### 2.1.1.1 Bulk Processes

Semiconductor materials are typically processed on an industrial scale through various bulk processes that take place at thermal equilibrium [19]. Such techniques include the Czochralski process, liquid phase epitaxy, float-zone, micro-pulling-down, laser-heated pedestal or laser float zone growth, vertical gradient freeze (VGF) and Bridgman-Stockbarger technique.

Single crystals of semiconductor materials such as silicon, gallium arsenide, and germanium can be made in large volumes of consistent quality with the **Liquid-encapsulated Czochralski** process (LEC). In the Czochralski process silicon or another semiconductor is melted in a high-purity quartz crucible, and desired dopants added to the melt. A seed crystal is dipped into the melt and the crucible and the seed are rotated as the seed is very slowly withdrawn. At the liquid melt interface the melt transitions into the solid phase and replicates the orientation of the seed crystal. The thermodynamics of the melt, the withdraw rate and the rotation rate determines the size of the boule that can be produced [19]. It is harder to grow compound semiconductors like GaAs and InP via LEC because stacking fault energy and resolved shear stress are lower in most compound semiconductors and promote twinning and high dislocation density respectively [19].

The **Bridgman-Stockbarger technique** is used on materials such as gallium arsenide for which the Czochralski process is difficult. In the Bridgeman technique a boule of polycrystalline material is kept in the crucible and heaters are moved along its length, heating the material to just above its melting point. The crystal grows along the length of the boule as the heater moves to the next location and the material cools, taking the crystallographic orientation of the seed. Boules grown by the Bridgeman method are smaller than by the LEC method, but for compound semiconductors they have dislocation densities an order of magnitude lower [19].

The **Float-zone process**, developed by William Gardner Pfann at Bell Labs, involves melting a narrow zone of the semiconductor ingot and moving the melt along the length of the ingot. The impurities move to the leading edge of the melt. The melt, with increasing concentration of impurities, is moved to the end of the ingot and removed leaving behind a pure semiconductor [19].

### 2.1.1.2 Epitaxial Processes

Bulk processes cannot produce the nanostructures and heterostructures used to control energy transfer in materials and achieve complex device architectures such

as those used for quantum cascade lasers, multijunction photovoltaics or LEDs. Instead, epitaxial processes are used. The word epitaxy comes from the Greek and is composed of the words *epi* meaning *on top of* and *taxis* meaning *arrangement*. Together they refer to the arrangement of a crystalline thin-film on a substrate. Epitaxial techniques are also referred to as non-equilibrium techniques because they take place away from thermodynamic equilibrium. Surface processes such as adsorption, thermal desorption, surface migration, and interdiffusion, rather than bulk thermodynamics, govern the processes. The two epitaxial techniques commonly used to grow nanostructured semiconductor materials are molecular beam epitaxy (MBE) and metal organic chemical vapor deposition (MOCVD) [19].

**Metal-organic Chemical Vapor Deposition (MOCVD)** is a semiconductor fabrication technique in which the material is formed from a chemical reaction. Multicrystalline or single crystal films can be produced on a commercial scale for many types of substrates and films. For growth of III-V semiconductors via MOCVD, metal-organic compounds containing group III elements and halide gases containing group V elements are introduced into the reaction chamber at mild pressures. Vapors of the metal-organic compounds are introduced into the chamber by passing an inert carrier gas such as argon or nitrogen through a bubbler of the metal-organic material, producing a dilute gas. The substrate is heated and has a catalytic effect on the gases causing the deposition of a film onto the substrate [19].

**Molecular Beam Epitaxy** is a very common, though costly, epitaxial growth technique for high quality semiconductor thin films and nanostructures. In this technique, beams of atoms and molecules react on the surface of a single crystalline substrate under ultra-high vacuum conditions ( $10^{-10}$  to  $10^{-11}$  torr). Atom and molecule beams are produced most commonly from Knudsen effusion cells which are often made of pyrolytic boron nitride and are used to heat solid precursor sources to about their melting point. Shutters are used to control the flow of gaseous atoms reaching the substrate surface [19].

### 2.1.2 Band structure

Materials can be classified based on their electronic properties as insulators, conductors and semiconductors. As the name suggests, conductors easily conduct electrons and generally have a range of resistivity of  $10^{-8} \Omega$  or less. Insulators do not easily conduct charge carriers and have a range of resistivity of  $10^{16} \Omega$  or greater at room temperature. Semiconductors have a conductivity range between that of insulators and conductors. Semiconductors are useful for fabricating electronic devices because the degree to which they conduct electricity can be engineered to suit the application by way of doping and applied voltage. These useful properties of semiconductors arise because of the crystal and chemical structure of the semiconductor material.

The conductivity of a material arises from the band structure, which in turn arises from the fundamental chemical structure of the materials' lattice. Atoms in a material have a valence shell of electrons that interact with the surrounding environment. In a crystal, the periodic arrangement of atoms leads to overlap of the electron wave functions of neighboring atoms. When atoms come into close proximity with each other the Pauli exclusion principle requires that the electrons cannot remain at the same energy level. The periodic arrangement of the lattice leads to the emergence of a ladder of delocalized energy states for electrons. The energy spacing between these allowed states and the number of states that are filled by existing electrons is determined by the lattice periodicity and number of valence electrons of the lattice atoms.

The level to which electrons fill the band is called the *Fermi level* or chemical potential. Technically the Fermi level is only defined at absolute zero, though it is typical practice in the semiconductor community to use the term to refer to the chemical potential at finite temperatures. When the Fermi level overlaps available states for electrons, the material is a conductor. When there is a small energy gap between filled states at or below the Fermi level and the next available states, the material is a semiconductor. When there is a large gap between states at or below the Fermi level and the next available states the material is an insulator because there is not typically

sufficient thermal or optical energy available to promote electrons from filled states to empty states in order to allow electrical conduction. In a semiconductor, the filled states at or below the Fermi level are called the valence band and the empty states above the band gap are called the conduction band.

The free electron model provides a simple, but highly effective, description of the transport of electrons in energy bands. It arises from a quantum mechanical understanding of electrons in materials and can be expanded to understand a wide variety of electronic material behavior. In the free electron model, valence electrons are free to move throughout the material. The solution to the Schrödinger equation models the wave function of the electron as: [20]

$$\psi_{\mathbf{k}}(\mathbf{r}) = \exp(i\mathbf{k} \cdot \mathbf{r}) \quad (2.1)$$

The free electron model is most useful for metals and for material properties that rely on kinetic motion of electrons. Where electrostatic interactions with the lattice occur, this model must be expanded to the nearly-free electron model [20]. These extensions to the free electron model are used to take into account the periodic lattice that makes up solid materials and allows one to describe how the band gaps arise in materials.

The extension of the free electron model takes into account Bragg reflection in solids, which is one way of understanding the emergence of energy band gaps. When the electron wave functions are scattered by the crystal, the reflected waves create constructive and destructive interference based on the wavelength of the electron wave function and the lattice spacing  $a$  of the crystal. This interference gives rise to the energy gap that defines the band gap energy  $E_g$  of the material and determines its optical and electronic properties.

The **Kronig-Penny model** provides a simple illustration of how the band structure of a solid state material arises from quantum mechanical properties [21]. The Kronig-Penny model is derived from the assumption that the lattice in a solid material can be modeled as an infinite series of square barriers as seen in Figure 2.1. The

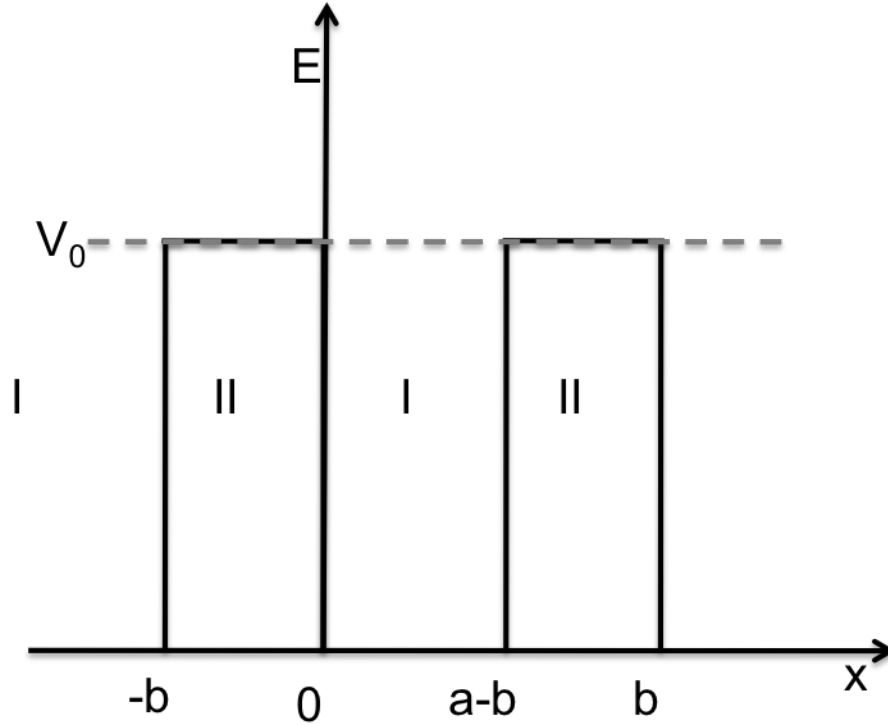


**Figure 2.1:** The potential model of a super lattice for the Kronig-Penny Model

potential barriers represent the coulomb interaction attracting electrons to the atomic nuclei of the material and Schrödinger's equation is solved for an electron traveling through the lattice. Bloch's theorem proved that the solutions of the Schrödinger equation in a periodic potential take the form:

$$\psi_{\mathbf{k}}(\mathbf{r}) = u_{\mathbf{k}}(\mathbf{r}) \exp(i\mathbf{k} \cdot \mathbf{r}) \quad (2.2)$$

where  $u_{\mathbf{k}}(\mathbf{r})$  is periodic with the crystal lattice [20]. This is called a Bloch function. Bloch's theorem states that: "The eigenfunctions of the wave equation for a periodic potential are the product of a plane wave  $\exp(i\mathbf{k} \cdot \mathbf{r})$  times a function  $u_{\mathbf{k}}(\mathbf{r})$  with the periodicity of the crystal lattice" [21].

A full derivation can be found in many introductory solid state textbooks. The

result is a transcendental equation:

$$\cos(ka) = \cos(ka) + \left(\frac{maS}{\hbar^2}\right) \frac{\sin(ka)}{ka} \quad (2.3)$$

where  $S = V_0b$ . The assumption for crystalline materials is that  $S$  remains the same as in the resonant tunneling (finite barrier width) case, but  $V_0 \rightarrow \infty$  and  $b \rightarrow 0$  giving the case where  $b$  is a delta function and no longer a finite barrier. Plotting the energy  $E = \hbar^2k_1^2/2m$  against the Bloch wavenumber  $k$  from the solution to the above equation shows, as seen in Figure 2.2, the resulting energy gaps at  $k = n\pi/a$ . Figure 2.2 thus illustrates how periodic potentials lead to the origin of band structure in solid state materials [21].

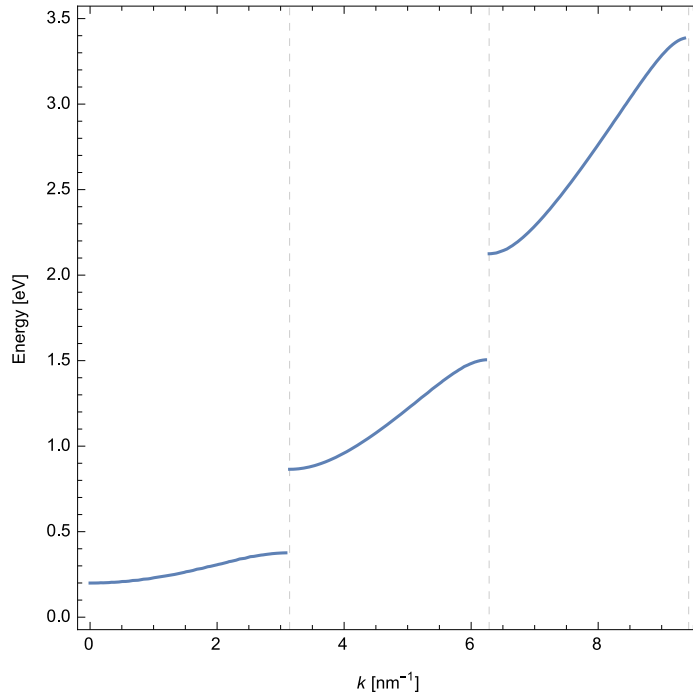


**Figure 2.2:** Allowed energies as a function of the Bloch wavenumber,  $k$ , computed from Equation 2.3. Note the emergence of bandgaps, ranges of energy in which there are no allowed states [2].

### 2.1.3 Energy Transport & Loss in Bulk Materials

Energy loss and recombination in semiconductors influences the properties of the material and the device performance. In photovoltaic devices, for example, carrier

recombination and loss pathways contribute to reduced photocurrent and lower power output. It is thus important to characterize the transport and loss mechanisms in semiconductors in order to understand what changes in material properties can be made to improve efficiency. This section introduces common experimental and analytical tools used to quantify energy loss and carrier recombination pathways.

### 2.1.3.1 Minority Carrier Lifetime

Minority carriers are the less abundant carrier species in a material. If a material is p-type (doped with holes), for example, electrons are the minority carrier. Similarly, if the material is n-type (doped with electrons), holes are the minority carriers. Minority carrier lifetime is an important property that influences the performance of many optoelectronic devices. From photovoltaics to transistors to LEDs, minority carrier lifetimes, and the ratio of radiative to non-radiative recombination, plays a crucial role in device performance. Minority carrier lifetime can be limited by a range of intrinsic properties in addition to radiative or non-radiative recombination. From the work of Ahrenkiel and others we know that a characteristic minority carrier lifetime,  $\tau$ , is a linear combination of the lifetimes of these mechanisms [22].

$$\frac{1}{\tau} = \frac{1}{\tau_{nR}} + \frac{1}{\tau_R} \quad (2.4)$$

where  $\tau_{nR}$  is the non-radiative lifetime and  $\tau_R$  is the radiative lifetime. The non-radiative component can be dominated by surface, defect or auger recombination. Recombination mediated by defects is called Shockley-Read-Hall (SRH) recombination and can be described by the SRH rate equations, which accounts for the rate of carrier capture and emission from defects, the concentration of defects and of carriers, the energy level of the defect and the lifetime of the carrier in the defect [3]. Explicitly listing the additional processes that contribute to the non-radiative component of lifetime means that Equation 2.4 becomes:

$$\frac{1}{\tau} = \frac{1}{\tau_R} + \frac{1}{\tau_S} + \frac{1}{\tau_{SRH}} + \frac{1}{\tau_A} \quad (2.5)$$

where  $\tau_S$  is the surface recombination limited lifetime,  $\tau_{SRH}$  is the Shockley-Read-Hall recombination limited lifetime and  $\tau_A$  is the Auger recombination limited lifetime. The rate of surface recombination can be described as  $\frac{2S}{d}$  where  $S$  is the interface recombination velocity and  $d$  is the thickness of the active region. The interface recombination velocity can be determined from  $S = \sigma\nu_{th}N_s$  where  $\sigma$  is the capture cross section for surface defects,  $\nu_{th}$  is the thermal velocity, and  $N_s$  is the planar density of surface recombination centers [22]. These parameters can be obtained by experimentally measuring the PL lifetime ( $\tau_{PL}$ ) of nominally identical samples with different thicknesses of active region and calculating the slope of  $1/\tau_{PL}$  vs.  $2/d$  to obtain the surface recombination velocity  $S$  [18].

Auger recombination is an interaction between three particles, often two electrons and an hole, in which an electron and hole recombine and non-radiatively transfer energy to the remaining electron, promoting it to an excited state. The rate of Auger recombination can be estimated from  $\frac{1}{\tau_A} = \sigma_A N^2$  where  $\sigma_A$  is the Auger cross-section, and  $N$  is the majority carrier number density. Auger recombination dominates the lifetime only at very high doping densities. The Shockley-Read-Hall or defect recombination can be described in relation to the defect density  $N_t$  in terms of  $\frac{1}{\tau_{SRH}} = \sigma\nu_{th}N_t$  where  $\nu_{th}$  is the thermal velocity, and  $\sigma$  is the capture cross-section for a particular type of trap. From here we can see that Equation 2.5 becomes:

$$\frac{1}{\tau} = \frac{1}{\tau_r} + \frac{2S}{d} + \sigma\nu_{th}N_t + \sigma_A N^2 \quad (2.6)$$

The measured PL lifetime of a material can also be affected by photon recycling, a process of self-absorption of the photons emitted by radiative recombination of carriers. This effect lengthens the observed lifetime relative to the intrinsic radiative lifetime [23]. Photon recycling affects the radiative lifetime in the low injection regime following the relationship  $\tau_R = \phi(d)/(BN)$ , where  $\phi$  is the effective photon recycling factor and  $B$  is the radiative recombination coefficient that is proportional to the matrix element and  $N$  is the majority carrier density [24]. The overlap between the emission spectrum and the absorption spectrum of the material is one factor influencing the

strength of photon recycling. When calculating the surface recombination velocity, a non-linear relationship for  $1/\tau_{PL}$  vs.  $2/d$  suggests photon recycling is playing a role in the measured PL lifetime [18].

### 2.1.3.2 Shockley-Read-Hall Recombination

Shockley-Read-Hall recombination, or defect recombination, is a common energy loss pathway in semiconductor materials that influences device performance. The widely known Shockley-Read-Hall model is commonly used to describe non-radiative recombination in semiconductors. The model examines how the lifetime of excited carriers is influenced by recombination due to traps caused by material defects. The types of mechanisms responsible for non-radiative recombination via trap centers can be seen in Figure 2.3.

A neutral trap can capture an electron from the conduction band or valance band, making the trap negative and leaving a hole behind. It can also capture a hole from the conduction or valance band leaving behind an electron. The model assumes that the limitation of the recombination rate is the availability of carriers for trapping. Other possible rate limiting factors that the model neglects are the relaxation time if a carrier is trapped in an excited state, but this is typically a very fast process and creates a negligible lag in time between trapping and relaxation to the ground state of the trap.

To understand how the Shockley Read Hall model can be extended to a range of excited carrier densities we must first understand the derivation of the initial equations that describe recombination in semiconductors. The recombination processes are governed by Fermi-Dirac statistics, where  $f$  represents the probability that a quantum state is occupied by an electron,  $E$  is the energy level of the quantum state,  $F$  is the Fermi level,  $k$  is Boltzman's constant and  $T$  is temperature in Kelvins [3].

$$f = 1/[1 + \exp[(E - F)/kT]] \quad (2.7)$$

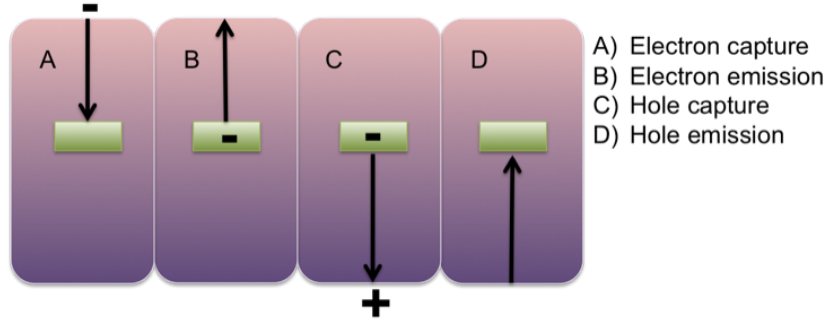


**Figure 2.3:** “The basic processes involved in recombination by trapping: (a) electron capture, (b) electron emission, (c) hole capture, (d) hole emission.” [3].

Conversely,  $f_p$  is the probability that the state is occupied by a hole and is given by:

$$f_p = 1 - f = \exp[(E - F)/kT] \quad (2.8)$$

In examining the electron capture process we see that the total number of quantum states, per unit volume, in the energy range  $dE$  is

$$N(E)dE \quad (2.9)$$

Given that the number of trapping centers is  $N_t$ ,  $c_n$  is the average probability for a carrier in  $dE$  to be captured by a trap, and  $f_{pt}$  represents the probability the trap is empty, the rate of capture will be: [3]

$$f_{pt}N_t c_n(E) f(E) N(E) dE \quad (2.10)$$

The probability that an electron will be emitted from a trap will be proportional to the number of electrons in the traps times the probability that the states in the range

$dE$  are empty. If  $e_n$  is the emission constant then the probability of electron emission is

$$f_t N_t e_n f_p(E) N(E) dE \quad (2.11)$$

By making the assumption that the electrons in the conduction band are in thermal equilibrium we denote a quasi fermi level  $F_n$  that also describes the fraction of traps that are occupied. We must assume that the rate of capture and the rate of emission of electrons are equal [3].

The net rate of capture can be written

$$dU_{cn} = [f_{pt} f(E) - (e_n/c_n) f_t f_p(E)] N_t c_n(E) N(E) dE \quad (2.12)$$

For thermal equilibrium the quantity in brackets must be zero, thus: [3]

$$e_n/c_n = \exp[(E_t - E)/kT] \quad (2.13)$$

where  $E_t$  is the trap energy. If it is assumed that the electrons in the conduction band are in thermal equilibrium,  $f$  and  $f_p$  are given by the Fermi-Dirac equation and the quasi Fermi level is represented by  $F_n$  or  $F_t$  for the fraction of filled traps. Integrating  $dU_{cn}$  over  $dE$ , we obtain the total rate of electron capture  $U_{cn}$

$$U_{cn} = [1 - \exp(F_t - F_n)/kT] f_{pt} N_t \quad (2.14)$$

When the system is in equilibrium, the square bracket vanishes and when  $F_n$  is greater than  $F_t$  there is a net rate of capture. The total rate of electron capture,  $U_{cn}$ , is obtained by integrating over  $dE$  [3].

$$U_{cn} = [1 - \exp\{(F_t - F_n)/kT\}] f_{pt} N_t \times \int_{\epsilon_c}^{\infty} f(E) N(E) c_n(E) dE \quad (2.15)$$

where the integration extends from the bottom of the conduction band to all higher levels. If  $F_n > F_t$  then there is a net rate of capture [3].

Shockley and Read describe the case where the electron and holes distributions are non-degenerate, where the the doping levels are sufficiently low that each dopant can be considered a localized state and the Fermi energy is far below the bottom of the conduction band. In this case, the previous equation can be rewritten as

$$U_{cn} = [1 - \exp(F_t - F_n) / kT] f_{pt} n C_n \quad (2.16)$$

where

$$n = N_c \exp(F_n - E_c) / kT \quad (2.17)$$

$$N_c = \int_{E_c}^{\infty} [\exp(E_c - E) / kT] N(E) dE \quad (2.18)$$

$$C_n = N_t \langle c_n \rangle \quad (2.19)$$

$$\langle c_n \rangle = \int_{E_c}^{\infty} \frac{[\exp(E_c - E) / kT] c_n(E) N(E)}{N_c} \quad (2.20)$$

The quantity  $C_n$  is the probability per unit time that an electron from the conduction band will be captured by a trap, under the conditions that all traps are empty. Conversely, we see that  $C_p$  is the probability per unit time that a hole can be captured from the valence band, following the assumption that all traps are filled with electrons and thus can capture holes [3].

For non-degenerate semiconductors, the traps in the conduction band are almost all empty, thus making  $f_p$ , the probability that a state is empty (or filled by a hole), near unity for the states in the conduction band. Thus, the emission rate is a function of  $f_t$  only. From Equation 2.16 it follows that the rate of emission is independent of  $F_n$ , the quasi fermi level for electrons, because the dependencies in the exponentials and in  $n$  cancel out giving:

$$f_{pt} n \times \exp(F_t - F_n) / kT = f_t N_c \times \exp(E_t - E_c) / kT \equiv f_t n_1 \quad (2.21)$$

where

$$n_1 = N_c \exp(E_t - E_c) / kT \quad (2.22)$$

is the number of electrons in the conduction band for the case in which the Fermi level is  $E_t$  [3].

In terms of  $n_1$ , the net rate of capture for electrons is:

$$U_{cn} = C_n f_{pt} n - C_n f_t n_1 \quad (2.23)$$

and for holes:

$$U_{cp} = C_p f_t p - C_p f_{pt} p_1 \quad (2.24)$$

If we assume that electron hole pairs are being generated at a constant rate  $U$  by some form of carrier injection, there must be a steady-state solution in which the rate of net electron and hole capture must be equal, which leads to:

$$C_n (1 - f_t) n - C_n f_t n_1 = C_p f_t p - C_p (1 - f_t) p_1 \quad (2.25)$$

Solving for  $f_t$  one arrives at:

$$f_t = (C_n n + C_p p_1) / [C_n (n + n_1) + C_p (p + p_1)] \quad (2.26)$$

When  $f_t$  and  $f_{pt}$  are substituted into the rate expressions the result is the net recombination rate:

$$U = C_n C_p (pn - p_1 n_1) / [C_n (n + n_1) + C_p (p + p_1)] \quad (2.27)$$

The product  $p_1 n_1$  is independent of the trap energy level and is defined as:

$$p_1 n_1 = N_c N_p \exp(E_v - E_c) / kT = N_c N_p \exp(-E_G / kT) = n_i^2 \quad (2.28)$$

where  $n_i$  is the electron and hole concentration in an intrinsic semiconductor, a material in which  $n$  and  $p$  are equal. The Fermi level in an intrinsic sample is described as  $E_i$  [3].

$$E_i = \frac{1}{2}(E_c - E_v) + \frac{1}{2}kT \ln(N_v/N_c) \quad (2.29)$$

Assuming that  $E_t > E_i$  and thus  $n_1 > n_i > p_1$ . When  $E_t < E_i$  the roles of electrons and holes are reversed (majority and minority carriers).

In Shockley and Read's paper they next describe the simple case in which the disturbance in the carrier density from excitation is small and in which the majority carrier density remains in equilibrium. In the appendix, Shockley and Read go on to relax this condition and expand the argument to a general case. Debuf et. al. expand this general case to arrive at an analytical model of carrier recombination [25]. Debuf's model is the foundation of our intensity-dependent TRPL analysis.

Shockley and Read describe in the appendix of their paper a general case in which the density of traps is not small compared to the normal carrier density and where  $\delta n$  and  $\delta p$  are not necessarily equal. This is important in relating the SRH model to our analysis, because the GaAs/InGaP double heterostructure samples we studied were nominally undoped, meaning that the number of traps could approach the level of the normal carrier density.

The assumption is made in the SRH model that the disturbances in the carrier density from the excitation source are small enough that only first order terms of  $\Delta n$  and  $\Delta p$ , the excess electron and hole concentrations, need to be considered. This is an important point to be considered when we later discuss the Debuf model. This simplifying assumption allows SRH to solve a linear rate equation; Debuf et. al. expand the model to solve a complete second order non-linear rate equation without making this low injection assumption.

From the low injection assumption (small disturbances in carrier density) the recombination rates are linear functions of  $\delta n$  and  $\delta p$ :

$$U_{cn} = A_{nn}\delta n + A_{np}\delta p \quad (2.30)$$

$$U_{cp} = A_{pn}\delta n + A_{pp}\delta p \quad (2.31)$$

The A's are constants. These equations, along with the continuity equation, provide a set of linear partial differential equations which can be solved for the excess carrier densities for any given set of boundary conditions. Shockley and Read's paper is primarily concerned with the steady state condition in which  $U_{cn} = U_{cp} = U$ , and since  $\delta n \neq \delta p$  two lifetimes can be found where, in general,  $\tau_n \neq \tau_p$ .

To calculate the constants, Shockley and Read refer to Equations 2.23 and 2.24 and include the small deviations ( $\delta n$ ,  $\delta p$  and  $\delta f_t$ ) of excess carrier density from equilibrium values of  $n_0$ ,  $p_0$  and  $f_t$ . The equations are thus modified to:

$$U_{cn} = C_n [(1 - f_t) \delta n - (n_0 + n_1) \delta f_t] \quad (2.32)$$

$$U_{cp} = C_p [f_t \delta p + (p_0 + p_1) \delta f_t] \quad (2.33)$$

From the neutrality requirement

$$\delta p - \delta n = N_t \delta f_t \quad (2.34)$$

Since this considers  $f_t$  in equilibrium we have

$$f_t = \frac{1}{1 + (n_1/n_0)} = 1 - \frac{1}{1 + (p_1/p_0)} \quad (2.35)$$

Substitution leads to the solution to find the constants

$$A_{nn} = C_n \left[ \frac{n_1}{n_0 + n_1} + \frac{n_0 + n_1}{N_t} \right] \quad (2.36)$$

$$A_{np} = -C_n \frac{n_0 + n_1}{N_t} \quad (2.37)$$

$$A_{pn} = -C_p \frac{p_0 + p_1}{N_t} \quad (2.38)$$

$$A_{pp} = C_p \left[ \frac{p_1}{p_0 + p_1} + \frac{p_0 + p_1}{N_t} \right] \quad (2.39)$$

These definitions lead to the lifetimes:

$$\tau_p = \frac{\tau_{n0}(p_0 + p_1) + \tau_{p0} [n_0 + n_1 + N_t (1 + n_0/n_1)^{-1}]}{n_0 + p_0 + N_t (1 + n_0/n_1)^{-1} (1 + n_1/n_0)^{-1}} \quad (2.40)$$

$$\tau_n = \frac{\tau_{p0}(n_0 + n_1) + \tau_{n0} [p_0 + p_1 + N_t (1 + p_0/p_1)^{-1}]}{n_0 + p_0 + N_t (1 + p_0/p_1)^{-1} (1 + p_1/p_0)^{-1}} \quad (2.41)$$

### 2.1.3.3 Debuf Model

The SRH rate equations are second order, nonlinear differential equations. However they are generally solvable for limited conditions such as the high or low injection regimes. Debuf et. al. developed a general analytical solution to the SRH rate equations for arbitrary injection, doping concentration, defect concentration, energy level, trap density, and capture cross section without approximation (high injection vs. low injection) to give minority ( $\tau_1$ ) and majority ( $\tau_2$ ) carrier decay time [26]. The Debuf model addresses the entire decay processes from  $0^+ < t < \infty$  as an infinite sum of linear, mono-exponential terms. It thus represents the impulse response of an infinite number of linear systems [26]. Importantly, the work compares results from the new model to numerical solutions of the SRH model using a multitransient analysis. The time constants  $\tau_1$  and  $\tau_2$  are related to fundamental frequencies of the multitransient analysis by  $\tau_1 = 1/\lambda_1$  and  $\tau_2 = 1/\lambda_2$ .

Debuf uses a simple, first-order, nonlinear system as an example to explain the general process of solving the SRH equations.

$$\frac{dn(t)}{dt} = N_1 n(t) + N_2 n^2(t) \quad (2.42)$$

When  $N_2 = 0$ , the linear assumption classically made in the SRH model, the solution becomes the familiar  $n(t) = n(0)\exp(N_1t)$ . When  $n(0)$ , the initial injection conditions, are large, however, we must take nonlinearity into account. The exact solution, including the nonlinear term, results in:

$$n(t) = \frac{N_1 n(0) e^{N_1 t}}{[N_1 + N_2 n(0)] - N_2 n(0) e^{N_1 t}} \quad (2.43)$$

If it not possible to integrate Equation 2.42 directly, one method to solve this equation would be to look at the linear solution  $n(t) = n(0)\exp(N_1t)$  and substitute it into Equation 2.42. This results in a term  $\exp(2N_1t)$  on the right hand side, implying the solution may take the form  $n(t) = n(0)\exp(N_1t) + n_2\exp(2N_1t)$  [26]. Continuing this pattern, the solution takes the form of an infinite series of monoexponential terms.

$$n(t) = n_1 e^{N_1 t} + n_2 e^{2N_1 t} + n_3 e^{3N_1 t} + \dots \quad (2.44)$$

$$\frac{dn(t)}{dt} = n_1 N_1 e^{N_1 t} + n_2 2N_1 e^{2N_1 t} + n_3 3N_1 e^{3N_1 t} \dots \quad (2.45)$$

Substituting Equations 2.44 and 2.45 into Equation 2.42, with the observation that  $\exp(N_1t)$  etc. are linearly independent functions, reveals that the solution is a geometric series.

$$n(t) = n_1 e^{N_1 t} + \frac{N_2}{N_1} n_1^2 e^{2N_1 t} + \left(\frac{N_2}{N_1}\right)^2 n_1^3 e^{3N_1 t} + \dots \quad (2.46)$$

$$n(t) = \frac{n_1 e^{N_1 t}}{1 - \frac{N_2}{N_1} n_1 e^{N_1 t}} \quad (2.47)$$

Including the initial condition

$$n(0) = \frac{n_1}{1 - \frac{N_2}{N_1} n_1} \quad (2.48)$$

the solution becomes

$$n(t) = \frac{N_1 n(0) e^{N_1 t}}{N_1 + N_2 n(0) (e^{N_1 t} - 1)} \quad (2.49)$$

which is equivalent to the solution that is achieved from direct integration.

Next Debuf derives the fundamental frequencies for the single level defect system. The carrier continuity equations for the one-dimensional case are

$$\frac{dn(x,t)}{dt} = G_n - U_n + \frac{dJ_n}{dx} \quad (2.50)$$

$$\frac{dp(x,t)}{dt} = G_p - U_p + \frac{dJ_p}{dx} \quad (2.51)$$

where  $n(x,t)$  and  $p(x,t)$  are the time and spatially dependent electron and hole concentrations,  $G_{n,p}$  is the generation rate,  $U_{n,p}$  is the recombination rate and  $J_{n,p}$  is the current density. Equations 2.50 and 2.51 can be simplified assuming that the generation rate, diffusion components and electric field are considered negligible.

$$\frac{dn(t)}{dt} = -U_n \quad (2.52)$$

$$\frac{dp(t)}{dt} = -U_p \quad (2.53)$$

To simplify the notation, Debuf expresses the excess electron and hole concentrations  $\Delta n(t)$  and  $\Delta p(t)$  in terms of a normalized excess carrier concentration  $\Delta n_{nm}(t)$  and  $\Delta p_{nm}(t)$  where  $\Delta n_{nm}(0^+) = 1$  and  $\Delta p_{nm}(0^+) = 1$  [26].

$$\Delta n_{nm}(t) = \frac{\Delta n(t)}{\Delta n(0)} \quad (2.54)$$

$$\Delta p_{nm}(t) = \frac{\Delta p(t)}{\Delta p(0)} \quad (2.55)$$

Debuf rewrites the defect level electron concentration in terms of the equilibrium concentration  $N_t f_0$  and the departure from equilibrium  $N_t \Delta f(0)$  such that:

$$n(t) = \Delta n_{nm}(t) \Delta n(0) + n_{p0} \quad (2.56)$$

$$p(t) = \Delta p_{nm}(t)\Delta p(0) + p_{p0} \quad (2.57)$$

$$N_t f(t) = N_t \Delta f(t) + N_t f_0 \quad (2.58)$$

With the equilibrium electron occupancy of the defect level in terms of

$$f_0 = \frac{p_1}{p_{p0} + p_1} \quad (2.59)$$

$$f_0 = \frac{n_1}{n_{p0} + n_1} \quad (2.60)$$

where:

$$n_1 = N_c \exp \left[ - \left( \frac{E_c - E_t}{kT} \right) \right] \quad (2.61)$$

$$p_1 = N_v \exp \left[ - \left( \frac{E_t - E_v}{kT} \right) \right] \quad (2.62)$$

The charge neutrality relation thus rewritten in this notation becomes:

$$\Delta p_{nm}(t)\Delta p(0) = \Delta n_{nm}\Delta n(0) + N_t f(t) \quad (2.63)$$

The SRH equations can then be rewritten in normalized notation:

$$- \frac{d\Delta n_{nm}(t)}{dt} = \gamma_0 \Delta n_{nm}(t) - \sigma_0 \Delta p_{nm}(t) - C_n [\Delta p_{nm}\Delta p(0) - \Delta n_{nm}\Delta n(0)] \Delta n_{nm}(t) \quad (2.64)$$

$$- \frac{d\Delta p_{nm}(t)}{dt} = \alpha_0 \Delta p_{nm}(t) + \beta_0 \Delta n_{nm}(t) + C_p [\Delta p_{nm}\Delta p(0) - \Delta n_{nm}\Delta n(0)] \Delta p_{nm}(t) \quad (2.65)$$

$$\alpha_0 = C_p N_t \left\{ \frac{p_1}{p_{p0} + p_1} + \frac{p_{p0} + p_1}{N_t} \right\} \quad (2.66)$$

$$\beta_0 = C_p N_t \left\{ \frac{p_{p0} + p_1}{N_t} \right\} \quad (2.67)$$

$$\gamma_0 = C_n N_t \left\{ \frac{n_1}{n_{p0} + n_1} + \frac{n_{p0} + n_1}{N_t} \right\} \quad (2.68)$$

$$\sigma_0 = C_n N_t \left\{ \frac{n_{p0} + n_1}{N_t} \right\} \quad (2.69)$$

where the capture coefficient for electrons and holes are  $C_n = v_{thn}\sigma_n$  and  $C_p = v_{thn}\sigma_{np}$  respectively.

$$\begin{aligned} -\frac{d\Delta n_{nm}(t)}{dt} = & C_n N_t \left[ \Delta n_{nm}(t) \left( \frac{n_{p0} + n_1}{N_t} + \frac{n_1}{n_{p0} + n_1} + \frac{\eta_n(t)\Delta n(0)}{N_t} \right) \right] \\ & - C_n N_t \left[ \Delta p_{nm}(t) \left( \frac{(n_{p0} + n_1)}{N_t} + \frac{\eta_n \Delta p(0)}{N_t} \right) \right] \\ & + C_n N_t \left[ \frac{1}{N_t} [\Delta n_{nm}(t)\Delta n(0) - \Delta p_{nm}(t)\Delta p(0)] \times [\Delta n_{nm}(t) - \eta_n(t)] \right] \end{aligned}$$

$$\begin{aligned} -\frac{d\Delta p_{nm}(t)}{dt} = & C_p N_t \left[ \Delta p_{nm}(t) \left( \frac{p_{p0} + p_1}{N_t} + \frac{p_1}{p_{p0} + p_1} + \frac{\eta_p(t)\Delta p(0)}{N_t} \right) \right] \\ & - C_p N_t \left[ \Delta n_{nm}(t) \left( \frac{(p_{p0} + p_1)}{N_t} + \frac{\eta_p \Delta n(0)}{N_t} \right) \right] \\ & + C_p N_t \left[ \frac{1}{N_t} [\Delta p_{nm}(t)\Delta p(0) - \Delta n_{nm}(t)\Delta n(0)] \times [\Delta p_{nm}(t) - \eta_p(t)] \right] \end{aligned}$$

The charge neutrality relation gives:  $\eta_n = \Delta f(t)$  and the nonlinear term becomes

$$f^n(t) = - [\Delta n_{nm}(t) - \eta_n(t)] \eta_n(t) \quad (2.70)$$

Defining the following relationships:

$$\alpha = C_p N_t \left\{ \frac{p_1}{p_{p0} + p_1} + \frac{p_{p0} + p_1}{N_t} + \frac{\eta_p(t_0)\Delta p(0)}{N_t} \right\} \quad (2.71)$$

$$\beta = C_p N_t \left\{ \frac{p_{p0} + p_1}{N_t} + \frac{\eta_p(t_0)\Delta n(0)}{N_t} \right\} \quad (2.72)$$

$$\gamma = C_n N_t \left\{ \frac{n_1}{n_{p0} + n_1} + \frac{n_{p0} + n_1}{N_t} + \frac{\eta_n(t) \Delta n(0)}{N_t} \right\} \quad (2.73)$$

$$\sigma = C_n N_t \left\{ \frac{n_{p0} + n_1}{N_t} + \frac{\eta_n(t_0) \Delta p(0)}{N_t} \right\} \quad (2.74)$$

The differential equations,  $-\frac{d\Delta n_{nm}(t)}{dt}$  and  $-\frac{d\Delta p_{nm}(t)}{dt}$ , become:

$$-\frac{d\Delta p_{nm}(t)}{dt} = \alpha \Delta p_{nm}(t_0) - \beta \Delta n_{nm}(t_0) \quad (2.75)$$

$$-\frac{d\Delta n_{nm}(t)}{dt} = \gamma \Delta n_{nm}(t_0) - \sigma \Delta p_{nm}(t_0) \quad (2.76)$$

To find the characteristic frequencies we must solve the equation:

$$[D^2 + (\alpha + \gamma) D + (\alpha\gamma - \sigma\beta)] e^{-\lambda t} = 0 \quad (2.77)$$

The fundamental frequencies can thus be expressed as:

$$\lambda^2 - (\alpha + \gamma) \lambda + (\alpha\gamma - \sigma\beta) = 0 \quad (2.78)$$

Solving for the roots:

$$\lambda_1 = \frac{1}{2} \frac{\alpha + \gamma}{\alpha\gamma - \sigma\beta} \left[ 1 + \left( 1 - 4 \frac{\alpha\gamma - \sigma\beta}{(\alpha + \gamma)^2} \right)^{1/2} \right] \quad (2.79)$$

$$\lambda_1 = \frac{1}{2} \frac{\alpha + \gamma}{\alpha\gamma - \sigma\beta} \left[ 1 - \left( 1 - 4 \frac{\alpha\gamma - \sigma\beta}{(\alpha + \gamma)^2} \right)^{1/2} \right] \quad (2.80)$$

Where the lifetime is related to the fundamental frequencies by:  $\lambda_1 = 1/\tau_1$ ,  $\lambda_2 = 1/\tau_2$ .

By solving the SRH rate equations over a range of injection levels, Debuf et. al. allow SRH recombination to be measured by TRPL across a range of measurement conditions. In Chapter 4 this will allow the trap density in low-doped GaAs double heterostructures to be estimated from intensity dependent TRPL measurements.

## 2.2 Nanostructured Self-Assembled Materials

### 2.2.1 Fabrication of Self-Assembled Quantum Dots

Self-assembled quantum dots are typically fabricated via the molecular beam epitaxy (MBE) using the Stranski-Krastinov growth mechanism. In this mechanism, quantum dots form due to the strain and surface energy created by a mismatch in lattice constants between the semiconductor substrate and the deposited material. The most common example is InAs quantum dots grown on GaAs. InAs has a lattice constant of 0.6058 nm and GaAs has a lattice constant of 0.5653 nm [27]. When a very thin layer of InAs is deposited on the GaAs substrate, under appropriate conditions, the initial layer of InAs atoms follows the lattice periodicity of the existing GaAs. As the thickness of the InAs layer increases, the difference in their lattice constants leads to increasing strain. At a certain critical thickness, it becomes energetically favorable for the InAs to coalesce into small “islands;” the surface energy penalty paid for the formation of these islands is outweighed by the decrease in strain energy. Figure 2.4 shows a stack of self-assembled InAs QDs formed due to the differences in lattice constants.



**Figure 2.4:** Cross-sectional SEM of self assembled quantum dots stacked along the growth direction [4].

### 2.2.2 Band Structure in Nanostructured Materials

The confinement of carriers in a quantum dot gives rise to discrete energy levels instead of continuous energy bands like in bulk semiconductors. The behavior of

carriers in a nanostructure like a quantum dot is governed by the electron or hole's wave function. To determine the wave function, we must solve Schrödinger's equation for the boundary conditions of a particle in box. A particle's wave function can be described by the time-independent Schrödinger equation:

$$-\frac{\hbar^2}{2m} \frac{d^2\psi(z)}{dz^2} + V(z)\psi(z) = E\psi(z) \quad (2.81)$$

Assuming the energy barriers of the quantum dot are infinite, the probability of finding a particle outside of the dot is zero and the wave function,  $\psi$ , must be zero outside the boundaries of the dot. Incorporating the infinite potential assumption into the Schrödinger equation yields Equation 2.82 for the behavior of the particle within a well of width  $L_z$ .

$$-\frac{\hbar^2}{2m} \frac{d^2\psi(z)}{dz^2} = E\psi(z) \quad (2.82)$$

Here  $m$  is the particle mass,  $E$  is the energy,  $\hbar$  is Planck's constant normalized by  $2\pi$ , and  $\psi$  is the wave function of the particle. This equation is subject to the boundary conditions:

$$\psi = 0; \quad z = 0, L_z \quad (2.83)$$

and the general solution to this equation can be written:

$$\psi(z) = A\sin(kz) + B\cos(kz) \quad (2.84)$$

where A and B are constants and  $k = \sqrt{\frac{2mE}{\hbar^2}}$ . The symmetry of the cosine function and the condition that the wave function goes to zero at  $z=0$  implies that  $B = 0$ .

$$\psi_n(z) = A_n \sin\left(\frac{n\pi z}{L_z}\right) \quad (2.85)$$

Using this wavefunction and solving for energy, one finds a set of discrete allowed energies for the electrons in the quantum dot:

$$E_n = \frac{\hbar^2}{2m} \left( \frac{n\pi}{L_z} \right)^2 \quad (2.86)$$

where  $n$  is a positive integer:

$$n = 1, 2, 3, \dots \quad (2.87)$$

The discrete solutions to the equation for energy are considered eigenvalues, or eigenenergies. These discrete energy levels created by the confinement of the particle wave function allow for a range of possibilities to tailor light-matter interactions. For example, we can see that  $L_z$ , the length of the confinement, is in the denominator, meaning that tuning the size of the quantum dot can be used to tune the allowed energy levels for particles in the dot [28].

### 2.2.3 Energy Transport & Loss in Nanostructured Materials

One unusual property arising from the quantum mechanical understanding of solid state materials is that an electron can penetrate an energy barrier even if its energy is below the level of the barrier. This phenomena is called tunneling: a small but finite probability that a carrier is allowed to pass through a potential barrier between quantum dots or out of a quantum dot and into another region with sufficiently low band energy. This creates the possibility of energy transport or loss by way of tunneling. For the case where  $E > V_0$  the solution to the Schrödinger equation is:

$$\psi(z) = \begin{cases} A \exp(ik_1z) + B \exp(-ik_1z), & z < 0 \\ C \exp(ik_2z) + D \exp(-ik_2z), & z > 0 \end{cases} \quad (2.88)$$

where  $k_1^2 = 2mE/\hbar^2$  and  $k_2^2 = 2m(E - V_0)/\hbar^2$ . Making the solutions equal and continuous at the barrier creates a set of simultaneous equations [21]. To solve for the *transmission amplitude*,  $t$  and the *reflection amplitude*,  $r$  we set  $A = 1$ ,  $B = r$ ,

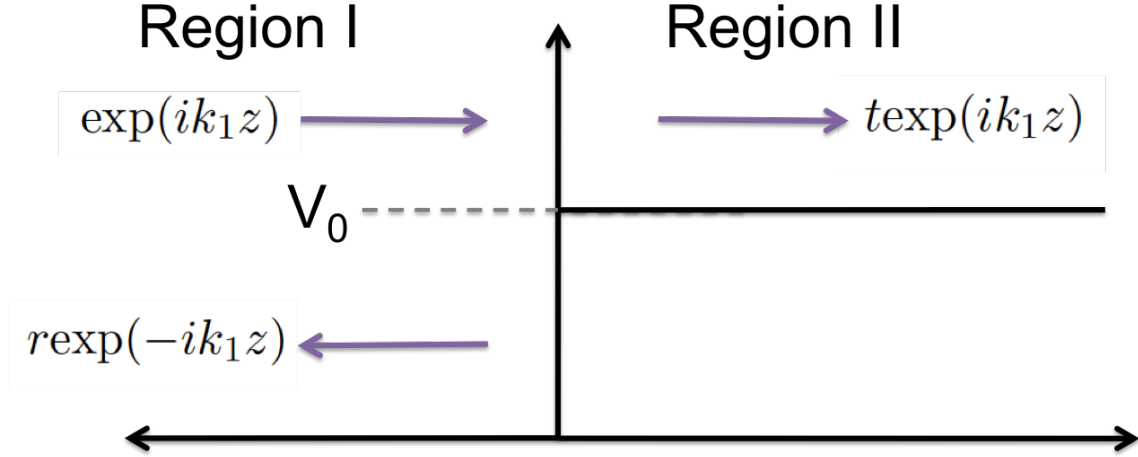


**Figure 2.5:** A potential step with a wave incident from the left. The potential is  $V = 0$  on the left,  $V = V_0$  on the right.

$C = t$  and  $D = 0$ . The logic of this can be seen in the Figure 2.5 [21]. Solving for the reflection and transmission amplitudes we get:

$$t = \frac{2k_1}{k_1 + k_2}, \quad r = \frac{k_1 - k_2}{k_1 + k_2} \quad (2.89)$$

When  $E < V_0$  the  $C \exp(ik_2 z)$  changes to  $C \exp(-\kappa_2 z)$  and the  $D \exp(-ik_2 z)$  changes to  $D \exp(+\kappa_2 z)$  where  $\kappa_2^2 = 2m(V_0 - E)/\hbar^2$ . This leads to the following solution for  $t$  and  $r$

$$t = \frac{2k_1}{k_1 + i\kappa_2}, \quad r = \frac{k_1 - i\kappa_2}{k_1 + i\kappa_2} \quad (2.90)$$

These tunneling coefficients are factored into the *flux transmission and reflection coefficients* which determine the actual current flow. For  $E < V_0$  there is no current flow, as would be expected classically, but when many square barriers are stacked, resonant tunneling and the formation of minibands become possible..

To deal with multiple barriers and more complex structures than just a step barrier, we turn to the T-matrix method. This method provides a facile approach to solving for the transmission and reflection coefficients in systems with large numbers of

barriers and wells, enabling us to understand energy transfer in superlattices and other nanostructured materials. The ‘‘T’’ in T-matrices stands for transfer and we define the relationships for tunneling above in terms of a transfer matrix T such that:

$$\begin{pmatrix} C \\ D \end{pmatrix} = T^{(21)} \begin{pmatrix} A \\ B \end{pmatrix} = \begin{pmatrix} T_{11}^{(21)} & T_{11}^{(21)} \\ T_{11}^{(21)} & T_{11}^{(21)} \end{pmatrix} \begin{pmatrix} A \\ B \end{pmatrix} \quad [21] \quad (2.91)$$

Here the superscripts on the T stand for the regions. This example illustrates transfer happening from region 2 to region 1. This can easily be extended to three regions

$$\begin{pmatrix} C \\ D \end{pmatrix} = T^{(21)} \begin{pmatrix} A \\ D \end{pmatrix}, \quad \begin{pmatrix} E \\ F \end{pmatrix} = T^{(32)} \begin{pmatrix} C \\ D \end{pmatrix} \quad (2.92)$$

which in turn gives:

$$\begin{pmatrix} E \\ F \end{pmatrix} = T^{(32)} T^{(21)} \begin{pmatrix} A \\ B \end{pmatrix} \equiv T^{(31)} \begin{pmatrix} A \\ B \end{pmatrix} \quad (2.93)$$

where  $T^{(31)} = T^{(32)} T^{(21)}$ . This can be extended for any number of regions, which makes it useful for understanding, predicting and designing the carrier transport properties of superlattices and more complex heterostructures. We can find the transmission and reflection amplitudes from the elements of  $T$

$$\begin{pmatrix} t \\ 0 \end{pmatrix} = T \begin{pmatrix} 1 \\ r \end{pmatrix} = \begin{pmatrix} T_{11} & T_{12} \\ T_{21} & T_{22} \end{pmatrix} \begin{pmatrix} 1 \\ r \end{pmatrix} \quad (2.94)$$

where  $r = -\frac{T_{21}}{T_{22}}$  and  $t = \frac{T_{11}T_{22} - T_{12}T_{21}}{T_{22}}$ . The  $T$ -matrix for this comes from the set-up of the wave functions:

$$T^{(21)} = \frac{1}{2k_2} \begin{pmatrix} k_2 + k_1 & k_2 - k_1 \\ k_2 - k_1 & k_2 - k_1 \end{pmatrix} \equiv T(k_2, k_1) \quad (2.95)$$

Here we assume the conditions  $E > V_0$  as we have shown previously; however when  $E < V_0$  we set  $k_2 = i\kappa_2$  [21].  $T$ -matrices and the underlying concept of tunneling

are useful in predicting material properties and designing devices reliant on energy transfer, for example quantum cascade lasers.

### 2.3 Colloidal Quantum Dot Materials

Colloidal quantum dots are chemically synthesized particles of semiconductor material typically from 2-6 nm in diameter. They are capped with organic ligands that passivate dangling surface bonds and keep the particles suspended in solution. Semiconductor shells of different materials and thicknesses can also be used to passivate dangling bonds and change the quantum confinement of charges in the CQD. Like self-assembled quantum dots, the principles of quantum confinement lead to important properties that give colloidal QDs a range of applications for optoelectronic devices, including photovoltaic cells.

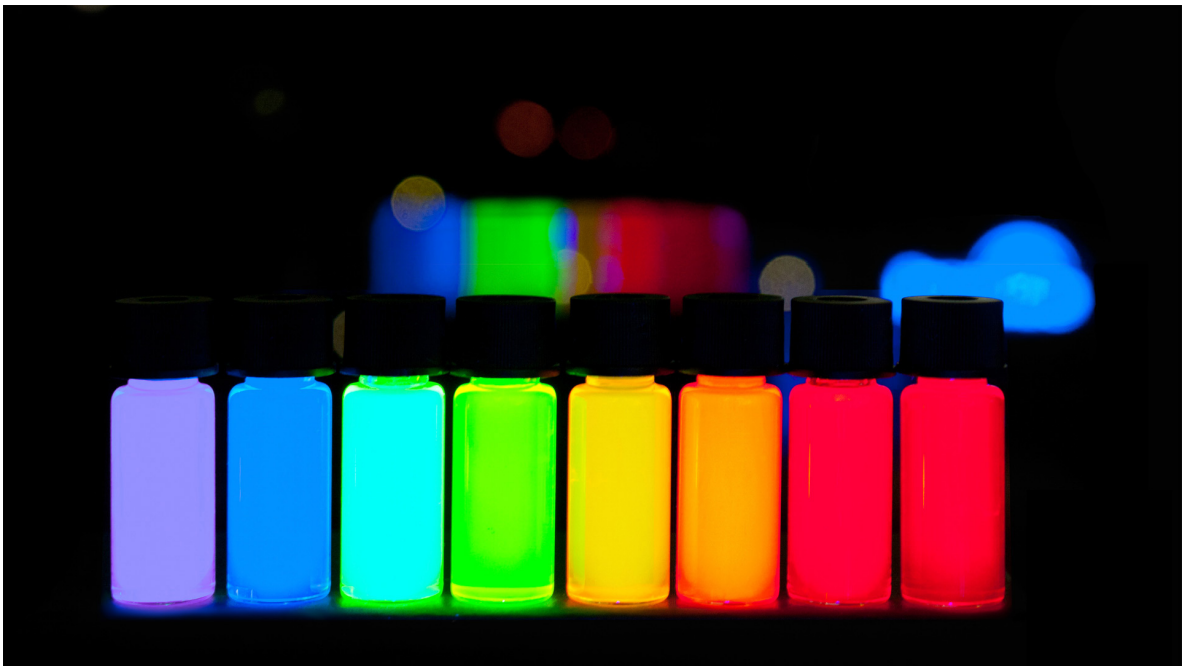


**Figure 2.6:** Solutions of CdSe colloidal quantum dots of varying sizes [5].

## 2.3.1 Fabrication of Colloidal Quantum Dot Materials

### 2.3.1.1 Synthesis

Ideally, synthesis creates colloidal quantum dots (CQDs) of high crystallinity and monodisperse size, where monodisperse is defined as a standard deviation in size of  $\sigma = \pm 5\%$ . Several different routes have been employed to achieve high quality CQDs. Early work by Murray et. al. advanced the synthesis of cadmium chalcogenide CQDs (CdS, CdSe, CdTe) by allowing narrower size distributions and improved particle crystallinity than previously achieved [29]. The Murray process, however, relied on dimethyl cadmium  $\text{Cd}(\text{CH}_3)_2$ , a toxic and pyrophoric precursor that was hazardous and difficult to work with. Peng et. al. advanced the state of the art for CQD synthesis in 2000 when they developed a synthetic route to monodispersed CdSe, CdS and CdTe quantum dots using cadmium oxide (CdO) as a precursor [30]. The stability and safety of the Peng procedure in comparison to the Murray procedure made CQD synthesis available to a much wider cohort of researchers and allowed easier commercialization of CQDs.

In the procedure developed by Peng et. al, CdO, trioctylphosphine oxide (TOPO) and tetradecylphosphoric acid (TDPA) were dissolved in a three neck flask and heated until the reddish brown CdO formed a colorless solution at about  $300^\circ\text{C}$ . TOPO acts as a coordinating solvent and the TDPA is the ligand that replaces oxygen and binds to the surface of the QD, solubilizing it. For CdSe CQDs, selenium was dissolved in trioctylphosphine (TOP) and injected into a three neck flask. Peng et. al. found that dissolving sulfur or tellurium in the TOP formed CdS or CdTe quantum dots, better than the previous methods using  $\text{Cd}(\text{CH}_3)_2$ .

An interest in telecommunications applications requiring emission and absorption of NIR or IR photons lead to the development of techniques for synthesizing lead chalcogenide quantum dots. For synthesis of lead chalcogenide quantum dots Hines et. al. prepared the lead oleate precursor by heating lead oxide (PbO) and oleic acid (OA) in a flask at  $150^\circ$  for one hour. A solution of TMS in octadecene (ODE) was then injected and the reaction was immediately allowed to cool [31]. This synthesis leaves

the lead chalcogenide quantum dots capped with oleic acid ligands.

### 2.3.1.2 Monolayer Film Formation

One advantage of using colloidal quantum dots in novel optoelectronic devices like next generation solar cells is the ease of processing. Soluble in a range of organic solvents, colloidal quantum dots can easily be formed into regular films using dip coating, spin coating, Langmuir-Blodgett, layer-by-layer (LbL), contact printing and drop casting [32]. Each method of film formation brings with it both challenges and advantages. As morphology of the film depends on the processing conditions and type of deposition, it is important to select a deposition technique that provides the right combination of speed, reliability and desired morphology.

Bulk films of colloidal quantum dots can be created through simple evaporation of the solvent in which they are suspended. With carefully chosen solvent boiling point and polarity, highly ordered bulk CQD films result due to slow evaporation of the solvent [33].

Transfer printing or contact printing, sometimes referred to as micro-contact printing if it involves micron scale patterning, involves the use of a stamp to physically place the CQD monolayers in a desirable formation. There are many variations on this technique but usually a poly-dimethylsilyloxane (PDMS) stamp is fabricated either with or without patterning. In one variation, a substrate is cleaned and treated with a self-assembled monolayer like ODTS to reduce the surface energy and improve lift off of the CQD monolayer. Often a polymer sacrificial layer is also added before the SAM is applied. The PDMS stamp is brought into contact with the CQDs monolayer and peeled off, lifting the monolayer with it. The stamp is then brought into contact with the substrate depositing the monolayer [34]. Some key factors to consider in applying this method are the swelling of PDMS in common organic solvents. To prevent this, parylene or photoresist SU-8 are employed to encapsulate the stamp. Additionally, a dry stamping method, involving creating a monolayer, letting it dry, and lifting it off to redeposit onto another substrate, can be performed [35]. Another method involves

segregation of the quantum dots on the surface of an immiscible liquid into a monolayer and using the PDMS to pick up the monolayer from the liquid and stamp onto the substrate [36].

## 2.3.2 Band Structure of Colloidal Quantum Dot Materials

### 2.3.2.1 Quantum Confinement

Similar to self-assembled quantum dots, the optoelectronic properties of CQDs are described by the particle in a box model and quantum confinement. In the case of CQDs the synthesis dictates that the time and temperature of the reaction are crucial conditions for determining the size of the particle and thus the confinement. When the size of the particle falls below the Bohr radius ( $a_r$ ) the charges become confined and both absorption and emission show size-dependent optoelectronic properties. Figure 2.7 shows the photoluminescence peaks of CQDs of various sizes and compositions. By varying the composition and the size of the CQDs, a large range of optoelectronic properties can be achieved.

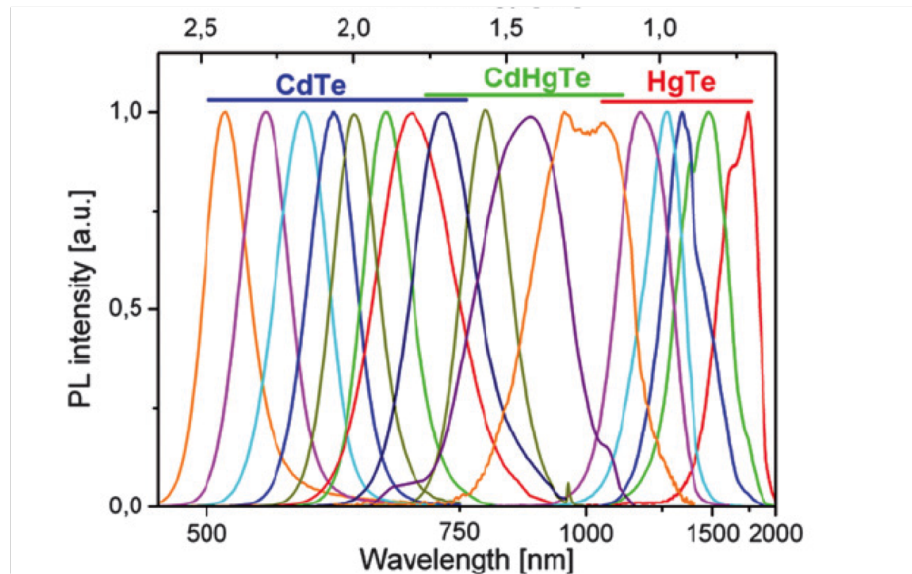


**Figure 2.7:** PL emission ranges of various sizes and materials of colloidal quantum dots [6].

Composition	PL Emission Range (nm)
CdS	365 - 465nm
CdSe	480 - 640nm
CdTe	510 - 720nm
PdS	850 - 1500nm

**Table 2.1:** Photoluminescence emission ranges for chalcogenide colloidal quantum dots.

The Bohr radius is determined by the crystal structure and chemical properties of the bulk materials. Materials with different compositions have different Bohr radii and thus when confined have different possible ranges of photon absorption and emission. Table 2.1 shows the typical achievable PL emission ranges for colloidal quantum dots of various common compositions.

### 2.3.2.2 Type I and Type II Band Alignment

In bulk semiconductors a type I band alignment occurs when one material has a conduction band edge that is lower, and a valence band edge that is higher, than the other material in the heterojunction, as seen in Figure 2.8. An example of a type I alignment is InGaAs/InP [21]. A type II alignment occurs when both the conduction band and the valence band of the material are lower than those in the other material, also shown in Figure 2.8. An example of a type II alignment is InAlAs/InP [21]. These alignments can be seen not only in bulk semiconductor materials but in layer structures of colloidal quantum dots and in the core/shell structures of CQDs.

When a CQD core/shell have a type I band alignment, the electron and hole wave function are confined to the core, increasing PL quantum yield QY as described above. When the CQD core has a type II alignment with it's shell, the electron and hole are spatially separated [33].

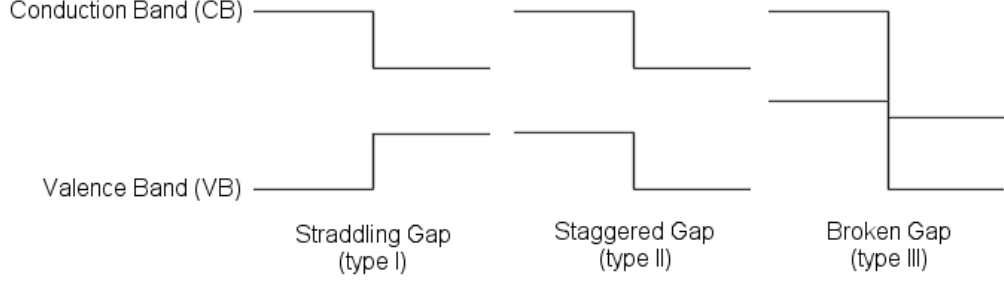


**Figure 2.8:** Types of heterojunction alignment [7].

### 2.3.3 Energy Transport & Loss in Colloidal Quantum Dot Materials

A key limitation and opportunity for advancement in creating photovoltaic devices from novel nano-structured materials such as colloidal quantum dots is the transport of carriers through the film. Carrier transport can occur due to drift from an electric field in a device or through diffusion. In neutral, unbiased films, diffusion dominates and is driven by the mobility and diffusion lengths in the material. The diffusion length is related to the carrier lifetime through  $L = \sqrt{D\tau}$  where  $D$  is the diffusivity constant and  $\tau$  is the carrier lifetime. CQD films have low mobility ( $10^{-3} - 10^{-2} \text{ cm}^2 \text{ V}^{-1} \text{ s}^{-1}$ ) compared to bulk semiconductors, which limits the photocurrent that can be extracted from a PV device. To improve photovoltaic performance for nano-structured materials, we must understand the energy transport processes that occur in CQD films and engineer them for improved transport. Recent reports have results demonstrating increases in carrier mobility up to  $1 - 30 \text{ cm}^2 \text{ V}^{-1} \text{ s}^{-1}$  by minimizing the CQD spacing through improved choice of ligands as a way to increase the electronic coupling [37]. Other work has shown that carrier lifetime is limited and device performance is more impacted by trap density, mediated by surface passivation, encouraging additional work to improve CQD surface conditions [38].

### 2.3.3.1 Surface Passivation

Colloidal quantum dots have a high surface area to volume ratio that results in a large number of un-passivated bonds/orbitals on the surface of the dot. These un-passivated surfaces can act as traps to carriers, causing non-radiative recombination [39]. Deep trap state radiative emission can also be observed in the PL spectra as a hump or tail at wavelengths longer than the core PL emission peak. Various organic and inorganic ligands have been used to passivate the surface traps. A common issue is that long insulating ligands are highly effective at passivating the surface traps but reduce the film conductivity, while short conductive ligands are often less effective at surface passivation. Research in this area seeks to find a solution to this apparent trade-off. Long insulating ligands promote more solubility in organic solvents and thus more easy processing for device fabrication. Typical organic ligands are oleic acid or TDPA [33].

An inorganic shell around the core of the quantum dot is another strategy for passivating the surface of CQDs [33]. The band alignment of the shells in relation to the core of the CQD determines the optoelectronic properties of the core/shell CQD. Quantum confined states isolated from surface states typically improve PL efficiency and occur, for example, when the band gap of the shell is larger than the band gap of the core. An example is CdSe/ZnS where CdSe (1.74 eV) is the core and ZnS is the shell (3.54 eV). The inclusion of an inorganic shell can increase the PL efficiency by an order of magnitude [33].

Colloidal quantum dot core shell structures are found to tolerate lattice mismatch much more than flat systems. The CdSe/ZnS system has a 12% lattice mismatch yet very high quantum yield (QY), while more matched systems can often show quenching of PL. It appears that the thicker the shell, the greater the possibility for the formation of defects that trap charges and cause non-radiative recombination [33]. A more important contributor to PL QY is the energy offset between the conduction and valence bands of the core and shell [33]. Smaller offsets between the core and shell allow the electron wavefunction to “sample” the surface and potentially “see” a

trapped hole and recombine non-radiatively. In contrast, for a material like CdSe/ZnS the offsets are large and the electron is tightly confined to the core, unable to overlap with surface defects and more likely to recombine radiatively [33].

### 2.3.3.2 Förster Resonance Energy Transfer

An important energy transfer mechanism in nano-structured materials is Förster resonance energy transfer (FRET). FRET is a dipole-dipole energy transfer process that is heavily dependent on the distance between the donor and acceptor species. First studied and applied in fluorescent dye molecules, it's sensitivity to distance allows measurement of sub-nanometer distances between chemical species based on the efficiency of the energy transfer. FRET assumes two oscillators in which there is weak coupling between the donor and acceptor. The acceptor must have allowed electronic transitions and the degree of coupling is given by the spectral overlap called the *Förster overlap integral*,  $J$ , where:

$$J = \int f_D(\lambda) \epsilon_A(\lambda) \lambda^4 d\lambda \quad (2.96)$$

in which  $f_D(\lambda)$  is the normalized donor emission spectrum,  $\epsilon_A(\lambda)$  is the acceptor molar extinction coefficient, and  $\lambda$  is the wavelength. The efficiency of energy transfer can be expressed in terms of this overlap integral in the form:

$$E = \frac{1}{1 + \left(\frac{R}{R_0}\right)^6} \quad (2.97)$$

where:

$$R_0^6 = \frac{9Q_0 \ln(10) \kappa^2 J}{128\pi^5 n^4 N_A} \quad (2.98)$$

in which  $Q_0$  is the quantum yield of the fluorescence,  $\kappa^2$  is the *dipole orientation factor*,  $n$  is the refractive index, and  $N_A$  is Avogadro's number [40], [41].

The FRET distance  $R_0$  is typically around 2nm for dye and CQD systems. FRET can be observed between CQD donor and acceptors with two distinct size distributions or within a single nominally mono-dispersed population [42].

While energy transport mechanisms like drift and diffusion dominate the electronic behavior of bulk materials, at the nanoscale mechanisms such as FRET, trap state recycling and tunneling play a more significant role. Carriers can also undergo various recombination processes that influence the dynamics of energy transport in nanoscale materials. Processes such as Shockley-Read-Hall or defect recombination, Auger recombination, surface recombination and photon recycling change the optoelectronic properties in nanostructured materials. It is next shown how time-resolved photoluminescence and controlled structure on nanometer lengths scales can be used to gain a better understanding of how these mechanisms are interrelated and can be used to enable next generation optoelectronic devices.

## Chapter 3

### OPTICAL CHARACTERIZATION OF PHOTOVOLTAIC MATERIALS

This section details the experimental techniques used to probe energy transfer dynamics in semiconductor materials. It includes the theory and practical use of various equipment as well as the fundamentals of analyzing TRPL data.

#### 3.1 Photoluminescence

Photoluminescence spectroscopy is a technique to measure the energy of material band gaps, excited states and defect states. In photoluminescence spectroscopy, an exciting laser impinges on the sample and photons with energy greater than the band gap are absorbed in the material, creating electron-hole pairs. Carriers then relax to the lowest energy state and, if an electron and hole wave function overlap and optical selection rules permit radiative recombination, they recombine to emit a photon. PL is often used to identify impurities in semiconductors because impurity levels have very specific energies [43]. The emitted photons are captured and measured, often with a charge coupled device (CDD). PL can only measure radiative recombination and is most useful for materials that have a high PL efficiency, like direct band gap semiconductors such as III-V materials.

#### 3.2 Time Resolved Photoluminescence

Time resolved photoluminescence is an optical characterization technique that relies on a time-correlated measurement of the light emitted from a semiconductor material upon radiative recombination of electron-hole pairs. A pulsed laser is used to excite charge carriers to an excited state. At some time later, based on the properties of the material, the carriers recombine, emitting photons. By measuring the time between

each excitation pulse and each emitted photon over millions of excitation cycles, a histogram is created that defines the lifetime of excited carriers in the material. The energy gap between excited carriers and the carriers they recombine with - for example the band gap of a semiconductor, or the energy gap between the excited states and the valance band - determines the energy/wavelength at which the light is emitted. A steady state PL spectrum of this energy can provide information about excited states, trap states and band gap energy of a material. Taking the histogram of the TRPL results and fitting to an exponential model such as  $I_{PL} = A_1e^{-t/\tau_1} + A_2e^{-t/\tau_2}$ , extracts characteristic lifetimes  $\tau_1$  or  $\tau_2$  that represent the lifetime when  $1/e$  of the radiative carrier recombination has occurred.

### 3.2.1 Mira-900 femtosecond laser

The Mira-900 femtosecond Ti:Sapphire laser is a tuneable, femtosecond pulsed laser, with a repetition rate of 76MHz and wavelength tuneable from 750 nm-950 nm. Both continuous wave (CW) and mode-locked operation are possible with this system. The Mira-900 is pumped with a 532nm 5W Verdi CW source laser. The Mira works on the principle of population inversion. The laser contains a high reflector, a gain medium and an output coupler. Light from the pump beam (created by the Verdi) illuminates the gain medium, exciting carriers. The light emitted when these carriers relax radiatively is coupled to modes of the cavity such that the light reflects off the high reflector and passes through the gain medium, a titanium doped sapphire crystal, again and again. The arrangement of mirrors and the beam path in cavity allows this to occur. The cavity feedback allows stimulated emission to occur, resulting in amplification of the light at a specific frequency/wavelength [44].

For amplification to occur the wavelength must satisfy the condition that exactly one integer number of half wavelengths must fit between the mirrors. The birefringent filter in the Mira allows us to select the wavelength for which this condition is satisfied. The individual wavelengths are also called longitudinal modes [44].

There are several different approaches to achieve pulsed laser operation, all of which require some type of optical shutter, also called a modulator, to open at precisely the correct time to allow a pulse of light to escape. In active mode-locking the modulator is a device whose frequency is precisely controlled to be equal to the time it takes for the pulse to bounce between end mirrors and make one round-trip of the cavity. In passive mode-locking a saturable absorber material allows the light to escape only when the intensity is high enough. The Mira is passively mode-locked using a principle called the optical Kerr effect [44].

Refractive index is a property of materials that affects the speed at which radiation travels through a material. Refractive index of a material is most commonly changed by changing the composition of the material, however in the optical Kerr effect the light itself changes the refractive index. At intensities of light that are sufficiently high, the electric fields from the light distort the atoms in the material changing its refractive index. The distortion of the refractive index creates a lens when high intensity light passes through the optic. The lens narrows the width of the beam allowing it to pass through a narrow slit. Only the presence of a high intensity, mode-locked beam allows the light to create the lens and pass through the slit [44].

The average power measured by mode-locked lasers does not fully describe the energy and fluence characteristics of the light. The laser emits ultra-short pulses containing a large number of photons, and then nothing for a long period. Pulse energy describes the average power divided by the repetition rate of the laser. Fluence is the amount of energy traveling through a given area. It is calculated by dividing the laser pulse energy by the effective focal spot area.

### **3.2.2 Second Harmonic Generator System**

The harmonic generator system takes the low-energy laser pulses and outputs doubled pulses through a nonlinear process. The SHG performs this task through a lithium triborate (LBO) crystal. Second harmonic generation, also called frequency doubling, is a nonlinear process that takes two photons of lower energy and converts

them into one high energy photon. For example, we use the SHG to convert 800 nm pulse light from the Mira-900f into 400 nm light to excite samples with a band gap in the visible spectral range. Since the Mira is tunable, the output of the SHG system is also tunable within the range of approximately 360-450 nm.

### 3.2.3 ConOptics Pulse Modulation system

The Mira-900 Ti:Sapphire laser has a repetition rate of 76 MHz, which is equivalent to one pulse every 13.2 ns. However, many of the material systems of interest have lifetimes longer than 13.2 ns. To investigate those systems with TRPL one must increase the time interval between pulses by suppressing intermediate pulses. This approach is called pulse picking. To accomplish pulse picking we use a ConOptics Pulse Modulation system. The system includes an electro-optic pulse modulator, a pulse generator and a voltage source. The pulse generator takes an electrical pulse train from the photodiode output of the Mira, converts it to a known frequency and, based on the setting of a thumbwheel, sends an output signal of the desired frequency. The voltage source takes the frequency from the pulse generator and generates a series of voltage pulses that it sends to the pulse modulator.

The pulse modulator is a type of transverse-field Pockels cells, which functions based on the change of birefringence based on the applied voltage. The incoming light from the Mira is horizontally polarized and the crystal axis is aligned along the x-axis of the modulator and  $45^\circ$  to the incoming light. The voltage source is used to apply an electric field that induces a change in the refractive index of the material to shift polarization to vertical. Pulses escape the modulator when no bias is applied and are blocked when the bias is applied, changing the polarization [45].

The pulse modulator, Model 350-160 KD\*P (potassium dideuterium phosphate) Series Modulator, is optimized for use with a Ti:Sapphire laser with output between 700 nm and 1064 nm. It can provide output from single pulses up to 30 MHz for mode locked lasers, with input from lasers up to 100 MHz and has a variable delay of 8 ns [45].

The extinction ratio is the ratio between the optical power at maximum and minimum output and is 500:1 in the ConOptics system as defined by the crystal. Adjustment of the beam alignment through the modulator allows optimization of the extinction ratio. If the incoming beam is misaligned, or not completely horizontally polarized, pulses that were intended to be blocked will leak through. Insertion loss - the loss of transmission power through the modulator - is estimated by the manufacturer ConOptics to be 85% [45].

### 3.2.4 Spectrometer

Photoluminescence from the sample is collected by a Princeton Instruments Acton SpectraPro i2500, typically 0.5m in length. The concept of the spectrometer is shown in the cartoon in Figure 3.1. Gratings within the spectrometer create dispersion in the incoming PL, causing the different wavelengths of light to refract at different angles. This spreads out the wavelengths in space, ordered by wavelength, allowing the spectral composition of the PL to be imaged on a camera. Three gratings, with groove density of 150, 600, and 1100 or 1200 grooves per millimeter, allow a range of energy resolutions to be achieved. A stepping motor and microprocessor controlled positioning allows repeatable and precise positioning of the gratings.

The spectrometer is used to image the PL onto a liquid nitrogen cooled charge-coupled device (CCD). The CCD is a silicon-based detector with a two dimensional array of pixels. Photons impinging on the array excite charges in the pixels, which are then read by the electronics of the spectrometer as intensity at each pixel. A side-port mirror diverts PL reflected off the grating from the CCD to an exit-port in the spectrometer. The slit at the exit port allows for the selection of a narrow range of wavelengths for spectrally-selective TRPL.

### 3.2.5 Avalanche Photodiode

An avalanche photodiode is a type of PIN photodiode that makes use of impact ionization of carriers at high reverse bias voltages. When a photo-generated carrier

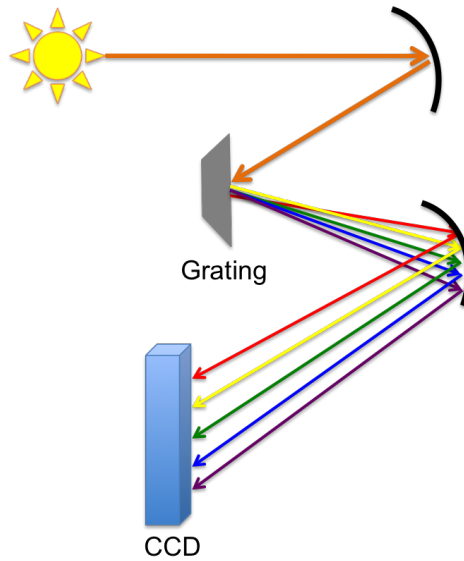


**Figure 3.1:** Cartoon of the functional concept of a spectrometer.

releases its energy to multiple carriers it creates a cascade, or avalanche, of carriers and thus a detectable current. The gain of an APD is usually in the range of 100 times and it is operated below but close to the breakdown voltage of the semiconductor.

Importantly, the APD is designed to register single photon events, and has a period of time, called dead-time, after a photon event occurs in which the APD returns to a ready condition. In order to get an accurate count of the photons striking the detector, the incoming photoluminescence must be kept within a certain range of intensities. If the PL is too intense an artifact called pile up is likely to occur in which more than one photon can hit the detector per cycle. The detector typically responds to the first photon and thus does not see the second photon due to the dead time. This makes the PL lifetime appear artificially short. To avoid pile up, the counts per second on the detector should be kept at 1-5% of the repetition rate registered by the trigger diode. For example, if the repetition rate of the laser is 76 MHz or  $7.6 \times 10^7$  Hz, the counts on the APD should be no greater than  $3.8 \times 10^6$  counts per second.

A key performance metric of an APD is the dark counts of the detector. At room temperature there is always a bath of phonons present in the material that comprises

the detector and some of these phonons have enough energy to excite a carrier and register a photon event even in the absence of photons. The number of counts that register on the APD even with no light shining on the detector defines the dark counts. Dark counts act like a background signal and can limit the signal-to-noise ratio of the APD when measuring materials with low PL signals. Dark counts can range from 35 counts per second to 1000's of counts per second.

Another important metric of an APD is the response time. The response time of the APD defines the time resolution possible and limits the lifetimes that can be measured to no shorter than 100-300 ps in most cases. Timing resolution varies with the manufacture of the APD. For decays times that are close to the instrument response, this signal can be compensated for in data analysis, but only up to a point - usually only when the instrument response is no more than 60% of the measured lifetime.

To expand the applications of time-correlated single photon counting (TCSPC), different types of detectors can be employed. For example, a silicon APD shown in Figure 3.2, like the PDM avalanche photodiode from Micro Photon Devices, has a wavelength range from 400 nm-900 nm with a 50% photon detection efficiency at 550 nm. Peltier cooling allows for reduced dark counts on the order of 100 counts per second. Timing resolution is approximately 35 ps full width half max. We also employed a Perkin-Elmer Single Photon Counting Module (SPCM-AQRH) with a detection range of 400 nm-1000 nm, with an efficiency of up to 65% at 650nm and a time resolution of approximately 300 ps.

For wavelengths in the range of 900 nm - 1700 nm an InGaAs/InP single photon avalanche photodiode (SPAD) is used. Detectors with a smaller band gap energy, like the InGaAs SPAD, are required to sense low-energy photons, however, they have much higher dark counts, on the order of 1000 counts per second. This produces a worse signal to noise ratio than the PDM detector. Due to this, the InGaAs SPAD is available in free running or gated mode. Gating allows the detector to be synchronized with a trigger source, often the output of the laser pulses with a variable delay, and improves the signal-to-noise of the detector by reducing dark counts. Cooling the detector below

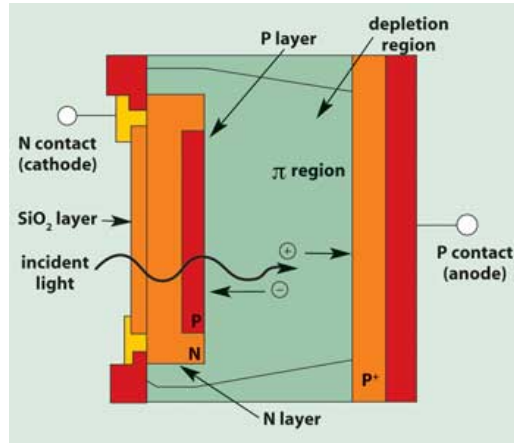


**Figure 3.2:** Schematic of an avalanche photodiode [8].

what is possible with Peltier coolers is also a possible route to reduced dark counts though in open atmosphere a detector cooled below the dew point will have problems with condensate formation.

Alternatives in measurement of time-resolved photoluminescence measurements are photomultiplier tubes and streak cameras. Photomultiplier tubes, as represented in Figure 3.3, are vacuum tubes with an input window, photocathode, focusing electrodes, electron multiplying dynodes and an anode. Light entering through the input window excites electrons in the photocathode, which are focussed by the electrodes on the the electron multiplying dynodes. The dynodes, a type of vacuum tube, produce secondary electrons when struck by the exciting electrons. This process is repeated by the succeeding dynodes, amplifying the signal. The amplified electrons are collected by the anode.

### 3.2.6 PicoHarp 300 Time-Correlated Single Photon Counting system

Time-correlated single photon counting is a preferred approach to performing TRPL measurements, particularly for nanostructured materials in which one may be working with a low flux of emitted photons. This approach creates a histogram of

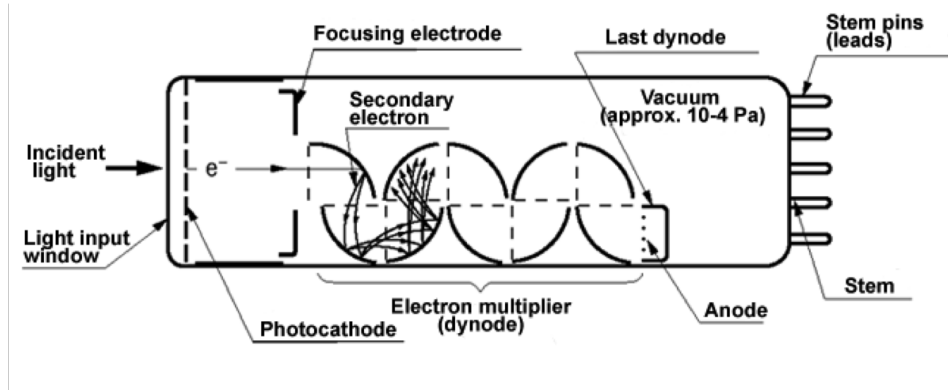


**Figure 3.3:** Schematic of a photomultiplier tube [9].

photon events precisely registered in time. Measuring the decay profile from a single event poses the challenge that systems one may desire to study only emit single photons per excitation event, or occur too fast for typical electronics to resolve. In TCSPC, a photon event registered at the detector is converted into an electrical signal. The time difference between the signal from the photon and the excitation pulse is then calculated. Fast electronics in the PicoHarp perform a reverse start-stop calculation. In this calculation, an observed photon emission event starts the clock, the next observed excitation pulse stops the clock, and the true start-stop time for the excitation cycle is computed from the repetition rate of the laser [46]. The PicoHarp Time Correlated Single Photon Counting system provides the electronic control for TSCPC measurement. The PicoHarp 300 is an electronic component which takes a signal from a trigger diode or fast photodiode and the signal from the avalanche photodiode. The PicoHarp 300 has two synchronous, independent, 4 ps resolution input channels with 65536 bins. Additionally, it has an adjustable input delay and can be controlled via a desktop computer using USB 2.0 [46].

In TCSPC, the time resolution is provided by the response of the detector, where the timing accuracy is limited by the uncertainty that the detector introduces when converting a photon to an electrical signal. Timing uncertainties are defined as the Full Width Half Maximum of the timing distribution, the instrument response function.

### 3.2.7 Data analysis

Our TCSPC data is initially analyzed using the FluoFit software that can read the data files from the PicoHarp. FluoFit can be used to perform several types of fitting to extract the characteristic lifetime from a data set. FluoFit can fit data with decay laws of up to four exponentials, stretched exponentials, Gaussian or Lorentzian behavior. It can deconvolve data with instrument response functions (IRF) or perform a simple tail fit if the IRF is short in comparison to the decay time of the material system. The FluoFit package also comes with a range of error analysis tools which will not be described here.

#### 3.2.7.1 Exponential Fitting

The histogram of a TCSPC experiment most often results in an exponentially decaying function. To extract a physically meaningful characteristic lifetime from the results we must fit to an exponential model. Often a simple, single exponential model, such as  $I_{PL} = A_1 e^{-t/\tau_1}$ , is appropriate. Figure 3.4 shows an example of a sample with a single exponential decay law. This occurs when a single carrier relaxation process dominates in the material. If multiple processes occur on similar time scales and with similar frequency, a multiple exponential mode such as  $I_{PL} = A_1 e^{-t/\tau_1} + A_2 e^{-t/\tau_2} + A_3 e^{-t/\tau_3}$  can be justified. Importantly, the  $\chi^2$  value of the least squares fitting will always improve with additional fitting parameters, even if those parameters are not meaningful. It is crucial to fit with the minimum required fitting parameters and to justify the physical mechanism behind each lifetime within a multi-exponential model.

The primary algorithm that FluoFit and other data analysis packages use is the iterative least squares method. The software is programmed to generate an initial Monte Carlo estimate of lifetimes. It creates a synthetic dataset from the estimate and then calculates the squares of the residuals between the original dataset and the synthetic dataset. It iterates the process, changing the characteristic lifetime used to generate the synthetic dataset, ultimately returning the lifetime that minimizes residuals.

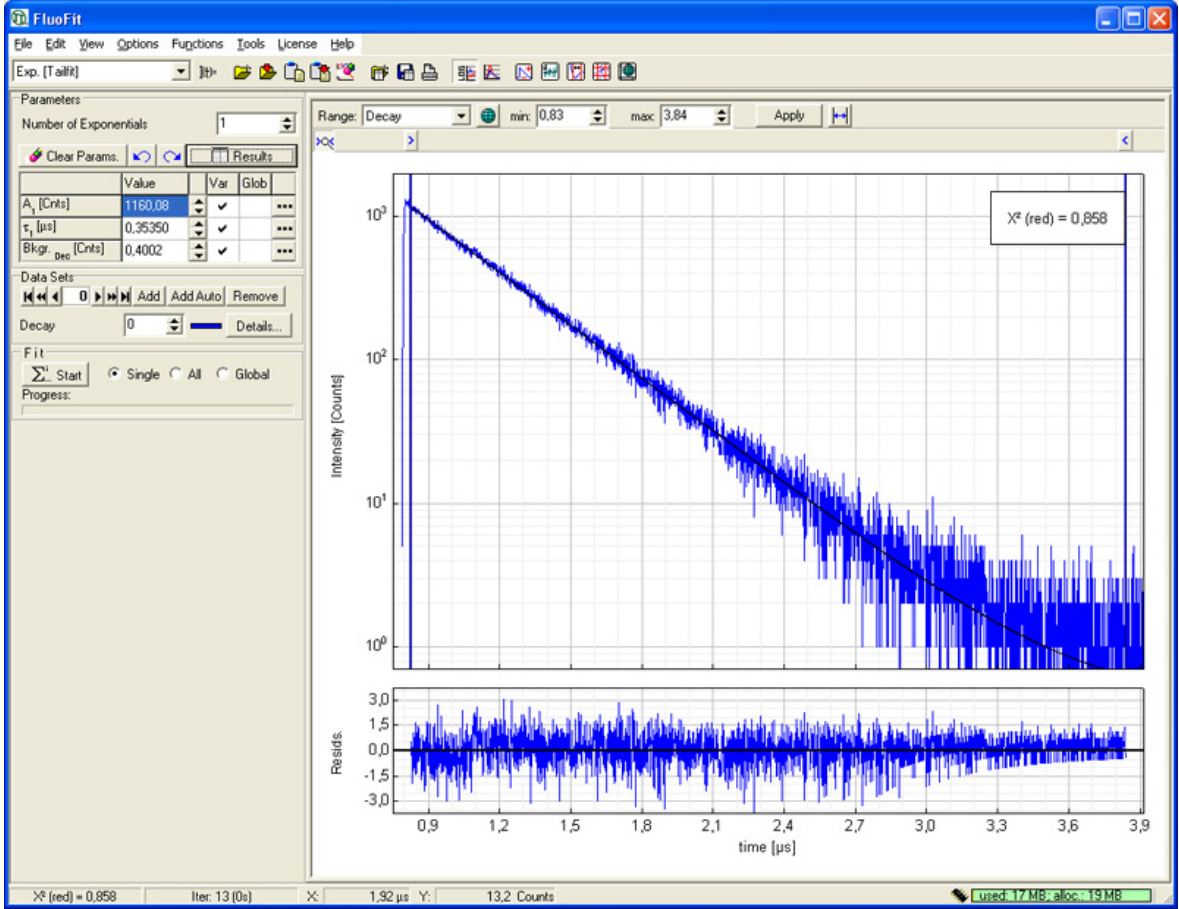


**Figure 3.4:** This figure shows an example of a simple, single exponential tail fit [10].

### 3.2.7.2 Deconvolution of IRF

The histogram of lifetimes that result from a measurement is actually the convolution of the response of the avalanche photodiode and the material behavior. This can be represented as  $f(t) = \int_0^t g(t') d(t-t') dt'$  where  $f(t)$  is the measured decay curve,  $g(t')$  is the instrument response and  $d(t)$  is the undistorted decay law of the system [47]. Generally it is the response behavior of the detector that limits the time resolution of the measurement. For systems in which the lifetime of the material is on the same order of magnitude as the response of the detector, the data analysis protocol must take into account the instrument response function (IRF). If the IRF is short in comparison to the lifetime of the measured PL, a tail fit - a fit in which only the tail

of the decay is taken into account without including the IRF - can be performed. If the IRF is on the order of 60% of the lifetime of the PL the IRF must be measured and accounted for in the data fitting. Measurement of the IRF is conducted without a sample, the spectrometer passes only the pulses from the laser to the avalanche photodiode (APD). The resultant histogram is the response function of the APD and can be removed through a deconvolution algorithm from the measured sample data to get the decay law that represents physical processes in the system [48]. An example of fitting to a bi-exponential model with a deconvolution performed in Fluofit is shown in Figure 3.5.

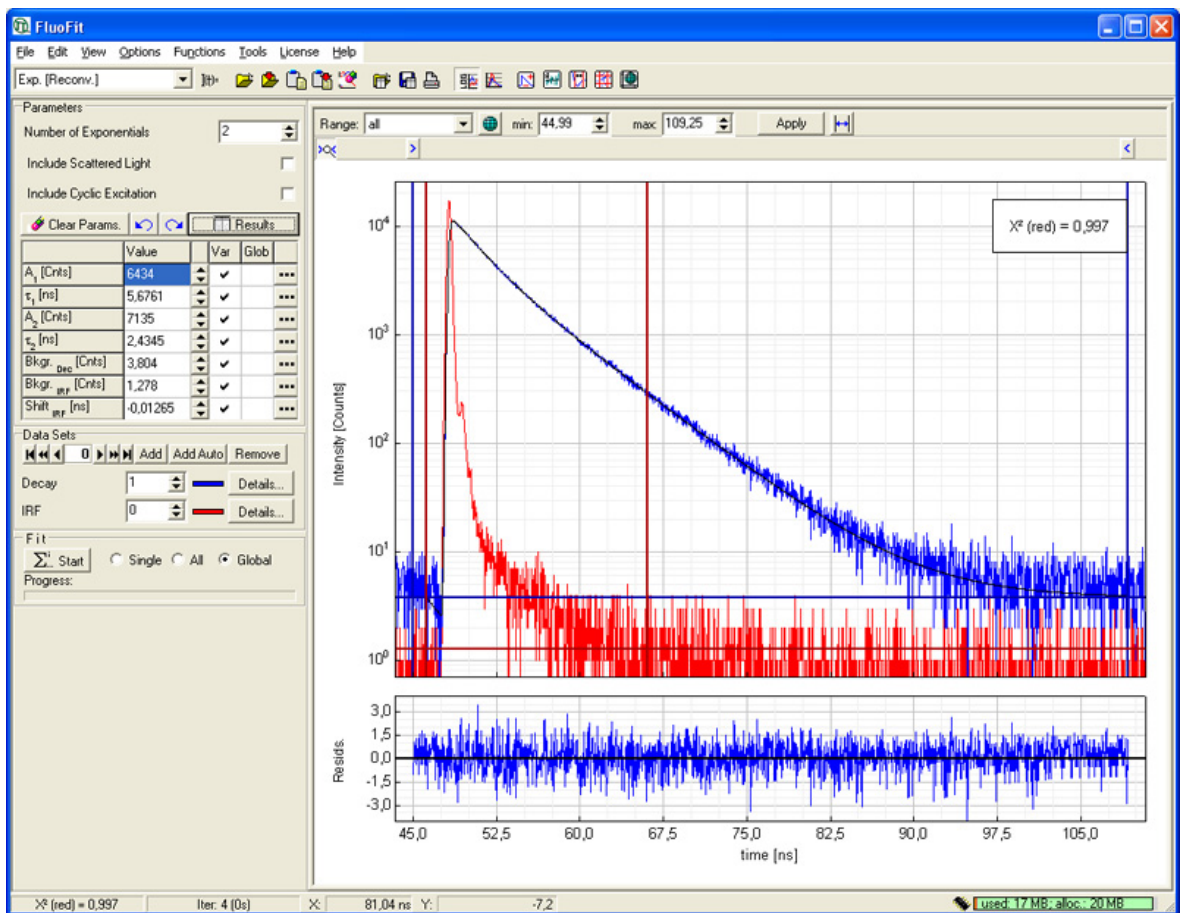


**Figure 3.5:** This figure shows an example of a double exponential fitting model with a deconvolution of the instrument response function (red) from the data (blue) [10].

## Chapter 4

### TIME-RESOLVED PHOTOLUMINESCENCE FOR ASSESSING MATERIAL QUALITY IN SEMICONDUCTORS

#### 4.1 Application of TRPL to Quantification of Trap Densities in GaAs

Minority carrier lifetime is a critical material property for the performance of photovoltaic devices. While the measurement of minority carrier lifetime is often presumed to be straightforward, it can be dependent on measurement conditions and sample conditions, resulting in conflicting or ambiguous results. Techniques like photoconductance measurements are often performed under strictly identical measurement conditions to obtain a reliable and comparable measurement of minority carrier lifetime that can be compared from sample to sample. This does not provide the depth of insight into carrier dynamics that can be achieved by looking at the lifetime dependence on measurement conditions.

Time-resolved photoluminescence was used with varying laser fluence conditions to develop an understanding of trap saturation in low doped GaAs for high efficiency PV applications. By going beyond a single measurement of minority carrier lifetime and characterizing how the material's measured PL lifetime changes with intensity of the exciting laser, we can extract an estimate for trap density, a proxy for material quality.

This work is motivated by the need to produce large quantities of high quality semiconductor material for PV applications. Deployment of PV devices at large scales will require fast growth rates. However, increasing growth rates typically lead to an increase in defect density and a reduction of minority carrier lifetime. By measuring the PL lifetime of GaAs grown at several different rates, via MOCVD, and building a model of trap saturation and the intensity dependence of the measured lifetime, we

have developed a tool for understanding how growth rate influences trap density in GaAs for photovoltaic devices.

## 4.2 Gallium Arsenide Double Heterostructures Grown by MOCVD

There are several mechanisms for non-radiative recombination in any semiconductor, including surface, defect and Auger recombination. A wide band gap window layer passivates the surface states, reducing surface recombination and a thick active region makes the surface to volume ratio low, suppressing any remaining surface recombination that takes place to a negligible fraction of the overall recombination. We use very low doping to reduce Auger recombination to a negligible level.

Gallium arsenide (GaAs) samples following this design were grown by metal organic vapor deposition (MOCVD) by our collaborators at Veeco MOCVD. The double heterostructure architecture, shown in Figure 4.1, consisted of InGaP window layers and a 10  $\mu\text{m}$  active region. The samples were grown at 14  $\mu\text{m}/\text{hr}$ , 28  $\mu\text{m}/\text{hr}$  and 56  $\mu\text{m}/\text{hr}$  using as Veeco K475 As/P tool. The samples were nominally undoped with a background doping of  $1 \times 10^{15} \text{ cm}^{-3}$  dominated by carbon and oxygen, making the material lightly p-type.

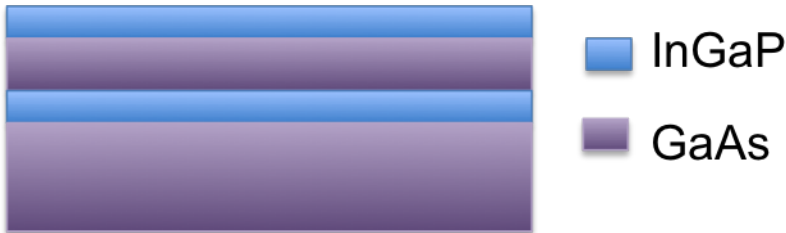


**Figure 4.1:** Schematic of the GaAs double heterostructure sample with 100 nm InGaP window layers and 10  $\mu\text{m}$  active region

## 4.3 Intensity-dependent time-resolved photoluminescence

Time-resolved photoluminescence was conducted using the Mira-900 pulsed laser at a wavelength of 800 nm (1.55 eV) and using the ConOptics pulse selection system to

select a repetition rate of 155 kHz. The laser was focused onto the sample at a 60° angle using a f=100 mm achromatic lens and calibrated neutral density filters were used to control the intensity for intensity-dependent measurements. Photoluminescence emitted from the DH samples was collected with an Olympus Plan FL M 10x microscope objective. The PL was spectrally resolved using a Princeton Instruments Acton Spectra Pro i2500 spectrometer with a liquid nitrogen cooled CCD. Time-resolved data was collected using a Perkin-Elmer silicon avalanche photodiode.

Figure 4.2 shows the TRPL decay curve for the sample grown at the slowest rate, 14  $\mu\text{m/hr}$ , at both high and low excitation laser fluences. Under-low fluence conditions, often referred to as low-injection conditions, the decay curve follows a mono-exponential decay law and can be fitted to  $I(t) = A_1 e^{-t/\tau_1}$  with a low  $\chi^2$  error. Under high-fluence, or high-injection, conditions, however, the decay curve shows a bi-exponential decay law and is most accurately fitted to  $I(t) = A_1 e^{-t/\tau_1} + A_2 e^{-t/\tau_2}$ . This is due to majority carrier recombination at high carrier densities [49]. Majority carrier recombination is negligible under low-fluence conditions. The fast component of the decay curve can be attributed to majority carrier recombination and the slower component can thus be ascribed to minority carrier recombination. The cross-over condition between high and low fluence/injection is  $\Phi \approx \frac{2p_0}{\alpha\tau_n}$ , where  $p_0$  is the acceptor concentration,  $\tau_n$  is the minority carrier lifetime, and  $\alpha$  is the extinction coefficient [50].

To analyze our TRPL results over a range of intensities we consider the longer lifetime component of the bi-exponential decay. The long lifetime decay corresponds to the minority carrier lifetime that would be measured under low injection conditions. Several types of recombination can contribute to measured surface recombination. The surface recombination component of lifetime can be discounted because of the InGaP window layer and the thickness of the active region.

Auger recombination is also known to occur at high injection levels. The Auger recombination rate is  $\frac{1}{\tau_A} = C_p p^2$  where  $C_p$  is the Auger recombination coefficient, which for GaAs is  $C_p = 1.6 \times 10^{-29} \text{ cm}^6 \text{ s}^{-1}$ , and where  $p$  is the acceptor concentration, also referred to as  $N_a$ . Since we have very low doped materials ( $N_a = 1 \times 10^{14} \text{ cm}^{-3}$ ), Auger

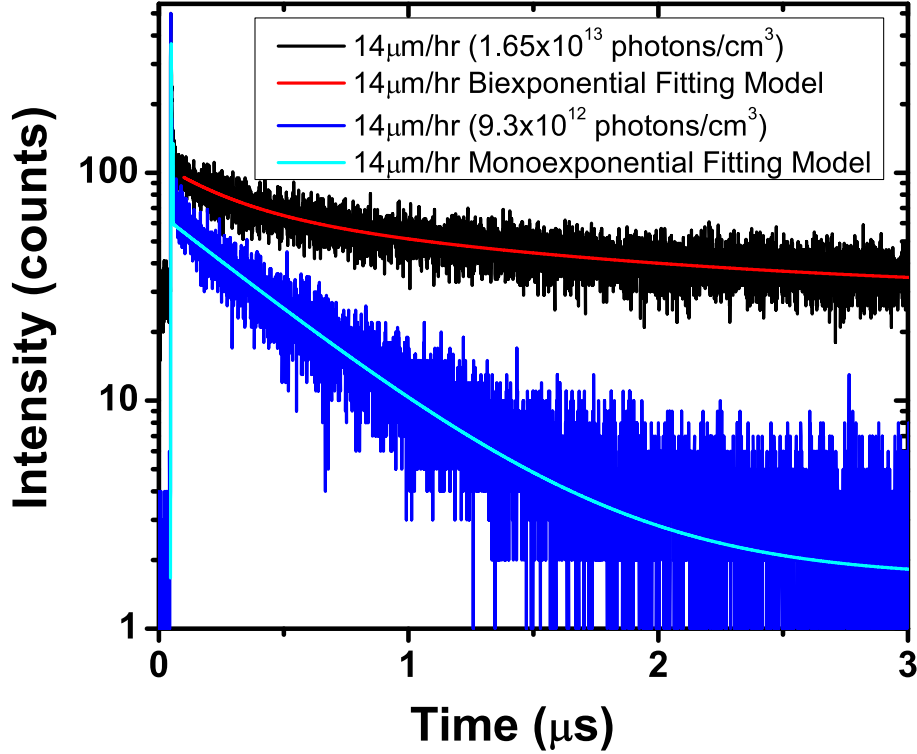


**Figure 4.2:** Fluence dependent time resolved photoluminescence decay curves for MOCVD GaAs grown at 14  $\mu\text{m/hr}$  [11].

recombination is not a significant recombination pathway for these samples.

Photon recycling is reemission and self-absorption of carriers in direct band-gap semiconductors. Photon recycling has an impact on the radiative lifetime through the relationship:  $\frac{1}{\tau_{PL}} = \frac{1}{\tau_{nR}} + \frac{1}{\phi\tau_R}$ , where  $\phi$  is the photon recycling coefficient,  $\tau_R$  is the radiative lifetime, and  $\tau_{nR}$  is the non-radiative lifetime [18]. This leads to a lengthening of the measured PL lifetimes in systems in which photon recycling is a dominant phenomena. The radiative lifetime is related to doping and the radiative recombination coefficient  $B$  by  $\frac{1}{\tau_R} = \frac{1}{Bp_0}$ . This relationship leads to a calculated lifetime of 5  $\mu\text{s}$  for GaAs with this doping level. Any effect of photon recycling would lengthen this lifetime, however, the longest observed lifetimes are 1.6  $\mu\text{s}$ , evidence that

non-radiative recombination is the limiting rate.

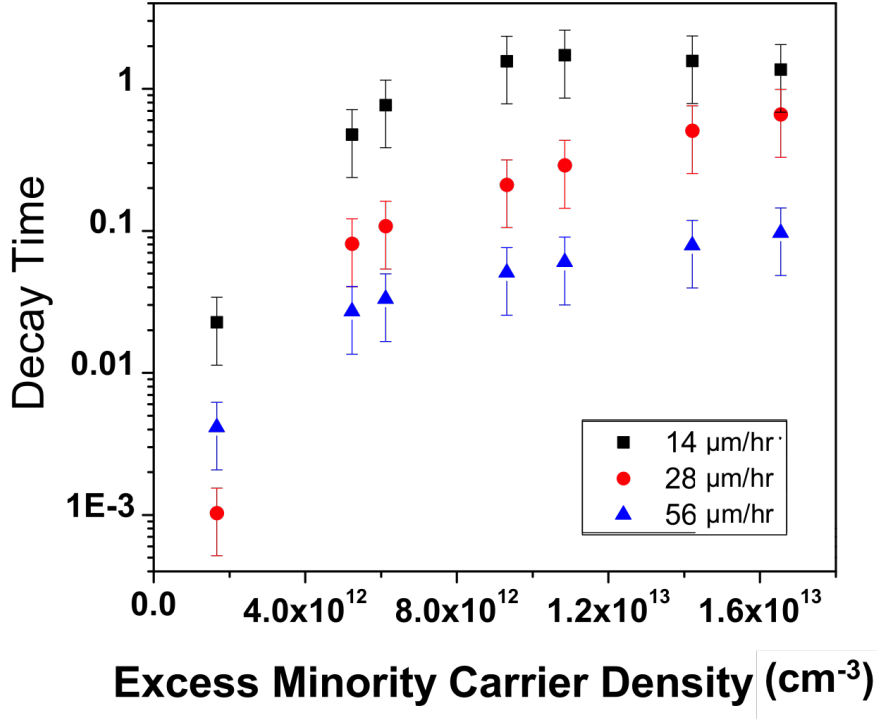


**Figure 4.3:** Measured minority carrier decay time as a function of excess minority carrier density as calculated from laser fluence [11].

Figure 4.3 shows that the long lifetime component, which should correspond to the minority carrier lifetime. However, the long lifetime component has a dependence on excitation fluence. Prior work suggests that the intensity dependence is likely related to trap state saturation, and thus it should be possible to use the intensity dependence to extract information about the traps from the TRPL results. To extract such information we turn to the statistical model developed by Shockley-Read-Hall and a solution to the SRH rate equations developed by Debuf et. al. [25]. As previously described, Debuf et. al. solved the SRH rate equation analytically over a range of

injection levels and temperatures. The result is the relationship:

$$\lambda_1 = \frac{1}{2} \frac{\alpha + \gamma}{\alpha\gamma - \sigma\beta} \left[ 1 + \left( 1 - 4 \frac{\alpha\gamma - \sigma\beta}{(\alpha + \gamma)^2} \right)^{1/2} \right] \quad (4.1)$$

$$\lambda_1 = \frac{1}{2} \frac{\alpha + \gamma}{\alpha\gamma - \sigma\beta} \left[ 1 - \left( 1 - 4 \frac{\alpha\gamma - \sigma\beta}{(\alpha + \gamma)^2} \right)^{1/2} \right] \quad (4.2)$$

which is detailed in the derivation in Chapter 2. The lifetimes are related to the fundamental frequencies ( $\lambda_1, \lambda_2$ ) by:  $\lambda_1 = 1/\tau_1, \lambda_2 = 1/\tau_2$ , where the two time constants ( $\tau_1$  and  $\tau_2$ ) correspond to the minority and majority carrier lifetimes, the two time constants that appear in a fit to the experimental data [25]. We fit this model to fit to our lifetime results as a function of laser fluence with  $N_t$ , the number of traps, as the fitting parameter. Other material parameters were estimated from literature for GaAs, including the effective density of states in the valance band  $N_v = 9.51 \times 10^{18} \text{ cm}^{-3}$ , the effective density of states in the conduction band  $N_c = 4.37 \times 10^{17} \text{ cm}^{-3}$ , and the thermal velocity of electrons and holes,  $v_{thn} = 4.4 \times 10^7 \text{ cm s}^{-1}$  and  $v_{thp} = 1.8 \times 10^7 \text{ cm s}^{-1}$ . We assumed the traps were the EL2 anti-site defect, which is the most common defect in MOCVD-grown GaAs [51], giving an estimated trap energy of 0.85eV. The capture cross sections for the EL2 defect in GaAs are  $\sigma_n = 5 \times 10^{-15} \text{ cm}^2$  and  $\sigma_p = 5.5 \times 10^{-17} \text{ cm}^2$  [52]. The radiative recombination coefficient is  $B = 1.788 \times 10^{10} \text{ cm}^3 \text{ s}^{-1}$ , and the Auger recombination coefficient is  $C = 1.6 \times 10^{-29} \text{ cm}^6 \text{ s}^{-1}$ . The doping density for these samples was estimated at about  $N_a = 1 \times 10^{15} \text{ cm}^{-3}$ , which is also the equilibrium carrier concentration for majority carriers,  $p_0$ . From the Law of Mass Action the equilibrium minority carrier concentration  $n_0 = n_i^2/N_a$ , where the intrinsic carrier concentration  $n_i = 2.1 \times 10^6 \text{ cm}^{-3}$  for GaAs [27].

We fit this model to the data for each sample using  $N_t$  as a fitting parameter, which allowed an estimate of the trap densities for each growth condition. Table 4.1 lists the values of  $N_t$  obtained from these fits. The lines in Figure 4.4 show the results of our fit to the experimental data. The fit agrees very well with the data, but a small quantitative disagreement is observed for the lowest laser intensity. We propose

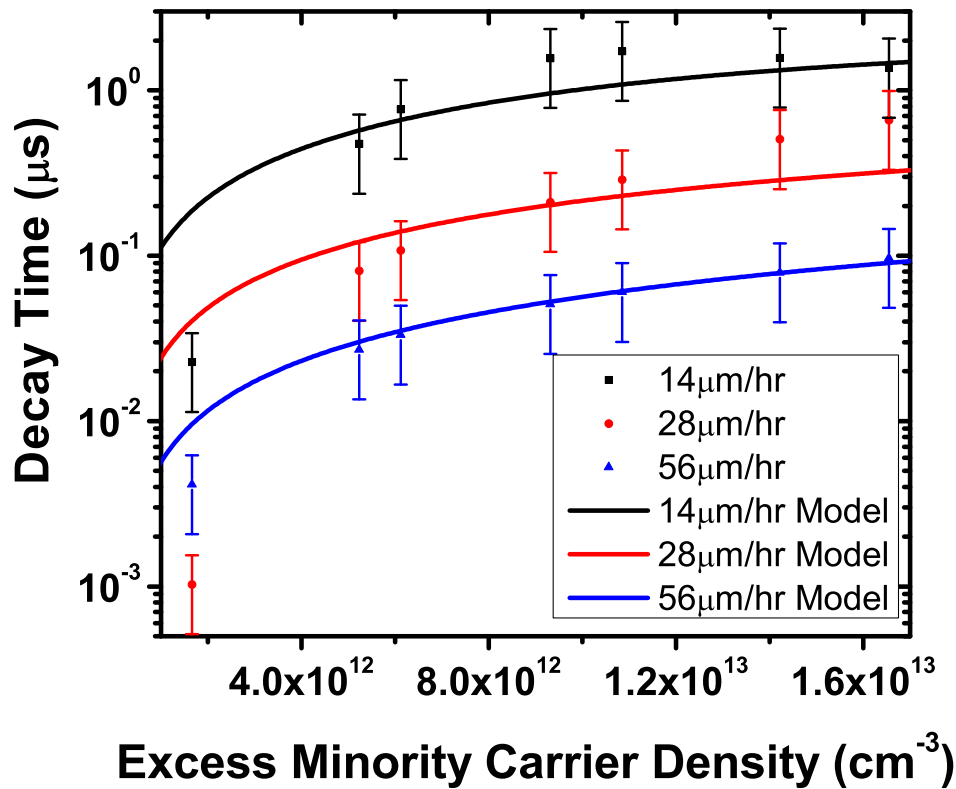


**Figure 4.4:** Measured minority carrier decay time as a function of excess minority carrier density as calculated from laser fluence. Solid lines show the fit calculated from the Debuf et. al. model [11].

two possible origins for this disagreement. First, although the relative laser fluences are precise, there is some uncertainty in the calculation of the absolute laser fluence because the spot size on the sample cannot be precisely measured. The slope of the result of the Debuf model is steepest at the lowest laser fluences, and thus this portion of the data is most sensitive to any uncertainty in absolute laser fluence. Second, our implementation of the Debuf model assumed a single trap type, but other trap species are likely present in very low densities. Although a very low density of these additional trap species would be easily saturated with increasing laser fluence, the assumption of a single trap species may begin to fail at the very lowest laser fluences measured. Additional investigation of the low fluence regime will be necessary to understand

Sample	Trap Density
14 $\mu\text{m}/\text{h}$	$8 \times 10^{13} \pm 2 \times 10^{13} \text{ cm}^{-3}$
28 $\mu\text{m}/\text{h}$	$3.5 \times 10^{14} \pm 8.75 \times 10^{13} \text{ cm}^{-3}$
56 $\mu\text{m}/\text{h}$	$1.7 \times 10^{15} \pm 4.25 \times 10^{14} \text{ cm}^{-3}$

**Table 4.1:** Estimated trap density for GaAs/InGaP double heterostructures grown by MOCVD at varying rates.

this small discrepancy between the model and experimental data. All uncertainty introduced by this discrepancy is captured in the error bars on the trap state densities obtained from the fit.

Using the estimated trap density results from the Debuf model, we calculate the expected lifetime, using the linear SRH model, as a function of doping density  $p_0$ . The result is shown in Figure 4.5. As doping approaches device-relevant levels, the difference in minority carrier lifetime between the fastest and slowest growth samples becomes negligible. This suggests that faster growth rates, at least within the range tested here, could be used without decreasing PV device performance as a result of shorter minority carrier lifetime.

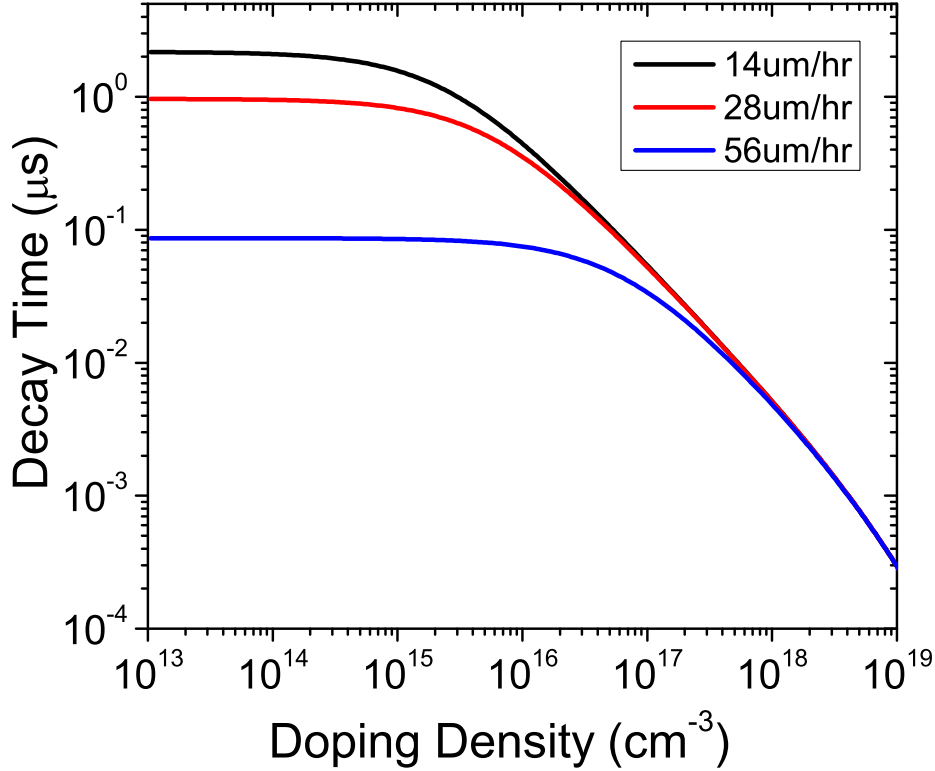


**Figure 4.5:** Minority carrier lifetime as a function of doping computed using the estimated trap densities and the SRH model [11].

The results presented in this section show that a deeper and more quantitative understanding of material properties can be gained from intensity-dependent time-resolved photoluminescence measurements. To implement this analysis we isolated Shockley-Read-Hall recombination as the dominant non-radiative mechanism by careful sample design. We applied an SRH-based model to intensity-dependent TRPL results to develop an understanding of how increasing fluence fills traps. The application of the model overcomes the ambiguity in interpreting minority carrier lifetime from time resolved data in materials that show a sensitivity to measurement conditions such as laser intensity. The approach allows for quantitative information on trap state density to be extracted via non-destructive testing and data analysis, providing a new approach

to rapid characterization of material quality.

## Chapter 5

### ENERGY TRANSFER DYNAMICS IN SELF-ASSEMBLED InAs QUANTUM DOT ErAs NANOINCLUSION SUPERLATTICES

In the previous chapter we demonstrated the use of time-resolved photoluminescence (TRPL) to understand carrier dynamics in semiconductors. By carefully isolating energy transfer mechanisms and controlling the measurement conditions we can extract more information than from minority carrier lifetime alone. In this chapter, we expand upon this concept to isolate the mechanism of carrier transfer between indium arsenide (InAs) quantum dots (QDs) and erbium arsenide (ErAs) nanoinclusions.

#### 5.1 Nanocomposite Materials

Nanoparticles embedded in a bulk semiconductor form a class of materials called nanocomposites. Nanocomposite materials have been studied for use in thermoelectric devices, THz photomixers, photoconductive switches and tunnel junctions because the inclusion of semi-metal nanoparticles in a host semiconductor can be used to tailor a range of optoelectronic properties, including recombination rate [53], [54], [55], [56]. Photoconductive switches, for example, which can be used to detect or generate THz radiation, require a short recombination lifetime to allow fast recovery. Photoconductive switches consist of a dipole antenna bridged by a photoconductive material with high dark resistivity. A short, optical pulse excites carriers in the photoconductive material, increasing the conductivity. The current is measured only when the photoconductive switch is on and illuminated. In addition to short recombination lifetimes and high dark resistivity, photoconductive switches should have a band gap energy appropriate for optical excitation and high carrier mobilities [57].

Erbium arsenide (ErAs), one of the more well-studied materials for nanocomposite applications, is a rock-salt structured semi-metallic material that forms self-assembled metal nanoparticles when co-deposited by MBE within a GaAs host [55], [58]. Prior work has demonstrated that incorporation of ErAs metal nanoparticles (MNPs) can prevent photoluminescence (PL) from both the bulk GaAs and embedded InAs QDs by providing a pathway for carrier capture and nonradiative relaxation [59]. The rates of carrier capture depend on the density of ErAs MNPs and the spacing between ErAs layer [60], [61]. Intensity-dependent optical experiments also indicate the ErAs MNPs do not contain saturable states. However, both the electronic structure of the ErAs MNPs and the mechanisms of carrier transfer remain poorly understood. Understanding the electronic structure and mechanisms of carrier transfer is critical for rational engineering of nanocomposite structures to tailor optoelectronic properties for device applications. We probed the electronic structure and optoelectronic properties of ErAs MNPs by characterizing carrier transfer between InAs QDs and the ErAs MNPs with steady-state and time-resolved PL.

## 5.2 Sample Structure

Collaborators at the Air Force Research Laboratory grew four samples containing InAs QDs and ErAs MNPs via MBE. As seen in the cartoon depicted in Figure 5.1, each sample contained 8 periods of a repeat structure that consisted of a layer of InAs QDs, a GaAs spacer layer with thickness  $d$ , an ErAs MNP layer and a second GaAs spacer layer. The InAs QDs were fabricated by depositing 2.5 monolayers (ML) of InAs on a GaAs substrate. The difference in lattice constants causes islands of material to form, creating the QD structure described in Chapter 2. Between samples the thickness of the first GaAs spacer layer was varied to explore the transfer of energy or charge between the InAs QDs and the ErAs MNPs. Layers of thickness 8, 10, 12, and 40 nm were deposited on top of the InAs QD layer. The ErAs MNPs were fabricated using a 1.6 ML deposition of ErAs. The second GaAs layer thickness was chosen to maintain a constant 80 nm period between all samples and was sufficiently thick to ensure that

carrier transfer through the first spacer layer was the dominant process.

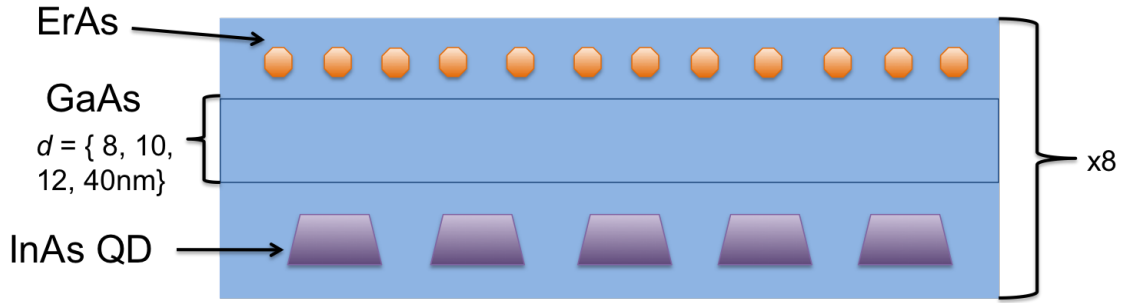


**Figure 5.1:** Schematic physical structure of one period of InAs quantum dots and ErAs nano-inclusions.

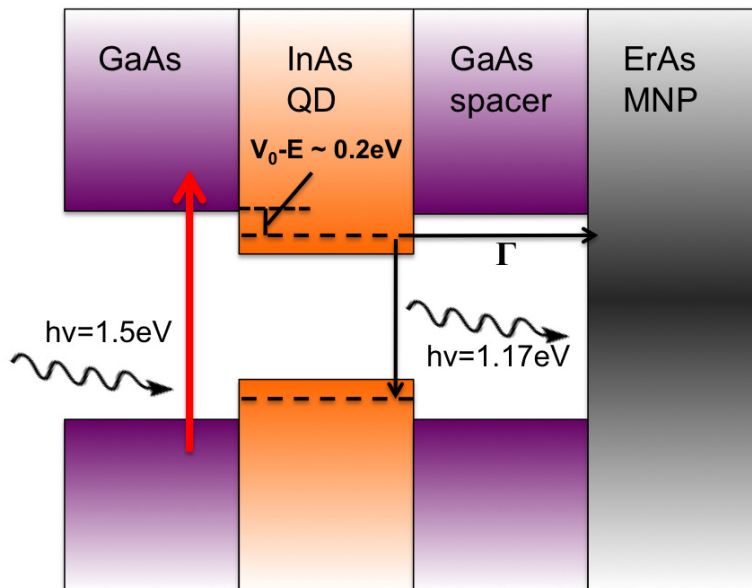


**Figure 5.2:** Schematic band diagram of one period of InAs quantum dots and ErAs nanocomposite [12].

The electronic structure of a single period of the sample is shown in Figure 5.2. Photoluminescence experiments consisted of exciting carriers over the bandgap of GaAs (1.5 eV), as seen in Figure 5.2. This allows optically generated carriers to relax into both the ErAs MNPs and the InAs quantum dots. Photoluminescence was spectrally resolved at the 1060nm (1.17 eV) ground states of the InAs quantum dots. This allows

isolation of the carrier transfer mechanisms as a change in QD lifetime under various conditions that affect carrier transfer.

### 5.3 Temperature Dependent Photoluminescence and Time-Resolved Photoluminescence

Many carrier transfer processes rely on the presence of phonons. To determine the influence of phonon-dependent carrier-transfer processes we performed temperature-dependent PL and TRPL. Temperature-dependent, steady-state PL was measured using a 532nm frequency-doubled Nd:YAG CW laser and Bomem FTIR. The temperature was varied from 4 K to 100 K under a constant excitation intensity of 1 W/cm<sup>2</sup>.

Figure 5.3 shows the steady-state PL results for the  $d = 40$  nm sample. InAs QD photoluminescence intensity decreases with increasing temperature, which has previously been observed in quantum dot systems and is attributed to thermal escape of carriers from the QDs [62]. This result does not allow us to distinguish between carrier escape to the conduction band of the GaAs or the ErAs MNPs, though either process could be the result of thermally-driven carrier excitation and therefore result in temperature dependent PL behavior. We also observe that total PL decreases with decreasing distance between the InAs QDs and the ErAs MNPs.

Time-resolved PL (TRPL) was acquired using a femtosecond pulsed Ti:Sapphire laser operating at 800 nm and 76 MHz repetition rate with a 150 fs pulse width. The emitted PL was collected using a 50 X (N.A. = 0.65) microscope objective and was spectrally-resolved using a 0.75 m monochromator. The excitation laser was filtered out of the collected PL with a 800 nm long pass filter. Time-resolved data was collected using a PicoQuant time-correlated single photon counting system and an InGaAs single photon avalanche photodiode (SPAD). PL decay data were obtained at temperatures ranging from 10 K to 70 K and at fluences from 6.8 mJ/cm<sup>2</sup> to 141 mJ/cm<sup>2</sup>. TRPL could not be collected on the  $d = 8$  nm sample, or for temperatures over 70 K, because the PL intensity dropped below the level of dark counts on the InGaAs SPAD.

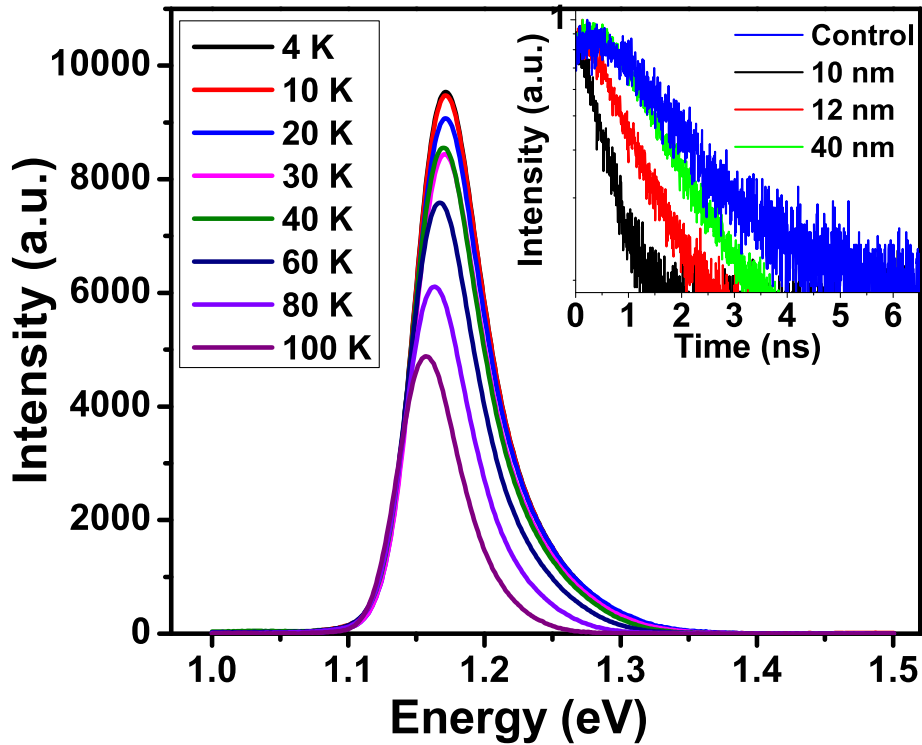


**Figure 5.3:** Temperature dependent photoluminescence of InAs self-assembled QDs. Inset: PL decay curves of InAs QD measured at 1060 nm and 10 K for four samples including the Control sample without ErAs MNPs, and GaAs spacer layers of 40 nm, 12 nm, and 10 nm [12].

The insensitivity of carrier lifetime in the InAs quantum dots to temperature, as shown in Figure 5.4, indicates that the transfer process to the ErAs MNPs is not phonon dependent. Thus using temperature-dependent TRPL we can eliminate thermally-activated transfer mechanisms as possible escape pathways and focus on processes that are independent of temperature, such as tunneling and FRET.

FRET, or Forster Resonance Energy Transfer, as discussed in Chapter 2, is a non-radiative energy transfer process that relies on the spectral overlap between two dipoles. In this case, we believe FRET to be unlikely due to the low absorption of ErAs in the emission range of the InAs quantum dots. We calculated the overlap integral,

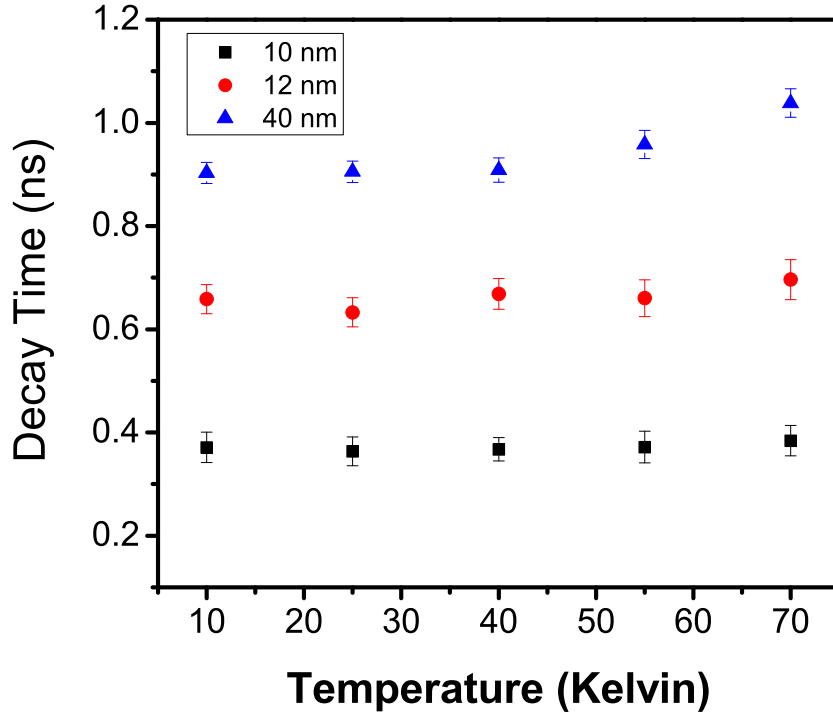


**Figure 5.4:** Temperature dependence of photoluminescence lifetime of samples with GaAs spacer layers of 40 nm, 12 nm, 10 nm [12].

$J = \int f_D(\lambda) \epsilon_A(\lambda) \lambda^4 d\lambda$ , using data from literature on the absorption of ErAs MNPs and the PL emission of our InAs QDs. The result was  $J = 1.445 \times 10^{11}$ . The calculation of the overlap integral substituted into the equation for  $R_0$  given in Chapter 2 yields a FRET distance of 5.73 nm. The quantum yield  $Q$  was assumed to be 0.5, the refractive index of GaAs was 3.299 [27], and the dipole orientation was taken to be 2/3. The greatest possible FRET distance should occur for emitters with 100 % quantum yield, therefore the calculation was repeated with  $Q = 1$ . The result was an  $R_0$  of 6.44 nm. The results are plotted with the tunneling model and the data in Figure 5.6. FRET is unlikely to be the dominant energy transfer mechanism in this case, mostly due to the lack of spectral overlap between the donor emission and acceptor absorption. Varying the estimated efficiency does not change the overall conclusion that FRET occurs at shorter distances than the energy transfer observed in these materials.

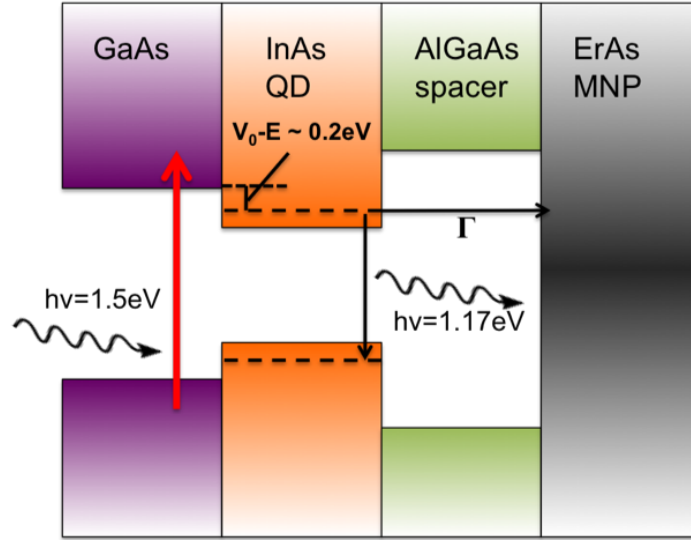


**Figure 5.5:** Schematic band diagram of one period of InAs quantum dots and ErAs nanocomposite including an AlGaAs spacer layer instead of GaAs to rule out FRET as an energy transfer mechanism.

Including AlGaAs in the spacer layer, as seen in Figure 5.5, is one suggested method for future work to firmly exclude energy transfer via FRET. Inclusion of the AlGaAs would change the tunnel probability but leave the FRET unchanged because FRET depends heavily on the distance  $d$  and only weakly on the composition of the barrier through the dielectric constant. If the resulting lifetime increased for a given barrier,  $d$ , in the AlGaAs barrier sample, compared to the GaAs barrier sample, we could conclusively eliminate FRET as a possible mechanism of energy transfer. This is a fruitful direction for future work.

The evidence points to tunneling as the escape pathway from InAs QDs to ErAs MNPs. However, to build an accurate model of tunneling behavior we have to make an assumption about the density of states in the ErAs MNPs. The electronic structure of the ErAs MNPs was probed through intensity dependent measurement of the InAs QD lifetime. Intensity-dependent TRPL was performed at fluences from  $6.8 \text{ mJ/cm}^2$  to  $141 \text{ mJ/cm}^2$ , as seen in Figure 5.7. If the ErAs MNP's had a band gap and discrete states, we would expect to see a saturation of the lifetime at high fluences that originates

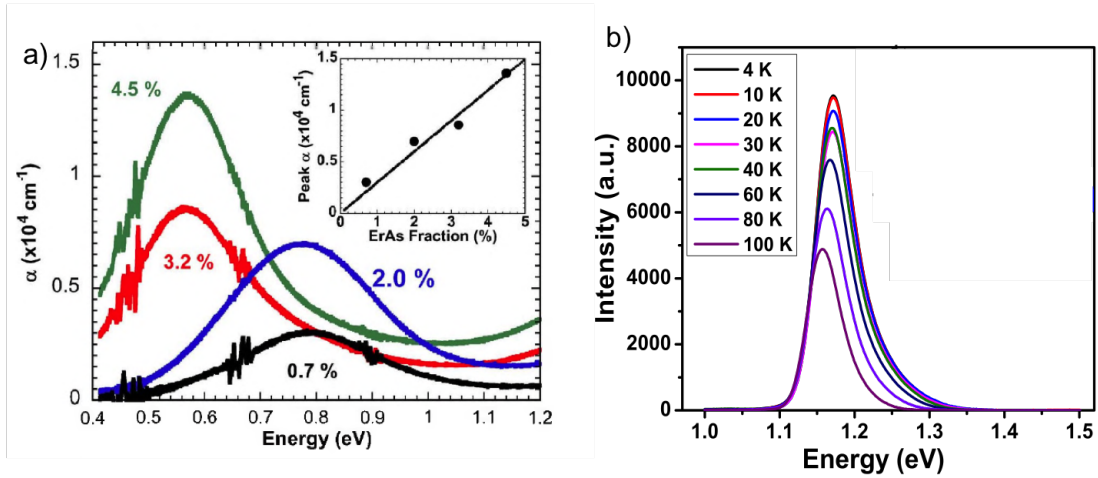


**Figure 5.6:** Comparison of donor emission and acceptor absorption spectra. a) Absorption spectra for ErAs nanoparticles embedded in GaAs with varying volume fractions of ErAs [13]. b) InAs quantum dot PL emission spectra.

in a phonon bottleneck due to filled ErAs states. This is not the case, as the data in Figure 5.7 shows: the lifetime of the InAs QDs is independent of excitation fluence. We can conclude from this that ErAs MNPs provide a non-saturatable non-radiative recombination pathway and have a continuous density of states.

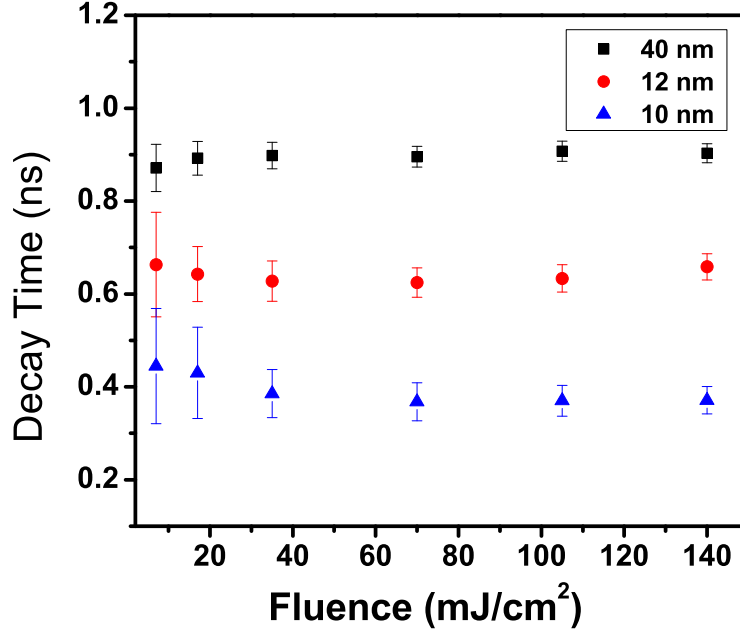


**Figure 5.7:** Fluence dependence of the PL lifetime in InAs QDs with varying distances from the ErAs nanocomposite region [12].

We next calculated the effect of tunneling on the lifetime of the InAs QDs using a standard conception of tunneling discussed in Chapter 2. We call the tunneling rate  $\Gamma$  and, using T-matrices, relate the distance between the InAs QDs and the ErAs MNPs to the lifetime [21].

From T-matrix formalism we have:

$$\Gamma = \frac{1}{\tau} = \frac{\hbar\pi T}{2d^2m^*} \quad (5.1)$$

where

$$T = \left[ 1 + \frac{V_0^2}{4E(V_0 - E)} \sinh^2(\kappa_2 d) \right]^{-1} \quad (5.2)$$

and

$$\kappa_2 = [2m^*(V_0 - E)/\hbar^2]^{1/2} \quad (5.3)$$

where  $\kappa_2 = [2m(V_0 - E)/\hbar^2]^{1/2}$ ,  $m^*$  the effective mass of the electron,  $E$  the energy of the discrete QD state and  $V_0$  the depth of the potential well, estimated via Anderson's rule [21]. Figure 5.8 shows the distance dependence of the lifetime and plots the result of the tunneling model. We find the best fit to the data using  $V_0 - E = 0.15$  eV, consistent with our estimate, based on the energy of the InAs ground state PL, that  $V_0 - E \sim 0.2$  eV. The dotted and dashed lines display fits using  $V_0 - E$  values of 0.1 and 0.2 eV, respectively, for comparison. The exact values of  $E$  and  $V_0$  cannot be precisely measured, but reasonable variations in the absolute values of  $E$  and  $V_0$  do not alter the fits to the data when  $V_0 - E$  remains constant. The measured PL decay rates agree with the tunneling model predictions within the uncertainty of the measurement and our understanding of the exact energy levels of the InAs quantum dots.

Figure 5.9 shows the distance dependence of PL lifetime including the model of FRET described previously. The red and blue curves shows the variation in  $R_0$  that occurs with variation in quantum yield of the emitters. The red curve,  $R_0 = 6.44$  nm, shows the lifetime computed with a FRET model including 100% quantum yield. The results confirm that FRET is unlikely to be the dominant energy transfer mechanism in these samples. The excellent agreement between the measured data and the theoretical tunneling model suggest that tunneling is the dominant mechanism of carrier transfer between the InAs QDs and ErAs MNPs.

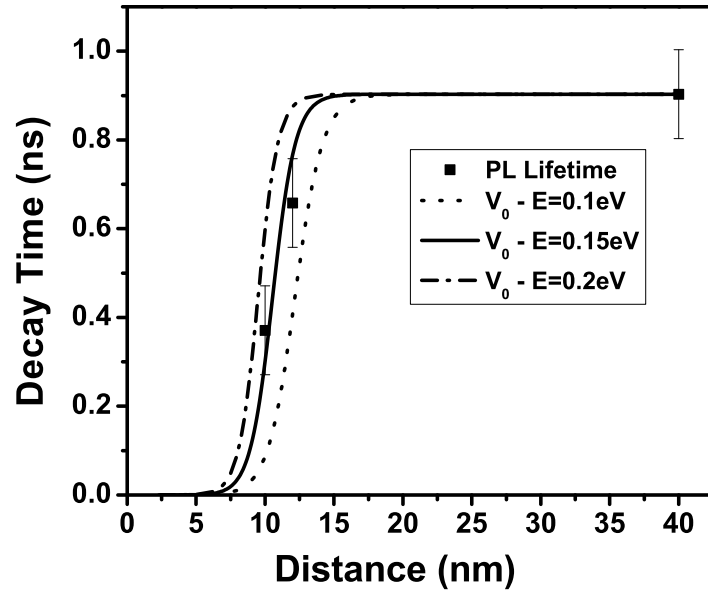


Figure 5.8: Dependence of PL lifetime on the thickness of the GaAs spacer layer with tunneling model [12].

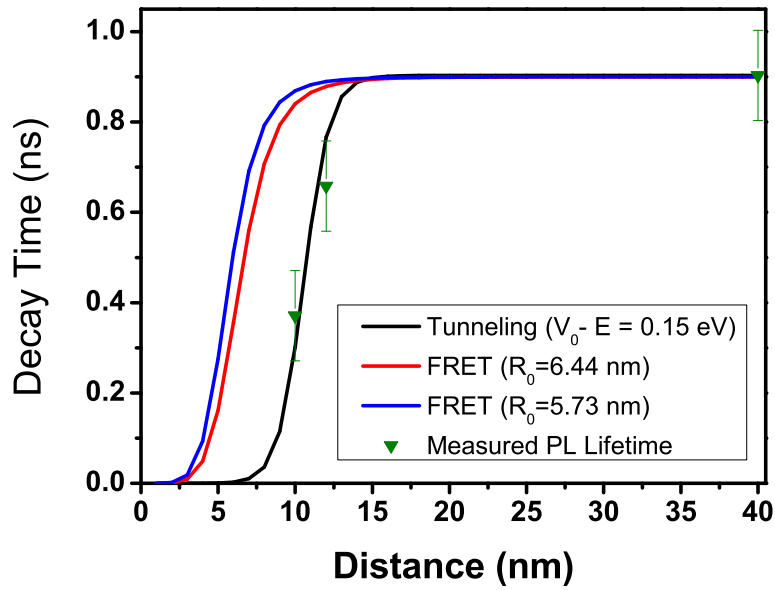


Figure 5.9: Dependence of PL lifetime on the thickness of the GaAs spacer layer with tunneling model and FRET model.

In summary, we use steady-state and time-resolved PL to probe the electronic structure of ErAs MNPs and the mechanisms of carrier transfer from InAs QDs to ErAs MNPs. Steady-state PL shows a decrease in PL intensity with increasing temperature and with decreasing distance between InAs quantum dots and ErAs MNPs. The absence of a temperature dependence for the PL decay rate allows us to conclude that carrier transfer is not dominated by phonon-assisted processes. The absence of an excitation fluence-dependence allows us to confirm that the ErAs MNPs have a continuous density of states. The excellent agreement between a simple model of carrier tunneling and the observed dependence of the PL decay rate on the distance between InAs quantum dots and ErAs MNPs allows us to conclude that tunneling through the GaAs barrier is likely the dominant mechanism of carrier escape from the InAs QDs. The excellent agreement between the model and experimental data suggests that the rate of carrier escape from QDs can be easily tailored for future optoelectronic device applications by selecting the appropriate GaAs barrier thickness or barrier composition.

## Chapter 6

### ENERGY TRANSPORT AND RECOMBINATION IN COLLOIDAL QUANTUM DOT STRUCTURES

We have shown that TRPL can be used to understand carrier transport and loss in controlled bulk and nanoscale semiconductor heterostructures. These same principles can be used to understand energy transport and loss in complex colloidal quantum dot heterostructures. Colloidal quantum dots (CQD) have numerous applications in photovoltaic and light emitting devices. However, unlike the material systems previously discussed, CQD materials have additional complexities that influence carrier transport and recombination. For example, surface ligands influence both surface recombination, the distance between quantum dots and the transport pathways between the dots [37], [63]. Consequently, changing the ligand type can influence three or more physical processes that are important to device performance. TRPL and PL allow us to isolate energy transfer and nonradiative recombination pathways in CQD heterostructures, which allows us to understand and engineer energy transport with nanoscale structure.

#### 6.1 Colloidal QD Cascade Structures

Controlling the structure of CQD thin films allows us to characterize recombination and carrier transport mechanisms using TRPL. Cascade structures, in which large, small optical band gap, acceptor quantum dots are sandwiched between layers of small, wide optical band gap, donor quantum dots, can influence energy and charge transport. A cartoon of a CQD cascade structure can be seen in Figure 6.1. Previous work by Feldmann et. al. [64] has shown that cascaded band gap CQD structures funnel energy through FRET from small to large CdSe QDs. Our work reveals an enhancement of

photoluminescence from the acceptor layer unexplained by FRET transfer alone and we use TRPL to understand how the cascade structure leads to an understanding of additional transport pathways such as trap state recycling.

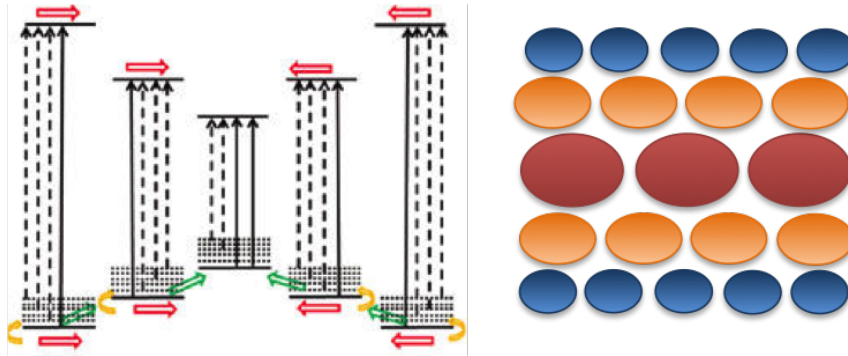


**Figure 6.1:** Cartoon of the colloidal quantum dot cascade structure [14].

### 6.1.1 Cascade Structure Fabrication

A CQD cascade structure was formed using a ligand exchange process. Three different sizes of lead sulfide (PbS) colloidal quantum dots were synthesized using a procedure modified from Hines et. al. [31]. Lead oxide (10 g) and oleic acid (1.34 g) were added to a flask which was heated and stirred under vacuum to degas. The mixture was kept under nitrogen at 110°C for 30 min. Next a solution of 210  $\mu\text{L}$  of hexamethyldisilathiane in 4 mL of octadecene was quickly injected into the flask, which was immediately removed from heat and allowed to slowly cool to room temperature. The CQDs were washed by precipitation in acetone and centrifugation several times. The size of the nano crystals in this synthesis procedure was controlled through the amount of oleic acid, whereby higher OA concentration gives larger CQDs [14]. The sizes of the QDs were chosen to allow emission wavelengths of 980, 1055 and 1240 nm.

The native ligand after synthesis is C18 oleic acid. Although oleic acid is known to do a good job of passivating surface states, it is a long chain acid that leads to

relatively large separations between CQDs, on the order of 2.2 nm. To facilitate energy transport between CQDs for device applications, we explored the consequences of exchanging the oleic acid for shorter ligands ethane dithiol (EDT) and benzene dithiol (BDT). For the ligand exchange, clean glass slides were dipped into a dilute solution of CQDs ( $<5$  mg/mL) by dip-coater and removed at 200 mm/min. Once dry, the substrate was dipped into a 0.02 M solution of EDT or BDT and acetonitrile for five seconds to remove OA ligands. Once the film is dry, the procedure can be repeated to add another layer of QDs. The shorter ligands increase the conductivity of the film by replacing long insulating ligands and also make the CQD film insoluble by cross linking the CQDs together.

### 6.1.2 Energy Transport Mechanisms & Characterization

The cascade structures studied were fabricated to enable a systematic consideration of energy transfer. We first use steady-state photoluminescence and absorption measurement to characterize the emission and absorption of the three sizes of PbS CQDs, monolayers of OA capped PbS QDs and films treated with EDT and BDT. The steady state PL, as seen in part a) of Figure 6.2, shows that the ligand exchange causes a red shift in the ground state emission of the QDs. The BDT-treated CQDs shows a  $\sim 35$  nm redshift while the EDT-treated film shows a  $\sim 71$  nm redshift. Redshifts occur due to energy transfer from high-energy QDs to low-energy QDs within the ensemble, followed by radiative recombination within the low-energy QD. The observed redshift suggests that energy transfer within the monolayers is becoming more efficient after the ligand exchange. FRET is increasingly efficient at shorter distances, and as the distance between QDs decreases, it becomes more efficient for energy to transfer to the lower energy QD states within the inhomogeneous size distribution of the CQDs.

Figure 6.2 shows that PL intensity from the BDT-treated sample was slightly enhanced relative to both the untreated sample and the EDT-treated sample. This can be explained by a higher concentration of p-type surface states in the OA film compared to the BDT-treated film and shorter interparticle spacing in EDT-treated

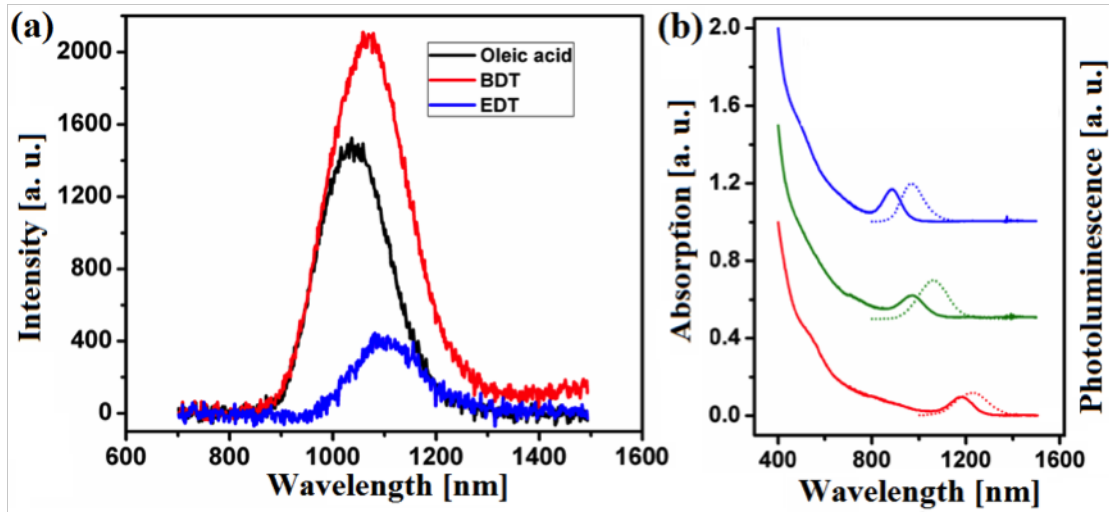


**Figure 6.2:** a) Steady-state photoluminescence of the OA, EDT and BDT-treated QD monolayers. b) Three sizes of PbS CQDs with 980 nm (blue) absorption solid line, emission dotted line, 1055 nm (green), 1240 nm (red) [14].

CQDs compared to the BDT-treated film. The BDT passivates the surface more effectively and the larger interparticle distance reduces both transport across the film and non-radiative recombination. Previous work suggests that PL quenching occurs when CQDs are formed into a film due to fast exciton dissociation from tunneling to non-radiative surface states. Conductivity measurements using charge extraction in linearly increasing voltage (CELIV) measurements confirm that EDT-treated CQD films have a 40-fold higher conductivity,  $1.56 \times 10^{-11}$  S/m, compared to the BDT-treated film,  $3.91 \times 10^{-13}$  S/m. The CELIV measurement directly confirms a higher acceptor concentration in the EDT-treated films as compared to the BDT films. These results demonstrate BDT provides improved surface passivation compared to OA and EDT-treated films, resulting in reduced surface-state mediated non-radiative recombination and increased acceptor concentration leading to increased PL intensity.

The cascade structures were built up layer by layer and measured at each stage to assess the carrier dynamics. Colloidal quantum dot sizes were chosen to achieve spectral overlap between the absorption of the acceptor CQDs and the emission of the donor quantum dots - a requirement for efficient FRET. Figure 6.2 b) shows the

absorption and emission spectra of the three sizes of CQDs.

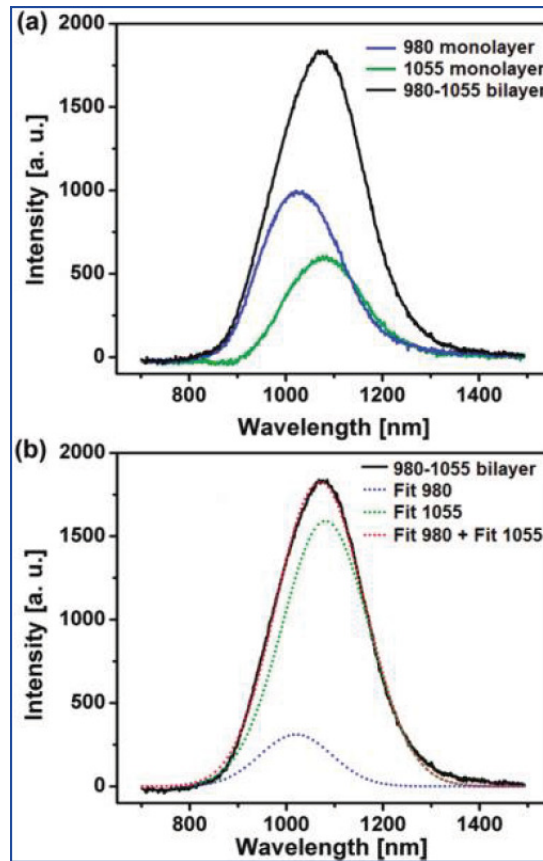


**Figure 6.3:** a) Steady-state PL measurement of 980nm and 1055nm CQD films using BDT ligand exchange. Monolayers (blue and green) and bilayer (black). b) Gaussian fit to the bi-layer PL spectrum showing a quenching of the 980 nm and an enhancement of the 1055 nm emission [14].

Consider first the energy transfer that occurs in a bilayer structure formed with the ligand exchange process. Figure 6.3 shows the steady state PL from a monolayer of 980 nm (blue) and 1055 nm (green) quantum dots treated with BDT. The black line shows the change in PL when the two films are placed into a bilayer 980 nm-1055 nm structure. As seen from the gaussian fitting results in Figure 6.3 b), enhanced emission from the 1055nm CQDs relative to the 980 nm CQDs is demonstrated. The density of 1055 nm QDs is the same in both the mono- and bi-layer structures, so the 165% increase in emission must be from either a reduction in non-radiative recombination in

the 1055 nm QDs or energy transfer from the 980 nm QDs to the 1055nm QD. Inclusion of the 980 nm QDs is unlikely to provide a pathway for a decrease in trap states or non-radiative recombination centers, but it does provide a pathway for FRET. Non-radiative recombination could also be reduced, not by the inclusion of non-radiative or defect centers, but by the depopulation of existing trap centers by trap state recycling. Trap state recycling is a process in which trapped charges on the surfaces of the CQDs transfer by FRET to the core of a lower energy acceptor quantum dot [64].

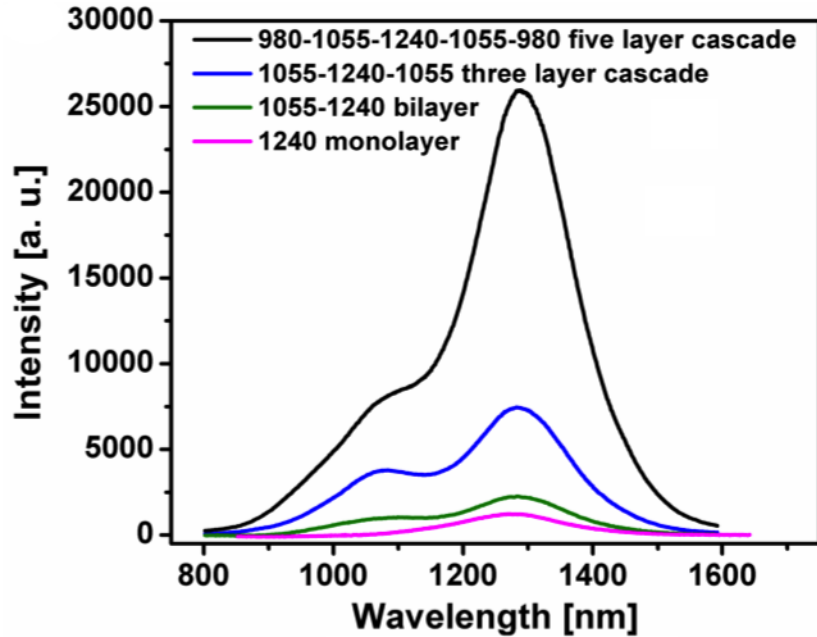


**Figure 6.4:** PL spectrum of the 1240 nm monolayer (pink), 1240 nm-1055 nm bilayer (green), 1055 nm-1240 nm-1055 nm cascade structure (blue), and 980 nm-1055 nm-1240 nm-1055 nm-980 nm cascade structure (black) [14].

Figure 6.4 shows the steady-state PL measurements of a five layer cascade structure as it is built up from a single monolayer. The acceptor size QDs (1240 nm emission) are shown in pink as the emission from a single monolayer. When the 1240 nm QDs are deposited onto the 1055nm donor QD monolayer forming a bilayer, we see enhanced emission as in the 980-1055 nm bilayer system - evidence of FRET. Forming a 1055 nm-1240 nm-1055 nm cascade shows a 5-fold emission increase compared to the

single monolayer. Finally, the five layer cascade of 980 nm-1055 nm-1240 nm-1055 nm-980 nm QDs shows a 19-fold enhancement of emission from the 1240 nm QDs relative to the monolayer, suggesting efficient FRET. An enhancement of PL emission could also be due to a decrease in non-radiative recombination due to trap state recycling.

To isolate the role of trap state recycling in the cascade structures additional control structures were formed. Five monolayers of 1240 nm CQDs treated with BDT and EDT were assembled. Figure 6.5 shows the absorption spectra as each layer of 1240 nm was added. The absorption shows a linear increase in absorption with additional monolayers, however the PL emission seen in Figure 6.6 shows significantly more than 5-fold increase in PL, suggesting a decrease in non-radiative recombination occurs. Trap state recycling occurs when surface-bound excitons transfer via FRET to nearby QDs where they can recombine radiatively. The red shift observed in the emission of the 5-layer structures, compared to the monolayer, supports this conclusion.

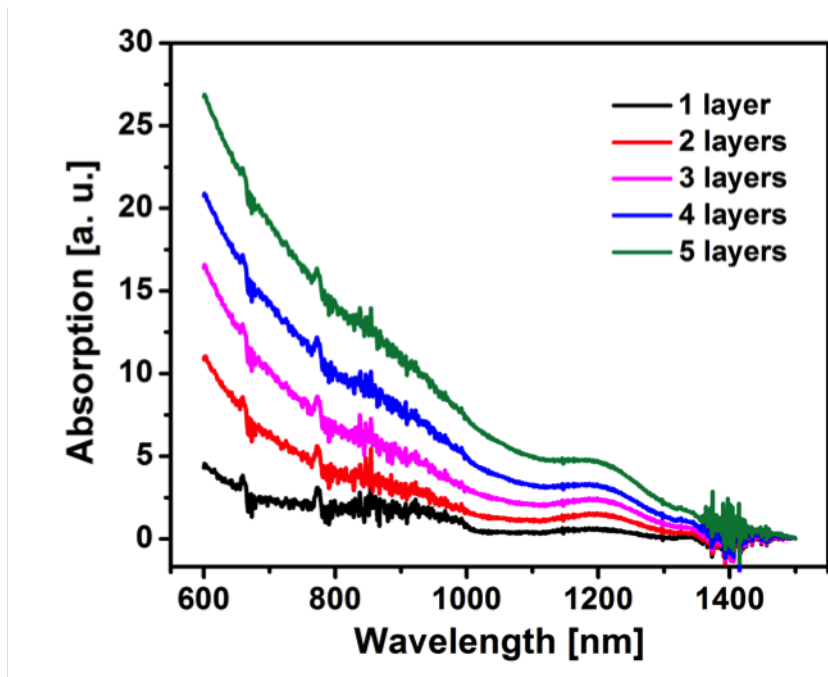


**Figure 6.5:** Absorption spectra of monolayer-by-monolayer assembly of PbS CQD solid treated with BDT [14].

The inset to Figure 6.6 shows the absorption of the 5-layer cascade structure

(red) and the the 5-layer acceptor structure (black). The integrated absorption of the 5-layer 1240 nm acceptor structure is 44% greater than the 5-layer cascade structure. However the integrated emission shows the 5-layer acceptor structure is 5% *less* than the 5-layer 1240 nm cascade structure. The overall PL enhancement in the cascade structure relative to the acceptor structure, especially given the lower absorption seen in the cascade structure, is further evidence of efficient exciton recycling from surface state bound excitons to acceptor quantum dot ground states.

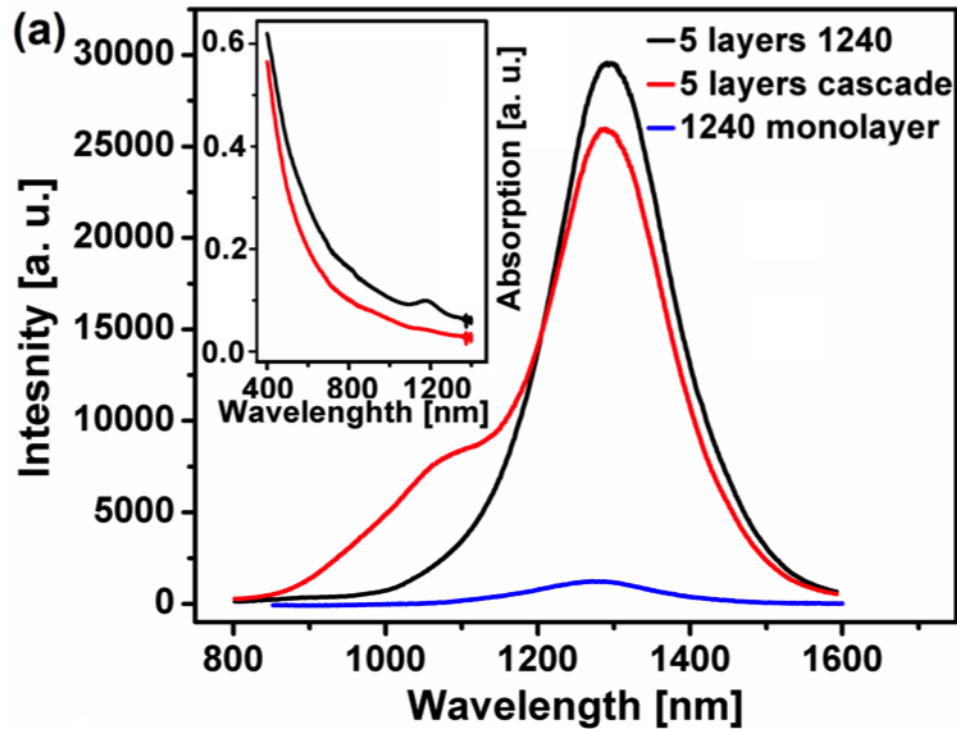


**Figure 6.6:** Photoluminescence of the five layer BDT-treated cascade structure (red), five layers of BDT-treated 1240 nm emission acceptor CQDs (black) and a single monolayer of 1240 nm acceptors. Inset: The absorption spectra of the 5-layer 1240 nm acceptor CQDs (black) and the 5-layer cascade [14].

Comparing Figure 6.6 and Figure 6.7, we can see the role played by the surface ligand in influencing trap state recycling. In the BDT-treated films, the acceptor structures and the cascade structures have similar emission. BDT has been shown to passivate the surface better than EDT, therefore surface traps play a smaller role

in energy transfer in the BDT films. In the EDT films the cascade structure has significantly higher emission compared to the 5-layer acceptor film. However due to the additional trap states causing non-radiative emission, the overall PL intensity is much lower for the EDT-treated films than the BDT-treated films. This suggests trap state recycling dominates in EDT-treated CQD films compared to BDT CQD films.

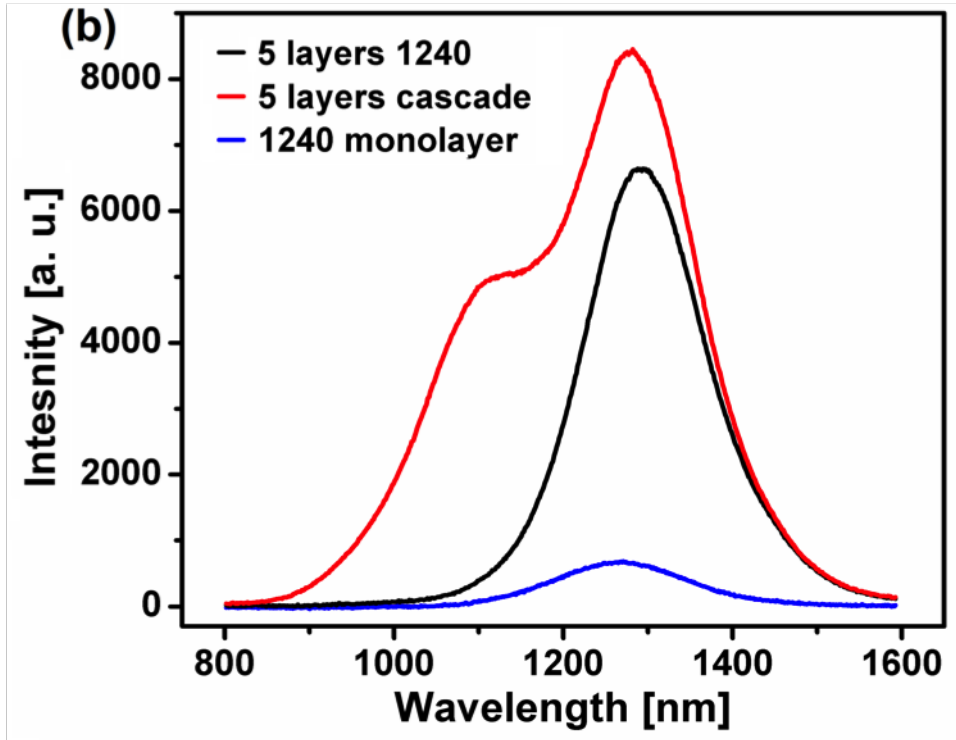


**Figure 6.7:** Photoluminescence of the five layer EDT-treated cascade structure (red), five layers of EDT-treated 1240 nm emission acceptor CQDs (black) and a single monolayer of 1240 nm acceptors [14].

Time-resolved photoluminescence was used to verify that the enhancement seen in the steady state PL is not completely accounted for by FRET from ground state to ground state of the CQDs in the cascade structure. Figure 6.10 shows the decay curves of donor emission in donor-only and donor-acceptor bilayer films treated with both BDT and EDT. The untreated OA-capped donor film was found to have a lifetime of  $\tau_d=278$  ns. As summarized in Table 6.1, the lifetime of the donor-only BDT-treated

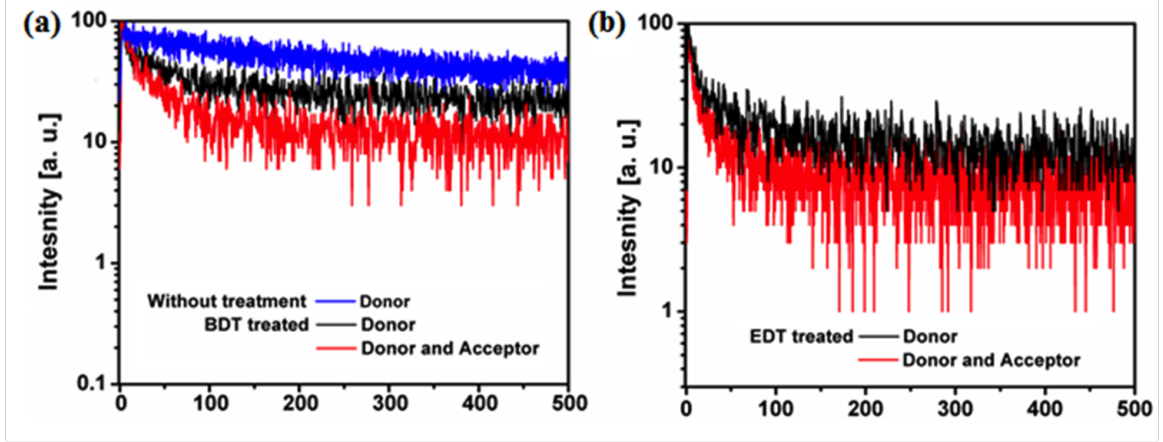


**Figure 6.8:** Time-resolved photoluminescence of PbS CQD films measured at the donor peak of 980 nm. a) OA capped untreated PbS CQD film (blue), donor-only BDT-treated PbS film (black), and BDT-treated donor-acceptor bilayer (red). b) Donor-only EDT-treated PbS film (black), and EDT-treated donor-acceptor bilayer (red) [14].

Sample	$\tau_d$ (ns)	$\tau_{da}$ (ns)
PbS w/ BDT	77	40
PbS w/ EDT	57	27

**Table 6.1:** Lifetimes of donor-only and donor-acceptor film structures.

film was found through mono-exponential fitting to be  $\tau_d=77$  ns, while the lifetime of the donor-acceptor BDT film was found to be  $\tau_{da}=40$  ns. With a shorter interparticle spacing, the EDT-treated films show a donor-only lifetime of  $\tau_d=57$  ns and a donor-acceptor bilayer lifetime of  $\tau_{da}=27$  ns. FRET efficiency can be estimated using  $\eta = 1 - (\tau_{da}/\tau_d)$  and is 53% for the EDT-treated bilayer and 48% for the BDT treated bilayer [65]. Assuming an approximate FRET efficiency of 50%, we can calculate the expected PL enhancement in the acceptor CQDs of the cascade structure to be at most 150% or 3-fold. If trap state recycling were effecting the energy transfer in these films, we would not see a change in lifetime of the donor CQDs because trapped excitons would recombine non-radiatively in the absence of trap state recycling. The lifetime of the acceptor, however would be influenced by both FRET and trap state recycling.

Therefore, looking at the donor lifetime as a signature of FRET gives us the expected FRET efficiency whether or not trap state recycling plays a role in energy transfer. FRET alone could account for a maximum 3-fold enhancement in PL. The observation of 19-fold PL enhancement for BDT treated films and 13-fold enhancement for EDT-treated films is clear evidence that trap state recycling plays an important role in energy transfer in these systems.

## 6.2 Type I & II Structures

Using this new understanding of carrier dynamics in colloidal quantum dot heterostructures, we can design structures that control energy and carrier transfer in a way that would be useful for optoelectronic devices such as photovoltaic cells. Colloidal quantum dot PV devices have been of limited use due to low carrier mobility and high trap density leading to large non-radiative losses [66], [67]. Designing a heterostructure to take advantage of energy transfer pathways could allow us to design more efficient CQD PV devices. Heterostructures with type II band alignment represent one approach to separating excitons in CQDs structures for CQD PV. Type-II refers to the condition in which the allowed states in the conduction and valance band of one CQD material are below the respective allowed states in the other CQD material, as depicted in Figure 2.8. Several groups have demonstrated the ability to separate excitons using type-II heterostructures [68], [69]. We investigate the effect of type-II band alignment on heterostructures fabricated with PbS and PbSe CQDs using the BDT ligand exchange treatment described previously.

### 6.2.1 Structure Formation

Type II CQD structures have previously been demonstrated in CdSe and CdTe systems [70]. Working with our collaborators, we extended the previous work to look at carrier separation in PbS/PbSe quantum dots, a system not previously investigated using type-II structures and advantageous in terms of a useful band gap for PV applications. CQDs were synthesized by a modified Hines method as previously described.

For the type I structures, PbS and PbSe QDs were made with emission peaks of PbSe at 930nm and PbS at 1040nm. This forms the typically FRET donor-acceptor structure. For the type II structure, PbSe and PbS QDs were synthesized with emission peaks centered around 960nm.

### 6.2.2 Energy Transport Mechanisms & Characterization

Figure 6.9 shows the evolution of the PL during the assembly of the type-1 structure. As we saw previously in the cascade structures, the acceptor QD emission is enhanced due to energy transfer from the donor QDs and it is further enhanced as a second layer of donors is added to sandwich the acceptor layer. Figure 6.9 demonstrates that the full-width-half-max of the type-1 structure and the emission energy of the peak match the PbS monolayer PL FWHM and peak position. The emission from the two layers of donor PbSe, however, remains negligible.

Additionally, the integrated emission intensity is more than twice what the sum of two donor PbSe films and an acceptor PbS film in isolation would be. The increase in emission efficiency is evidence that the strongly-coupled type-1 structure allows trap state recycling similar to that demonstrated in the cascade structure above. To analyze the recombination processes in the type-1 structure, we performed TRPL on both a BDT-treated acceptor-only control film and the three layer type-1 structure.

Well-passivated lead chalcogenide quantum dots have relatively long radiative lifetimes, on the order of hundreds of nanoseconds to microseconds. Our decay times for the BDT and three-layer structure show lifetimes on the order of ten nanoseconds, suggesting non-radiative mechanisms are limiting the lifetime. Figure 6.10 shows that the fabrication of a layered structure with BDT ligand exchange treatment does not significantly alter the lifetime and therefore does not introduce additional non-radiative pathways beyond the monolayer treated with BDT. Given that the formation of the type-I and type II structures are performed using the same ligand exchange treatment, looking at the TRPL from the type-II structure in comparison to the type-I lifetimes

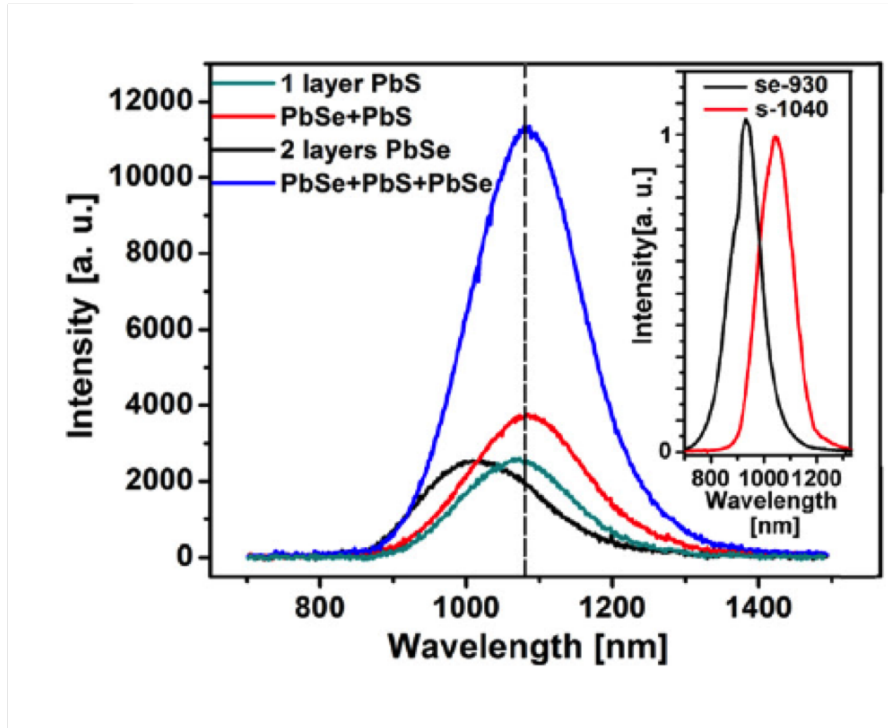


**Figure 6.9:** Photoluminescence emission from the three layer type-I CQD structure (blue), two layers of PbSe (black), PbSe-PbS bilayer (red) and a mono-layer of PbS CQDs [1].

allows us to understand how the band offsets influence carrier transport in the two architectures.

Figure 6.11 shows the PL emission of the type-II PbS/PbSe structure. The change in the sizes of the quantum dots relative to the type-I structures change the alignment of allowed states and makes FRET highly unlikely in this structure. To make a fair comparison between the 4-layer control structures and the two-layer type-II structure, the dotted black line shows the sum of the control structures divided by two. The emission peak of the type-II structure is in line with the arithmetic mean of the control structures, which implies that both PbS and PbSe contribute to PL emission in the type-II structure. However, the emission intensity is significantly quenched. From the TRPL on the type-I structures we know that formation of the layered structure does not introduce any additional non-radiative recombination pathways, so the quenching

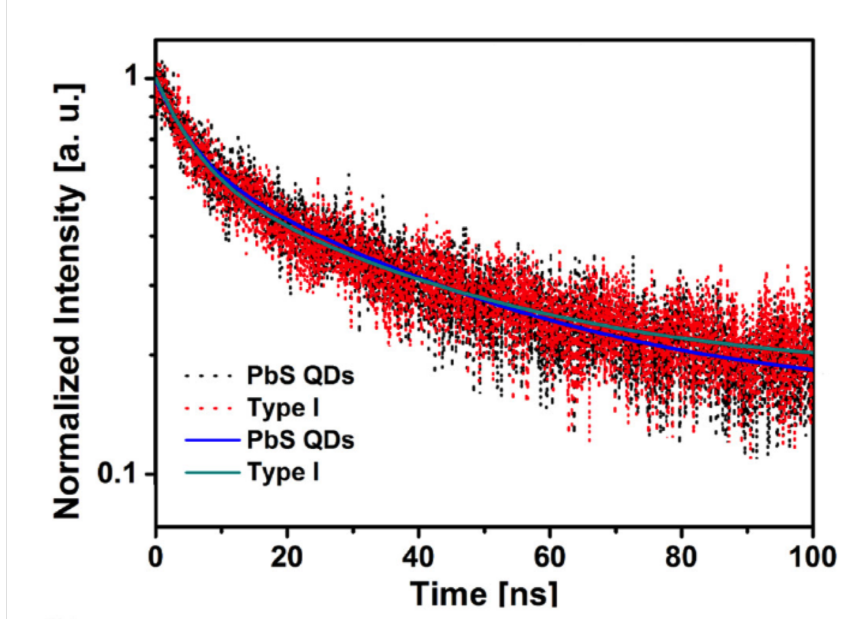


**Figure 6.10:** Time-resolved photoluminescence taken at 950nm of PbS BDT-treated film (black with blue fit line) and a BDT treated type-I structure (red with green fit line) [1].

Sample	$\tau_1$ (ns)	$\tau_2$ (ns)
PbS w/ BDT	$4.8 \pm 0.4$	$35 \pm 2$
Type I	$5.3 \pm 0.4$	$34 \pm 2$
Type II	$3.9 \pm 0.2$	$23 \pm 1$

**Table 6.2:** Lifetimes of lead chalcogenide quantum dot structures [1].

must be due to a non-radiative pathway that is related to the alignment of allowed states of the QDs.

As we have done previously, we used TRPL to identify the underlying mechanism leading to the PL quenching observed in the type-II structure. The results of the bi-exponential fitting can be seen in Table 6.2. The lifetimes of the BDT and type-I film are longer than the lifetimes of the type-II film, indicating that charge separation is causing the reduced PL emission and reduced lifetime.

In summary, we have demonstrated the use of TRPL to understand the energy

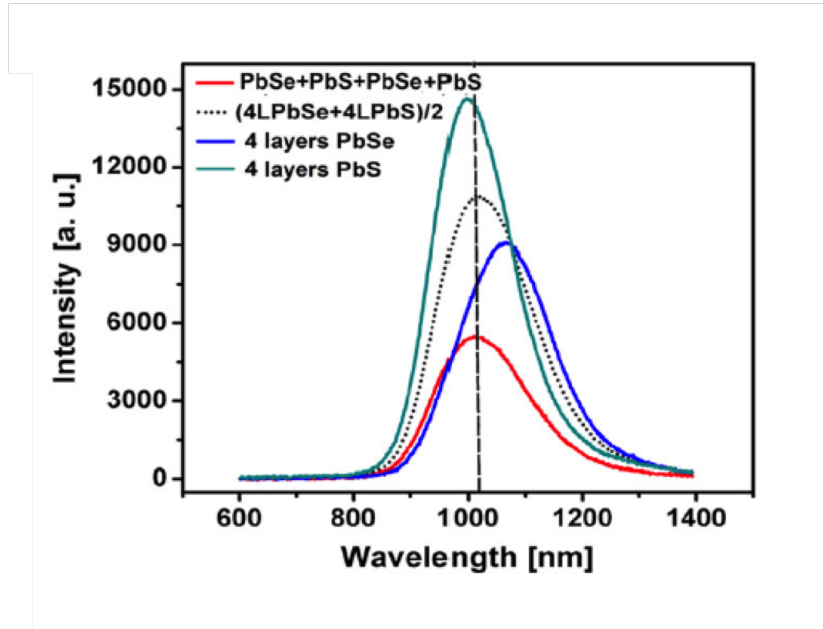


**Figure 6.11:** PL from a four layer PbSe film (blue), a four layer PbS film (green), and a type-II PbS-PbSe-PbS-PbSe four layer heterostructure. The arithmetic average between the PbS (green) and PbSe (blue) four layer films is shown for comparison with the heterostructure [1].

transfer and carrier transfer mechanisms in colloidal quantum dot heterostructures. We used 5-layer FRET structures to separate the role of ground state FRET and trap state recycling by comparing the PL to TRPL and the calculated FRET efficiency for a given lifetime. We built type-I and type-II band alignment structures to understand how charge separation and energy separation compare in similar structures with different band alignment. By extending our analysis beyond a single measure of PL lifetime, we have been able to develop a more detailed understanding of energy transfer in colloidal quantum dot heterostructures.

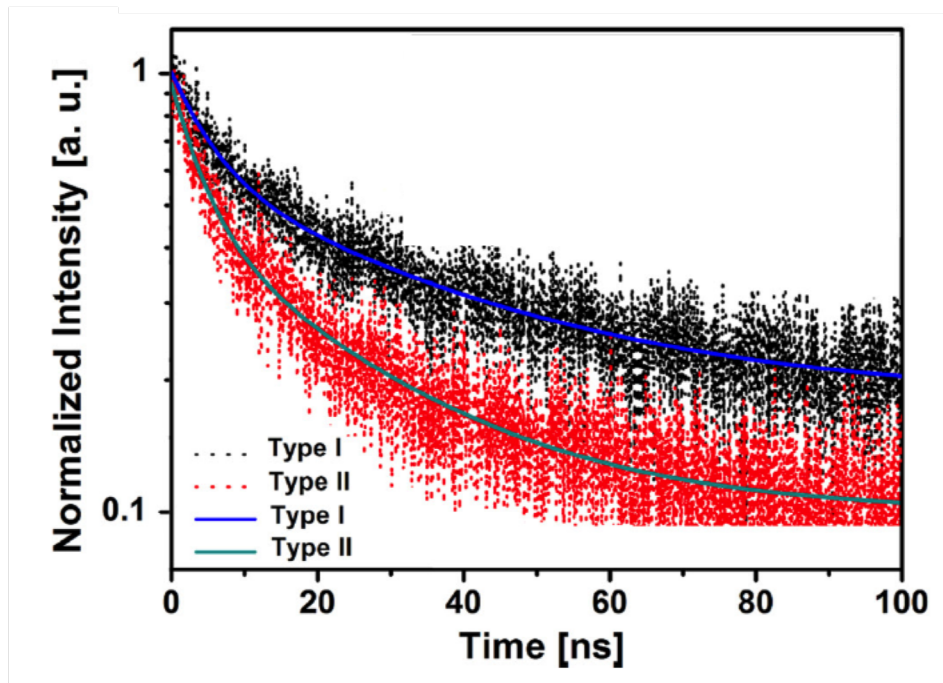


**Figure 6.12:** Time-resolved photoluminescence decays of BDT treated type-I and type-II heterostructures showing the reduced PL lifetime in the type-II structure [1].

## Chapter 7

### CONCLUSIONS

In this work, we used continuous wave and time-resolved photoluminescence to understand energy transfer mechanisms in materials for optoelectronic device applications. We focus particularly on the use of nanometer-scale control over material structure and composition to isolate and separately understand distinct mechanisms for carrier or energy transfer and loss. We first used GaAs double heterostructure architectures and the intensity dependence of PL lifetime to understand the trap saturation process and estimate trap density in GaAs samples grown at varying rates for photovoltaic applications. We used the PL lifetime of InAs QDs as a function of laser intensity and temperature to probe the electronic structure of a GaAs-based nanocomposite containing InAs QDs at varying distances from embedded ErAs metal nanoparticles with possible applications in THz devices. We also used FRET cascade structures to understand the role of trap state recycling in colloidal quantum dot heterostructures applicable to colloidal quantum dot photovoltaic devices. We showed that a detailed understanding of TRPL, in which measurement conditions are varied to attain information beyond the standard minority carrier lifetime, can provide insights into carrier recombination and energy transport. These insights will inform the design of next generation optoelectronic devices.

The methods we describe here can be extended to achieve a more complete understanding of the material systems investigated. For the GaAs double heterostructures, Ahrenkiel and others have shown that a series of TRPL measurements with varying active layer thickness can be used to generate an estimate of surface recombination velocity and photon recycling. Our work relied on the assumption that the

InGaP window layer provides adequate surface passivation to reduce the surface recombination to negligible levels. Photon recycling, meanwhile, is dependent on both doping and the active region thickness. Our work shows that it would likely produce much longer lifetimes, thus our short lifetimes are SRH limited. While these two assumptions are sound, an experimental investigation of samples with a series of different thicknesses would provide evidence to strengthen our conclusions.

There is an additional opportunity to extend this work by considering a wider range of pump fluences in our intensity-dependent TRPL experiments. The measurements conducted thus far used intensities that varied by only one order of magnitude, limited by the pump power available from our laser and the detection threshold of our avalanche photodiode system. Debuf et. al. and others have theoretically calculated saturation behaviors that include a flat, low-injection regime, a regime of quasi-linearly increasing lifetime, and a saturated, flat high-injection region. An improvement on this work would increase the range of fluences to fit the full curve. Measuring more samples and comparing results to SIMS would also advance our understanding of the material quality. To fit our data with a computational model based on the work of Debuf et. al., we made the assumption of a single defect level, EL2, which we believe dominates the trapping process. Measuring the actual defect levels with DLTS would allow us to determine whether this assumption is true or whether multiple defects play a role. Debuf et. al have extended his analytical solution to one with multiple defects so it is conceivable that multiple defects could be modeled with a process similar to what we have done here.

In Chapter 5 we discussed using the PL lifetimes of InAs quantum dots to probe charge and energy transfer to ErAs metal nanoparticles. We saw that while FRET was unlikely, due to the lack of spectral overlap between the emission of the donor and the absorption of the acceptor, FRET remains a possible mechanism of energy transfer that we can not unambiguously rule out. Additional work to address this question could be undertaken by replacing some portion of the GaAs barrier separating the QDs and the ErAs nanoinclusions with AlGaAs. The addition of AlGaAs to the barrier would

change the tunneling probability but would not change the likelihood of FRET, which is dependent only on distance and spectral overlap. Additionally, creating additional samples with varying separations, particularly in the range of 12-40 nm, would provide a better test of the tunneling theory and generate a better understanding of where tunneling begins to turn off.

For the work on colloidal quantum dot cascade structures, selecting sizes of acceptor quantum dots whose emission falls within the range of our detector would allow us to measure the increase in acceptor lifetime associated with energy transfer and strengthen our case for FRET transfer from recycled surface states.

In summary, we have used systematic TRPL measurements of semiconductor heterostructures to isolate individual carrier and energy transfer and loss processes and their dependence on nanoscale material structure and composition.

## BIBLIOGRAPHY

- [1] F. Xu, C. R. Haughn, X. Ma, M. F. Doty, and S. G. Cloutier, “Charge-transfer dynamics in multilayered PbS and PbSe quantum dot architectures,” *Applied Physics Letters*, vol. 104, no. 051112, 2014.
- [2] Mathematica, “Mathematica forums,” <http://mathematica.stackexchange.com/questions/20624/plotting-extended-zone-scheme>.
- [3] W. Shockley and W. Read, “Statistics of the Recombination of Holes and Electrons,” *Physical Review*, vol. 87, pp. 1–8, Mar. 1952.
- [4] M. Razeghi, “Quantum dot infrared photodetectors - northwestern university,” <http://cq.d.eecs.northwestern.edu/research/qdots.php>, 2008.
- [5] PlasmaChem, “Zdcdses quantum dots,” <http://www.plasmachem.com/shop/en/226-zncdses-alloyed-quantum-dots>, 2014.
- [6] A. Rogach, T. Klar, J. Lupton, A. Meijerink, and J. Feldmann, “Energy transfer with semiconductor nanocrystals,” *Journal of Materials Chemistry*, vol. 19, no. 9, pp. 1208–1221, 2009.
- [7] Wikipedia, “Heterojunction types,” <http://en.wikipedia.org/wiki/Heterojunction>, 2014.
- [8] K. Spring and M. Davidson, “Concepts in digital imaging technology - avalanche photodiodes,” *Hamamatsu*, 2014.
- [9] Hamamatsu, “Photocathode technology - photomultiplier tube,” <http://www.hamamatsu.com/jp/en/technology/innovation/photocathode/index.html>, 2014.
- [10] PicoQuant, “Fluofit software homepage,” <http://www.picoquant.com/products/category/software/fluofit-global-fluorescence-decay-data-analysis-software#images>, 2013.
- [11] C. Haughn, K. Schmieder, J. Zide, A. Barnett, C. Ebert, R. Opila, and M. Doty, “Quantification of trap state densities in GaAs heterostructures grown at varying rates using intensity-dependent time resolved photoluminescence,” *Applied Physics Letters*, vol. 102, no. 182108, 2013.

- [12] C. Haughn, E. Steenbergen, L. J. Bissell, E. Y. Chen, K. G. Eyink, J. M. O. Zide, and M. F. Doty, “Carrier transfer from InAs quantum dots to ErAs metal nanoparticles,” *Applied Physics Letters*, vol. 105, 2014.
- [13] M. A. Scarpulla, J. M. O. Zide, J. M. LeBeau, C. G. Van de Walle, A. C. Gossard, and K. T. Delaney, “Near-infrared absorption and semimetal-semiconductor transition in 2 nm ErAs nanoparticles embedded in GaAs and AlAs,” *Applied Physics Letters*, vol. 92, no. 17, p. 173116, 2008.
- [14] F. Xu, X. Ma, C. R. Haughn, J. Benavides, M. F. Doty, and S. G. Cloutier, “Efficient Exciton Funneling in Cascaded PbS Quantum Dot Superstructures,” *ACS nano*, vol. 5, no. 12, pp. 9950–9957, 2011.
- [15] D. Schroder, “Carrier lifetimes in silicon,” *IEEE Transactions on Electron Devices*, vol. 44, no. 1, pp. 160–170, 1997.
- [16] R. K. Ahrenkiel, B. Keyes, and D. Dunlavy, “Intensity-dependent minority-carrier lifetime in III-V semiconductors due to saturation of recombination centers,” *Journal of Applied Physics*, vol. 70, no. 1, pp. 225–231, 1991.
- [17] R. K. Ahrenkiel, “NREL measurement of minority carrier lifetime by time resolved photoluminescence,” *Solid-State Electronics*, vol. 35, pp. 239–250, May 2002.
- [18] R. Ahrenkiel, B. Keyes, G. Lush, M. Melloch, M. Lundstrom, and H. MacMillan, “Minority-carrier lifetime and photon recycling in nGaAs,” *Journal of Vacuum Science & Technology A: Vacuum, Surfaces, and Films*, vol. 10, no. 4, pp. 990–995, 1992.
- [19] O. Manasreh, *Semiconductor Heterojunctions and Nanostructures*. McGraw-Hill, 2005.
- [20] C. Kittel, *Introduction to Solid State Physics*. John Wiley & Sons, Inc, 8 ed., 2013.
- [21] J. H. Davies, *The Physics of Low Dimensional Semiconductors: An Introduction*. Cambridge University Press, 1998.
- [22] R. K. Ahrenkiel, “Measurement of minority-carrier lifetime by time-resolved photoluminescence,” *Solid-State Electronics*, vol. 35, no. 3, pp. 239–250, 1992.
- [23] P. Renaud, F. Raymond, B. Bensaïd, and C. Vèrié, “Influence of photon recycling on lifetime and diffusion coefficient in GaAs,” *Journal of Applied Physics*, vol. 71, no. 4, p. 1907, 1992.
- [24] R. K. Ahrenkiel, B. M. Keyes, and D. J. Dunlavy, “Intensity-dependent minority-carrier lifetime in III-V semiconductors due to saturation of recombination centers,” *Journal of Applied Physics*, vol. 70, no. 1, p. 225, 1991.

- [25] D. Debuf, Y. Shrivastava, and A. Dunn, “General analytic solution to the Shockley-Read-Hall rate equations with a single-level defect,” *Physical Review B*, vol. 65, June 2002.
- [26] D. Debuf, Y. Shrivastava, and A. Dunn, “General analytic solution to the Shockley-Read-Hall rate equations with a single-level defect,” *Physical Review B*, vol. 65, p. 245211, June 2002.
- [27] “Physical properties of semiconductors: GaAs - gallium arsenide,” *IOFFE*, p. <http://www.ioffe.ru/SVA/NSM/Semicond/GaAs/index.html>.
- [28] M. P. Marder, *Condensed Matter Physics*. John Wiley & Sons, Inc, 2000.
- [29] C. Murray, D. Norris, and M. Bawendi, “Synthesis and Characterization of Nearly Monodisperse CdE (E = S, Se, Te) Semiconductor Nanocrystallites,” *Journal of the American Chemical Society*, vol. 115, no. 19, pp. 8706–8715, 1993.
- [30] Z. A. Peng and X. Peng, “Formation of high-quality CdTe, CdSe, and CdS nanocrystals using CdO as precursor.,” *Journal of the American Chemical Society*, vol. 123, pp. 183–4, Jan. 2001.
- [31] M. Hines and G. Scholes, “Colloidal PbS Nanocrystals with Size-Tunable Near-Infrared Emission: Observation of Post-Synthesis Self-Narrowing of the Particle Size Distribution,” *Advanced Materials*, vol. 15, pp. 1844–1849, Nov. 2003.
- [32] S. Maenosono, T. Okubo, and Y. Yamaguchi, “Overview of Nanoparticle Array Formation by Wet Coating,” *Journal of Nanoparticle Research*, vol. 5, pp. 5–15, Apr. 2003.
- [33] V. Klimov, ed., *Nanocrystal Quantum Dots*. CRC Press Taylor & Francis Group, 2nd ed., 2010.
- [34] A. Rizzo, M. Mazzeo, M. Palumbo, G. Lerario, S. D’Amone, R. Cingolani, and G. Gigli, “Hybrid Light-Emitting Diodes from Microcontact-Printing Double-Transfer of Colloidal Semiconductor CdSe/ZnS Quantum Dots onto Organic Layers,” *Advanced Materials*, vol. 20, pp. 1886–1891, May 2008.
- [35] M. J. Panzer, K. E. Aidala, and V. Bulovic, “Contact printing of colloidal nanocrystal thin films for hybrid organic/quantum dot optoelectronic devices,” vol. 1, pp. 1–8, 2012.
- [36] T. Kim, K. Cho, E. Lee, S. Lee, and J. Chae, “Full-colour quantum dot displays fabricated by transfer printing,” *Nature . . .*, vol. 5, no. February, 2011.
- [37] P. Guyot-Sionnest, “Electrical transport in colloidal quantum dot films,” *The Journal of Physical Chemistry Letters*, 2012.

- [38] D. Zhitomirsky, O. Voznyy, L. Levina, S. Hoogland, K. W. Kemp, A. H. Ip, S. M. Thon, and E. H. Sargent, “Engineering colloidal quantum dot solids within and beyond the mobility-invariant regime.,” *Nature Communications*, vol. 5, p. 3803, Jan. 2014.
- [39] A. M. Smith and S. Nie, “Semiconductor Nanocrystals: Structure, Properties, and Band Gap Engineering,” *Accounts Of Chemical Research*, vol. 43, pp. 190–200, Jan. 2010.
- [40] B. Masters, “Paths to Förster’s resonance energy transfer (FRET) theory,” *The European Physical Journal H*, vol. 39, pp. 87–139, Dec. 2013.
- [41] C. Higgins, M. Lunz, A. L. Bradley, V. A. Gerard, S. Byrne, Y. K. Gun’ko, V. Lesnyak, and N. Gaponik, “Energy transfer in colloidal CdTe quantum dot nanoclusters.,” *Optics express*, vol. 18, pp. 24486–94, Nov. 2010.
- [42] M. Lunz, A. L. Bradley, V. Lesnyak, and N. Gaponik, “Influence of quantum dot concentration on Förster resonant energy transfer in monodispersed nanocrystal quantum dot monolayers,” *Physical Review B*, vol. 81, pp. 1–10, May 2010.
- [43] D. K. Schroder, *Semiconductor Material and Device Characterization*. IEEE Press, 3rd ed., 2006.
- [44] Coherent, 5100 Patrick Henry Drive, Santa Clara, CA 95054, *The Coherent Mira Model 900-F Laser Operator’s Manual*.
- [45] ConOptics, *Moduator Alignment Procedure*, 2009.
- [46] PicoQuant GmbH, Rudower Chaussee 29 (IGZ) 12489 Berlin, Germany, *PicoHarp 300 User’s Manual and Technical Data*.
- [47] J. A. D.V. O’Connor, W.R. Ware, “Deconvolution of fluorescence decay curves. a critical comparison of techniques,” *Journal Of Physical Chemistry*, vol. 83, no. 10, pp. 1333–1343, 1979.
- [48] W. Ware, L. Doemeny, and T. Nemzek, “Deconvolution of fluorescence and phosphorescence decay curves. Least-squares method,” *The Journal of Physical Chemistry*, vol. 4561, no. 8, 1973.
- [49] R. K. Ahrenkiel and M. Lundstrom, eds., *Minority Carriers In III-V Semiconductors: Physics and Applications*. Academic Press Inc., 1993.
- [50] J. Orton and P. Blood, *The Electrical Characterization of Semiconductors: Measurement of Minority Carrier Properties*. Academic Press Inc., 1990.
- [51] M. Kamińska and M. Skowroński, “Identification of the 0.82-eV Electron Trap EL2 in GaAs as an Isolated Antisite Arsenic Defect,” *Physical review letters*, vol. 55, no. 20, pp. 2204–2207, 1985.

- [52] M. A. Zaidi, H. Maaref, and J. C. Bourgoin, “Minority carrier capture cross section of the EL2 defect in GaAs,” *Applied Physics Letters*, vol. 61, no. 20, p. 2452, 1992.
- [53] M. Hanson, S. Bank, J. Zide, J. Zimmerman, and A. Gossard, “Controlling electronic properties of epitaxial nanocomposites of dissimilar materials,” *Journal of Crystal Growth*, vol. 301-302, pp. 4–9, Apr. 2007.
- [54] T. Kruczek, R. Leyman, D. Carnegie, N. Bazieva, G. Erbert, S. Schulz, C. Rendon, S. Reynolds, and E. U. Rafailov, “Continuous wave terahertz radiation from an InAs/GaAs quantum-dot photomixer device,” *Applied Physics Letters*, vol. 101, no. 8, p. 081114, 2012.
- [55] J. M. O. Zide, J.-H. Bahk, R. Singh, M. Zebarjadi, G. Zeng, H. Lu, J. P. Feser, D. Xu, S. L. Singer, Z. X. Bian, A. Majumdar, J. E. Bowers, A. Shakouri, and A. C. Gossard, “High efficiency semimetal/semiconductor nanocomposite thermoelectric materials,” *Journal of Applied Physics*, vol. 108, no. 12, p. 123702, 2010.
- [56] W. Kim, S. L. Singer, A. Majumdar, D. Vashaee, Z. Bian, A. Shakouri, G. Zeng, J. E. Bowers, J. M. O. Zide, and A. C. Gossard, “Cross-plane lattice and electronic thermal conductivities of ErAs:InGaAsInGaAlAs superlattices,” *Applied Physics Letters*, vol. 88, no. 24, p. 242107, 2006.
- [57] S. Andrews and A. Armitage, “Optimization of photoconducting receivers for THz spectroscopy,” *Physics in medicine . . .*, vol. 3705, 2002.
- [58] J. K. Kawasaki, R. Timm, K. T. Delaney, E. Lundgren, A. Mikkelsen, and C. J. Palmström, “Local density of states and interface effects in semimetallic ErAs nanoparticles embedded in GaAs,” *Physical Review Letters*, vol. 107, p. 036806, July 2011.
- [59] E. Brown, A. Bacher, D. Driscoll, M. Hanson, C. Kadow, and A. Gossard, “Evidence for a Strong Surface-Plasmon Resonance on ErAs Nanoparticles in GaAs,” *Physical Review Letters*, vol. 90, p. 077403, Feb. 2003.
- [60] M. Griebel, J. H. Smet, D. C. Driscoll, J. Kuhl, C. A. Diez, N. Freytag, C. Kadow, A. C. Gossard, and K. Von Klitzing, “Tunable subpicosecond optoelectronic transduction in superlattices of self-assembled ErAs nanoislands,” *Nature materials*, vol. 2, pp. 122–6, Feb. 2003.
- [61] A. M. Crook, H. P. Nair, and S. R. Bank, “Surface segregation effects of erbium in GaAs growth and their implications for optical devices containing ErAs nanostructures,” *Applied Physics Letters*, vol. 98, no. 12, p. 121108, 2011.
- [62] X. L. Zhou, Y. H. Chen, X. L. Ye, B. Xu, and Z. G. Wang, “Abnormal temperature dependent photoluminescence of excited states of InAs/GaAs quantum dots: Carrier exchange between excited states and ground states,” *Journal of Applied Physics*, vol. 109, no. 11, p. 113540, 2011.

- [63] K. J. Williams, W. A. Tisdale, K. S. Leschkies, G. Haugstad, D. J. Norris, E. S. Aydil, and X.-Y. Zhu, “Strong electronic coupling in two-dimensional assemblies of colloidal PbSe quantum dots,” *ACS nano*, vol. 3, pp. 1532–8, June 2009.
- [64] T. Franzl, T. A. Klar, S. Schietinger, A. L. Rogach, and J. Feldmann, “Exciton Recycling in Graded Gap Nanocrystal Structures,” *Nano Letters*, vol. 4, pp. 1599–1603, Sept. 2004.
- [65] R. Bose, J. McMillan, J. Gao, and K. Rickey, “Temperature-tuning of near-infrared monodisperse quantum dot solids at 1.5 m for controllable Forster energy transfer,” *Nano Letters*, vol. 8, no. 7, pp. 2006–2011, 2008.
- [66] X. Ma, F. Xu, J. Benavides, and S. G. Cloutier, “High performance hybrid near-infrared LEDs using benzenedithiol cross-linked PbS colloidal nanocrystals,” *Organic Electronics*, vol. 13, pp. 525–531, Mar. 2012.
- [67] J. M. Luther, M. Law, Q. Song, C. L. Perkins, M. C. Beard, and A. J. Nozik, “Structural, optical, and electrical properties of self-assembled films of PbSe nanocrystals treated with 1,2-ethanedithiol,” *ACS nano*, vol. 2, pp. 271–80, Feb. 2008.
- [68] X. Wang, X. Ren, K. Kahen, M. A. Hahn, M. Rajeswaran, S. Maccagnano-Zacher, J. Silcox, G. E. Cragg, A. L. Efros, and T. D. Krauss, “Non-blinking semiconductor nanocrystals,” *Nature*, vol. 459, pp. 686–689, Jan. 2009.
- [69] C. Wang, C. Chen, Y. Chen, C. Wei, C. Lai, M. Ho, P. Chou, and M. Hofmann, “Surface plasmon enhanced energy transfer between type I CdSe/ZnS and type II CdSe/ZnTe quantum dots,” *Applied Physics Letters*, vol. 96, p. 71906, 2010.
- [70] D. Gross, A. S. Sussha, T. A. Klar, E. Da Como, A. L. Rogach, and J. Feldmann, “Charge separation in type II tunneling structures of close-packed CdTe and CdSe nanocrystals,” *Nano letters*, vol. 8, pp. 1482–5, May 2008.

Appendix A  
MATHEMATICA CODE FOR DEBUF MODEL

# Debuf Model

---

## Constants (for GaAs)

```
In[1]:= vthn = 4.4 * 10^7; (*cm/sec for GaAs*)
vthp = 1.8 * 10^7; (*cm/sec for GaAs*)
Et = 0.85; (*eV*)
Ev = 0;
Ec = 1.424;
T = 300;

σn = 5 * 10^-15;
σp = 5.5 * 10^-17;
Nc = 4.37 * 10^17; (*cm^2 for GaAs*)
Nv = 1.83 * 10^15 * T^(3/2); (*cm^2*)
B = 1.788 * 10^-10; (*cm^3/sec*)
C1 = 1.6 * 10^-29; (*cm^6/sec for GaAs*)
kT = 0.025852; (*eV*)

ni = 2.1 * 10^6; (*cm^-3*)
Na = 1 * 10^15; (*cm^-3*)
p0 = Na; (*equalibrium carrier concentrations*)
n0 = ni^2 / Na; (*equalibrium carrier concentrations*)
us = 10^6; (*seconds to microseconds*)
Cn = vthn * σn;
Cp = vthp * σp;
(*Nt=7*10^14;*) (*initial value of Nt, will change later*)

n1 = Nc * Exp[-(Ec - Et) / kT];
p1 = Nv * Exp[-(Et - Ev) / kT];

α0[Nt_] := Cp * Nt * (p1 / (p0 + p1) + p0 / Nt);
β0[Nt_] := Cp * Nt * (p0 + p1) / Nt;
γ0[Nt_] := Cn * Nt * (n1 / (n0 + n1) + n0 / Nt);
σ0[Nt_] := Cn * Nt * (n0 + n1) / Nt;
```

## Formulas

In[17]= (\*assuming  $\Delta n = \Delta p$ \*)

$$\phi[\Delta n_, Nt_] := \left(1 + \frac{Nt}{\Delta n}\right);$$

(\*xxxxxxxx\*)

$$\eta n[\Delta n_, Nt_] := ((\phi[\Delta n, Nt] * \alpha 0[Nt] - \beta 0[Nt]) - (\phi[\Delta n, Nt] * \gamma 0[Nt] - (\phi[\Delta n, Nt])^2 * \sigma 0[Nt])) / (\phi[\Delta n, Nt] * \Delta n * (1 - \phi[\Delta n, Nt]) (Cn + Cp));$$

$$\eta p[\Delta n_, Nt_] := \eta n[\Delta n, Nt] * \left(1 + \frac{Nt}{\Delta n}\right);$$

(\*xxxxxxxx\*)

$$\alpha[\Delta n_, \Delta p_, Nt_] := Cp * Nt * \left(\frac{p1}{p0 + p1} + \frac{p0 + p1}{Nt} + \frac{\eta p[\Delta n, Nt] * \Delta p}{Nt}\right);$$

$$\beta[\Delta n_, Nt_] := Cp * Nt * \left(\frac{p0 + p1}{Nt} + \frac{\eta p[\Delta n, Nt] * \Delta n}{Nt}\right);$$

$$\gamma[\Delta n_, Nt_] := Cn * Nt * \left(\frac{n1}{n0 + n1} + \frac{n0 + n1}{Nt} + \frac{\eta n[\Delta n, Nt] * \Delta n}{Nt}\right);$$

$$\sigma[\Delta n_, \Delta p_, Nt_] := Cn * Nt * \left(\frac{n0 + n1}{Nt} + \frac{\eta n[\Delta n, Nt] * \Delta p}{Nt}\right);$$

$$\lambda 3[\Delta n_, \Delta p_, Nt_] :=$$

$$\frac{1}{2} (\alpha[\Delta n, \Delta p, Nt] + \gamma[\Delta n, Nt] - (\alpha[\Delta n, \Delta p, Nt]^2 - 2 * \alpha[\Delta n, \Delta p, Nt] * \gamma[\Delta n, Nt] + \gamma[\Delta n, Nt]^2 + 4 * \beta[\Delta n, Nt] * \sigma[\Delta n, \Delta p, Nt]))^{(1/2)}$$

$$\lambda 4[\Delta n_, \Delta p_, Nt_] := \frac{1}{2} (\alpha[\Delta n, \Delta p, Nt] + \gamma[\Delta n, Nt] + (\alpha[\Delta n, \Delta p, Nt]^2 - 2 * \alpha[\Delta n, \Delta p, Nt] * \gamma[\Delta n, Nt] + \gamma[\Delta n, Nt]^2 + 4 * \beta[\Delta n, Nt] * \sigma[\Delta n, \Delta p, Nt]))^{(1/2)}$$

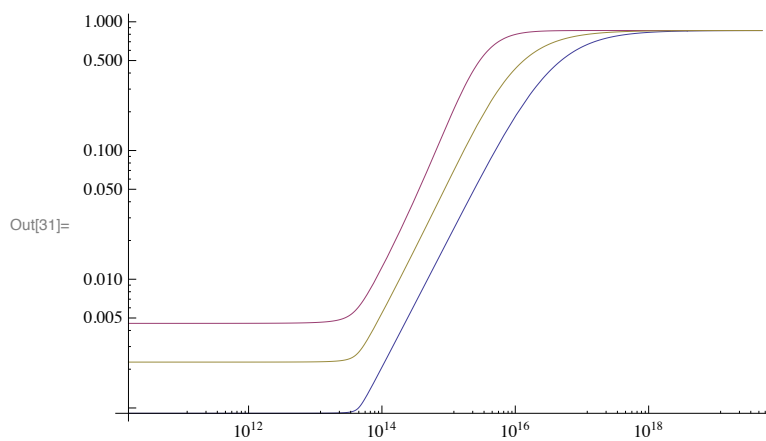
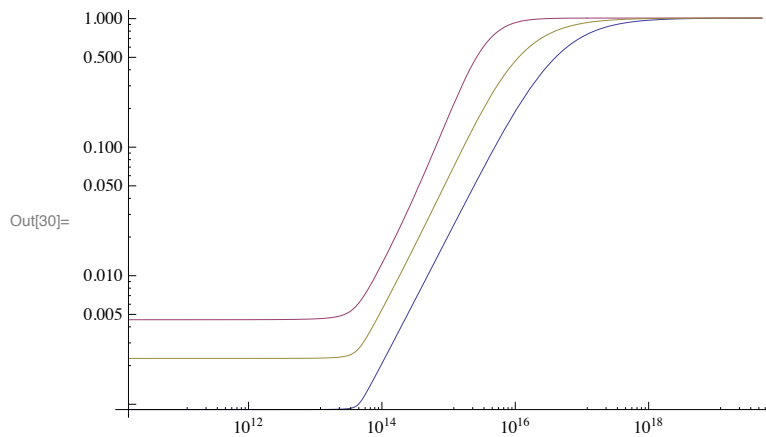
$$\tau 3[\Delta n_, \Delta p_, Nt_] := 1 / \lambda 3[\Delta n, \Delta p, Nt];$$

$$\tau 4[\Delta n_, \Delta p_, Nt_] := 1 / \lambda 4[\Delta n, \Delta p, Nt];$$

$$\tau T[\Delta n_, \Delta p_, Nt_] := \left(\frac{1}{\tau 3[\Delta n, \Delta p, Nt]} + C1 * p0^2 + B * p0\right)^{-1};$$

## Outputs

```
In[29]:= Δp = 10^16;
LogLogPlot[{τ3[Δn, Δp, 5 * 10^15] * us, τ3[Δn, Δp, 1 * 10^15] * us, τ3[Δn, Δp, 2 * 10^15] * us},
{Δn, 5 * 10^9.5, 5 * 10^19}]
(*LogLogPlot[{λ3[Δn], λ4[Δn]}, {Δn, 5 * 10^9.5, 5 * 10^16}]*)
LogLogPlot[{τT[Δn, Δp, 5 * 10^15] * us, τT[Δn, Δp, 1 * 10^15] * us, τT[Δn, Δp, 2 * 10^15] * us},
{Δn, 5 * 10^9.5, 5 * 10^19}]
```



### ■ Include Data

```
In[68]:= h = 6.626 * 10^-34; (*m^2 kg/s^2 K*)
λ = 800 * 10^-9; (*m*)
c = 3 * 10^8; (*m*)

P = (1 * 10^-3); (*W*)
RR = 1.52 * 10^5; (*repetition rate Hz (1/s)*)

(*Calculating spot size*)
LP = 0.498; (*W*)
PD = 80; (*W/cm^2*)
SpZ = (LP / PD) * (10^-4);
r = Sqrt[(SpZ) / Pi]; (*beam diameter in m*)
```

```

(*get the beam waist focused through the lens*)
L = 800 * 10^-9; (*m*)
F = 250 * 10^-3; (*m*)
d = r;
ww = N[(4 * L / Pi) * (F / d) / 2];

(*get the area of the ellipse that hits the sample*)
theta = Pi / 3; (*estimated 60 deg angle*)
b = ww * Cos[theta]; (*minor axis of ellipse*)
Area = Pi * b * ww; (*focused area based on lens and angle*)

SpotArea = SpZ;
PE = P / RR; (*P = Pave*)
EN = h * c / λ;

PpP = PE / EN; (*photons per pulse*)
Ξ = PpP / (Area * 10^4); (*photon flux cm^-2*)

α1 = 13267; (*cm^-1*)

I1 = Ξ * Exp[-α1 * x];
Ξ = (10^4) * ∫_0^{10*10^-3} (1 - 0.32) I1 dx;
φ1 = Ξ * (1); (*NDO*)
φ2 = Ξ * (0.85896); (*NDO.1*)
φ3 = Ξ * (0.655491); (*NDO.2*)
φ4 = Ξ * (0.563006); (*NDO.3*)
φ5 = Ξ * (0.369942); (*NDO.4*)
φ6 = Ξ * (0.316228); (*NDO.5*)
φ7 = Ξ * (0.100578); (*ND1*)
a = 1;

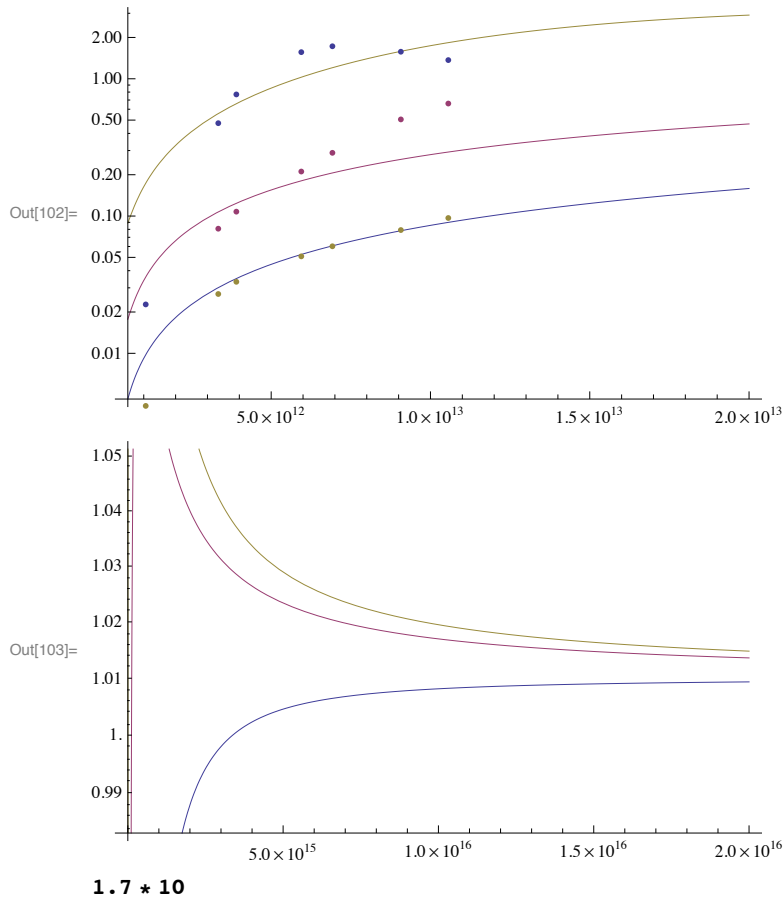
Data716 = List[{φ1 * a, 1.368}, {φ2 * a, 1.574}, {φ3 * a, 1.725},
  {φ4 * a, 1.563}, {φ5 * a, 0.769}, {φ6 * a, 0.4748}, {φ7 * a, 0.02271}];
Data917 = List[{φ1 * a, 0.6601}, {φ2 * a, 0.5058}, {φ3 * a, 0.2888},
  {φ4 * a, 0.211}, {φ5 * a, 0.10763}, {φ6 * a, 0.08088}, {φ7 * a, 0.00103}];
Data992 = List[{φ1 * a, 0.09677}, {φ2 * a, 0.07907}, {φ3 * a, 0.06023},
  {φ4 * a, 0.05086}, {φ5 * a, 0.03319}, {φ6 * a, 0.02705}, {φ7 * a, 0.00414}];

(*ListLogPlot[{Data716,Data917,Data992},
  PlotRange -> {0,4},PlotStyle ->{PointSize[Medium]},Frame -> True]*)
(*ListLogLogPlot[{Data716,Data917,Data992},PlotRange -> Automatic]

LogLogPlot[{τ3[x,Δp,4*10^13]*us},{x,5*10^12,1*10^16}]

Show[LogLogPlot[{τ3[x,Δp1,7.3*10^15]*us,τ3[x,Δp2,2*10^15]*us,τ3[x,Δp3,7.3*10^14]*us},
  {x,5*10^11,1*10^15},PlotRange->Automatic],
  ListLogLogPlot[{Data716,Data917,Data992}]]*)
Δp1 = 1 * 10^14;
Δp2 = 1 * 10^14;
Δp3 = 1 * 10^14;
Nt1 = 1.1 * 10^15;
Nt2 = 3 * 10^14;
Nt3 = 7.6 * 10^13;
Show[LogPlot[{τ3[x, Δp1, Nt1] * us, τ3[x, Δp2, Nt2] * us, τ3[x, Δp3, Nt3] * us},
  {x, 5 * 10^11, 2 * 10^13}, PlotRange -> Automatic],
  ListLogPlot[{Data716, Data917, Data992}]]]
LogPlot[{τ3[Δn, Δp1, Nt1] * us, τ3[Δn, Δp2, Nt2] * us, τ3[Δn, Δp3, Nt3] * us},
  {Δn, 5 * 10^11, 2 * 10^16}]

```



### ■ Standard Deviation and Least Squares Minimization

```

In[120]:= Data7162 = List[1.368, 1.574, 1.725, 1.563, 0.769, 0.4748, 0.02271];
Nt1 = 3 * 10^15;
Modell = List[τ3[φ1 * a, Nt1] * us, τ3[φ2 * a, Nt1] * us, τ3[φ3 * a, Nt1] * us,
  τ3[φ4 * a, Nt1] * us, τ3[φ5 * a, Nt1] * us, τ3[φ6 * a, Nt1] * us, τ3[φ7 * a, Nt1] * us];
Var = (Data7162 - Modell)^2;
Svar = 0;
For[i = 0, i < 7, i++; SVar = Svar + Var[[i]]];
SVar;
Sqrt[SVar / 7];

```

```

In[128]:= min = 5 * 10^11;
max = 5 * 10^14;
S716 = {{0, 0}};
max / (5 * 10^10)
(*For S716*)

For[f = min, f < max, f += 5 * 10^10; S716 = Append[S716, {f, τ3[f, Δp3, Nt3] * us}]]
Export["S716-6.dat", S716]
S716

(*For S917*)
S917 = {{0, 0}}
For[f = min, f < max, f += 5 * 10^10; S917 = Append[S917, {f, τ3[f, Δp2, Nt2] * us}]]
Export["S917-6.dat", S917]
S917

(*For S992*)
S992 = {{0, 0}}
For[f = min, f < max, f += 5 * 10^10; S992 = Append[S992, {f, τ3[f, Δp1, Nt1] * us}]]
Export["S992-6.dat", S992]
S992

```

Out[131]= 10 000

Out[133]= S716-6.dat

A very large output was generated. Here is a sample of it:

Out[134]=

```

{{0, 0}, {550 000 000 000, 0.0955583}, {600 000 000 000, 0.102577},
{650 000 000 000, 0.109826}, {700 000 000 000, 0.11724}, {750 000 000 000, 0.124781},
<<9980>>, {499 800 000 000 000, 1.20253}, {499 850 000 000 000, 1.20251},
{499 900 000 000 000, 1.2025}, {499 950 000 000 000, 1.20248}, {500 000 000 000 000, 1.20246}}

```

Show Less Show More Show Full Output Set Size Limit...

Out[135]= {{0, 0}}

Out[137]= S917-6.dat

A very large output was generated. Here is a sample of it:

Out[138]=

```

{{0, 0}, {550 000 000 000, 0.0192073}, {600 000 000 000, 0.0207956},
{650 000 000 000, 0.02242}, {700 000 000 000, 0.0240599}, {750 000 000 000, 0.0257068},
<<9980>>, {499 800 000 000 000, 1.08142}, {499 850 000 000 000, 1.08141},
{499 900 000 000 000, 1.08141}, {499 950 000 000 000, 1.08141}, {500 000 000 000 000, 1.08141}}

```

Show Less Show More Show Full Output Set Size Limit...

Out[139]= {{0, 0}}

Out[141]= S992-6.dat

**Appendix B**  
**RIGHTS AND PERMISSIONS**

## AIP PUBLISHING LLC LICENSE TERMS AND CONDITIONS

Nov 13, 2014

**All payments must be made in full to CCC. For payment instructions, please see information listed at the bottom of this form.**

License Number	3507130841850
Order Date	Nov 13, 2014
Publisher	AIP Publishing LLC
Publication	Applied Physics Letters
Article Title	Carrier transfer from InAs quantum dots to ErAs metal nanoparticles
Author	C. R. Haughn,E. H. Steenbergen,L. J. Bissell, et al.
Online Publication Date	Sep 12, 2014
Volume number	105
Issue number	10
Type of Use	Thesis/Dissertation
Requestor type	Author (original article)
Format	Print and electronic
Portion	Figure/Table
Number of figures/tables	5
Title of your thesis / dissertation	Energy Transport in Nanostructured Materials
Expected completion date	Dec 2014
Estimated size (number of pages)	115
Total	0.00 USD

### Terms and Conditions

AIP Publishing LLC -- Terms and Conditions: Permissions Uses

AIP Publishing LLC ("AIPP") hereby grants to you the non-exclusive right and license to use and/or distribute the Material according to the use specified in your order, on a one-time basis, for the specified term, with a maximum distribution equal to the number that you have ordered. Any links or other content accompanying the Material are not the subject of this license.

1. You agree to include the following copyright and permission notice with the reproduction of the Material: "Reprinted with permission from [FULL CITATION]. Copyright [PUBLICATION YEAR], AIP Publishing LLC." For an article, the copyright and permission notice must be printed on the first page of the article or book chapter. For photographs, covers, or tables, the copyright and permission notice may appear with the Material, in a footnote, or in the reference list.
2. If you have licensed reuse of a figure, photograph, cover, or table, it is your responsibility to ensure that the material is original to AIPP and does not contain the copyright of another entity, and that the copyright notice of the figure, photograph, cover, or table does not

- indicate that it was reprinted by AIPP, with permission, from another source. Under no circumstances does AIPP, purport or intend to grant permission to reuse material to which it does not hold copyright.
3. You may not alter or modify the Material in any manner. You may translate the Material into another language only if you have licensed translation rights. You may not use the Material for promotional purposes. AIPP reserves all rights not specifically granted herein.
  4. The foregoing license shall not take effect unless and until AIPP or its agent, Copyright Clearance Center, receives the Payment in accordance with Copyright Clearance Center Billing and Payment Terms and Conditions, which are incorporated herein by reference.
  5. AIPP or the Copyright Clearance Center may, within two business days of granting this license, revoke the license for any reason whatsoever, with a full refund payable to you. Should you violate the terms of this license at any time, AIPP, AIP Publishing LLC, or Copyright Clearance Center may revoke the license with no refund to you. Notice of such revocation will be made using the contact information provided by you. Failure to receive such notice will not nullify the revocation.
  6. AIPP makes no representations or warranties with respect to the Material. You agree to indemnify and hold harmless AIPP, AIP Publishing LLC, and their officers, directors, employees or agents from and against any and all claims arising out of your use of the Material other than as specifically authorized herein.
  7. The permission granted herein is personal to you and is not transferable or assignable without the prior written permission of AIPP. This license may not be amended except in a writing signed by the party to be charged.
  8. If purchase orders, acknowledgments or check endorsements are issued on any forms containing terms and conditions which are inconsistent with these provisions, such inconsistent terms and conditions shall be of no force and effect. This document, including the CCC Billing and Payment Terms and Conditions, shall be the entire agreement between the parties relating to the subject matter hereof.

This Agreement shall be governed by and construed in accordance with the laws of the State of New York. Both parties hereby submit to the jurisdiction of the courts of New York County for purposes of resolving any disputes that may arise hereunder.

**Questions? [customercare@copyright.com](mailto:customercare@copyright.com) or +1-855-239-3415 (toll free in the US) or +1-978-646-2777.**

**Gratis licenses (referencing \$0 in the Total field) are free. Please retain this printable license for your reference. No payment is required.**

---

---

## AIP PUBLISHING LLC LICENSE TERMS AND CONDITIONS

Nov 13, 2014

**All payments must be made in full to CCC. For payment instructions, please see information listed at the bottom of this form.**

License Number	3507131304670
Order Date	Nov 13, 2014
Publisher	AIP Publishing LLC
Publication	Applied Physics Letters
Article Title	Quantification of trap state densities in GaAs heterostructures grown at varying rates using intensity-dependent time resolved photoluminescence
Author	C. R. Haughn, K. J. Schmieder, J. M. O. Zide, et al.
Online Publication Date	May 10, 2013
Volume number	102
Issue number	18
Type of Use	Thesis/Dissertation
Requestor type	Author (original article)
Format	Print and electronic
Portion	Figure/Table
Number of figures/tables	3
Title of your thesis / dissertation	Energy Transport in Nanostructured Materials
Expected completion date	Dec 2014
Estimated size (number of pages)	115
Total	0.00 USD

### Terms and Conditions

#### AIP Publishing LLC -- Terms and Conditions: Permissions Uses

AIP Publishing LLC ("AIPP") hereby grants to you the non-exclusive right and license to use and/or distribute the Material according to the use specified in your order, on a one-time basis, for the specified term, with a maximum distribution equal to the number that you have ordered. Any links or other content accompanying the Material are not the subject of this license.

1. You agree to include the following copyright and permission notice with the reproduction of the Material: "Reprinted with permission from [FULL CITATION]. Copyright [PUBLICATION YEAR], AIP Publishing LLC." For an article, the copyright and permission notice must be printed on the first page of the article or book chapter. For photographs, covers, or tables, the copyright and permission notice may appear with the Material, in a footnote, or in the reference list.
2. If you have licensed reuse of a figure, photograph, cover, or table, it is your responsibility

to ensure that the material is original to AIPP and does not contain the copyright of another entity, and that the copyright notice of the figure, photograph, cover, or table does not indicate that it was reprinted by AIPP, with permission, from another source. Under no circumstances does AIPP, purport or intend to grant permission to reuse material to which it does not hold copyright.

3. You may not alter or modify the Material in any manner. You may translate the Material into another language only if you have licensed translation rights. You may not use the Material for promotional purposes. AIPP reserves all rights not specifically granted herein.
4. The foregoing license shall not take effect unless and until AIPP or its agent, Copyright Clearance Center, receives the Payment in accordance with Copyright Clearance Center Billing and Payment Terms and Conditions, which are incorporated herein by reference.
5. AIPP or the Copyright Clearance Center may, within two business days of granting this license, revoke the license for any reason whatsoever, with a full refund payable to you. Should you violate the terms of this license at any time, AIPP, AIP Publishing LLC, or Copyright Clearance Center may revoke the license with no refund to you. Notice of such revocation will be made using the contact information provided by you. Failure to receive such notice will not nullify the revocation.
6. AIPP makes no representations or warranties with respect to the Material. You agree to indemnify and hold harmless AIPP, AIP Publishing LLC, and their officers, directors, employees or agents from and against any and all claims arising out of your use of the Material other than as specifically authorized herein.
7. The permission granted herein is personal to you and is not transferable or assignable without the prior written permission of AIPP. This license may not be amended except in a writing signed by the party to be charged.
8. If purchase orders, acknowledgments or check endorsements are issued on any forms containing terms and conditions which are inconsistent with these provisions, such inconsistent terms and conditions shall be of no force and effect. This document, including the CCC Billing and Payment Terms and Conditions, shall be the entire agreement between the parties relating to the subject matter hereof.

This Agreement shall be governed by and construed in accordance with the laws of the State of New York. Both parties hereby submit to the jurisdiction of the courts of New York County for purposes of resolving any disputes that may arise hereunder.

**Questions? [customercare@copyright.com](mailto:customercare@copyright.com) or +1-855-239-3415 (toll free in the US) or +1-978-646-2777.**

**Gratis licenses (referencing \$0 in the Total field) are free. Please retain this printable license for your reference. No payment is required.**

---

---

]

## AIP PUBLISHING LLC LICENSE TERMS AND CONDITIONS

Nov 13, 2014

**All payments must be made in full to CCC. For payment instructions, please see information listed at the bottom of this form.**

License Number	3507131405340
Order Date	Nov 13, 2014
Publisher	AIP Publishing LLC
Publication	Applied Physics Letters
Article Title	Charge-transfer dynamics in multilayered PbS and PbSe quantum dot architectures
Author	F. Xu,C. R. Haughn,X. Ma, et al.
Online Publication Date	Feb 4, 2014
Volume number	104
Issue number	5
Type of Use	Thesis/Dissertation
Requestor type	Author (original article)
Format	Print and electronic
Portion	Figure/Table
Number of figures/tables	2
Title of your thesis / dissertation	Energy Transport in Nanostructured Materials
Expected completion date	Dec 2014
Estimated size (number of pages)	115
Total	0.00 USD

### Terms and Conditions

#### AIP Publishing LLC -- Terms and Conditions: Permissions Uses

AIP Publishing LLC ("AIPP") hereby grants to you the non-exclusive right and license to use and/or distribute the Material according to the use specified in your order, on a one-time basis, for the specified term, with a maximum distribution equal to the number that you have ordered. Any links or other content accompanying the Material are not the subject of this license.

1. You agree to include the following copyright and permission notice with the reproduction of the Material: "Reprinted with permission from [FULL CITATION]. Copyright [PUBLICATION YEAR], AIP Publishing LLC." For an article, the copyright and permission notice must be printed on the first page of the article or book chapter. For photographs, covers, or tables, the copyright and permission notice may appear with the Material, in a footnote, or in the reference list.
2. If you have licensed reuse of a figure, photograph, cover, or table, it is your responsibility to ensure that the material is original to AIPP and does not contain the copyright of another

entity, and that the copyright notice of the figure, photograph, cover, or table does not indicate that it was reprinted by AIPP, with permission, from another source. Under no circumstances does AIPP, purport or intend to grant permission to reuse material to which it does not hold copyright.

3. You may not alter or modify the Material in any manner. You may translate the Material into another language only if you have licensed translation rights. You may not use the Material for promotional purposes. AIPP reserves all rights not specifically granted herein.
4. The foregoing license shall not take effect unless and until AIPP or its agent, Copyright Clearance Center, receives the Payment in accordance with Copyright Clearance Center Billing and Payment Terms and Conditions, which are incorporated herein by reference.
5. AIPP or the Copyright Clearance Center may, within two business days of granting this license, revoke the license for any reason whatsoever, with a full refund payable to you. Should you violate the terms of this license at any time, AIPP, AIP Publishing LLC, or Copyright Clearance Center may revoke the license with no refund to you. Notice of such revocation will be made using the contact information provided by you. Failure to receive such notice will not nullify the revocation.
6. AIPP makes no representations or warranties with respect to the Material. You agree to indemnify and hold harmless AIPP, AIP Publishing LLC, and their officers, directors, employees or agents from and against any and all claims arising out of your use of the Material other than as specifically authorized herein.
7. The permission granted herein is personal to you and is not transferable or assignable without the prior written permission of AIPP. This license may not be amended except in a writing signed by the party to be charged.
8. If purchase orders, acknowledgments or check endorsements are issued on any forms containing terms and conditions which are inconsistent with these provisions, such inconsistent terms and conditions shall be of no force and effect. This document, including the CCC Billing and Payment Terms and Conditions, shall be the entire agreement between the parties relating to the subject matter hereof.

This Agreement shall be governed by and construed in accordance with the laws of the State of New York. Both parties hereby submit to the jurisdiction of the courts of New York County for purposes of resolving any disputes that may arise hereunder.

**Questions? [customercare@copyright.com](mailto:customercare@copyright.com) or +1-855-239-3415 (toll free in the US) or +1-978-646-2777.**

**Gratis licenses (referencing \$0 in the Total field) are free. Please retain this printable license for your reference. No payment is required.**

---

---

## AIP PUBLISHING LLC LICENSE TERMS AND CONDITIONS

Nov 13, 2014

**All payments must be made in full to CCC. For payment instructions, please see information listed at the bottom of this form.**

License Number	3507141415837
Order Date	Nov 13, 2014
Publisher	AIP Publishing LLC
Publication	Applied Physics Letters
Article Title	Near-infrared absorption and semimetal-semiconductor transition in 2nm ErAs nanoparticles embedded in GaAs and AlAs
Author	Michael A. Scarpulla, Joshua M. O. Zide, James M. LeBeau, et al.
Online Publication Date	May 1, 2008
Volume number	92
Issue number	17
Type of Use	Thesis/Dissertation
Requestor type	Student
Format	Print and electronic
Portion	Figure/Table
Number of figures/tables	1
Title of your thesis / dissertation	Energy Transport in Nanostructured Materials
Expected completion date	Dec 2014
Estimated size (number of pages)	115
Total	0.00 USD

### Terms and Conditions

#### AIP Publishing LLC -- Terms and Conditions: Permissions Uses

AIP Publishing LLC ("AIPP") hereby grants to you the non-exclusive right and license to use and/or distribute the Material according to the use specified in your order, on a one-time basis, for the specified term, with a maximum distribution equal to the number that you have ordered. Any links or other content accompanying the Material are not the subject of this license.

1. You agree to include the following copyright and permission notice with the reproduction of the Material: "Reprinted with permission from [FULL CITATION]. Copyright [PUBLICATION YEAR], AIP Publishing LLC." For an article, the copyright and permission notice must be printed on the first page of the article or book chapter. For photographs, covers, or tables, the copyright and permission notice may appear with the Material, in a footnote, or in the reference list.
2. If you have licensed reuse of a figure, photograph, cover, or table, it is your responsibility to ensure that the material is original to AIPP and does not contain the copyright of another

entity, and that the copyright notice of the figure, photograph, cover, or table does not indicate that it was reprinted by AIPP, with permission, from another source. Under no circumstances does AIPP, purport or intend to grant permission to reuse material to which it does not hold copyright.

3. You may not alter or modify the Material in any manner. You may translate the Material into another language only if you have licensed translation rights. You may not use the Material for promotional purposes. AIPP reserves all rights not specifically granted herein.
4. The foregoing license shall not take effect unless and until AIPP or its agent, Copyright Clearance Center, receives the Payment in accordance with Copyright Clearance Center Billing and Payment Terms and Conditions, which are incorporated herein by reference.
5. AIPP or the Copyright Clearance Center may, within two business days of granting this license, revoke the license for any reason whatsoever, with a full refund payable to you. Should you violate the terms of this license at any time, AIPP, AIP Publishing LLC, or Copyright Clearance Center may revoke the license with no refund to you. Notice of such revocation will be made using the contact information provided by you. Failure to receive such notice will not nullify the revocation.
6. AIPP makes no representations or warranties with respect to the Material. You agree to indemnify and hold harmless AIPP, AIP Publishing LLC, and their officers, directors, employees or agents from and against any and all claims arising out of your use of the Material other than as specifically authorized herein.
7. The permission granted herein is personal to you and is not transferable or assignable without the prior written permission of AIPP. This license may not be amended except in a writing signed by the party to be charged.
8. If purchase orders, acknowledgments or check endorsements are issued on any forms containing terms and conditions which are inconsistent with these provisions, such inconsistent terms and conditions shall be of no force and effect. This document, including the CCC Billing and Payment Terms and Conditions, shall be the entire agreement between the parties relating to the subject matter hereof.

This Agreement shall be governed by and construed in accordance with the laws of the State of New York. Both parties hereby submit to the jurisdiction of the courts of New York County for purposes of resolving any disputes that may arise hereunder.

**Questions? [customercare@copyright.com](mailto:customercare@copyright.com) or +1-855-239-3415 (toll free in the US) or +1-978-646-2777.**

**Gratis licenses (referencing \$0 in the Total field) are free. Please retain this printable license for your reference. No payment is required.**

---

---



RightsLink®

[Home](#)[Account Info](#)[Help](#)

**Title:** Efficient Exciton Funneling in Cascaded PbS Quantum Dot Superstructures

**Author:** Fan Xu, Xin Ma, Chelsea R. Haughn, et al

**Publication:** ACS Nano

**Publisher:** American Chemical Society

**Date:** Dec 1, 2011

Copyright © 2011, American Chemical Society

Logged in as:  
Chelsea Haughn

[LOGOUT](#)

### PERMISSION/LICENSE IS GRANTED FOR YOUR ORDER AT NO CHARGE

This type of permission/license, instead of the standard Terms & Conditions, is sent to you because no fee is being charged for your order. Please note the following:

- Permission is granted for your request in both print and electronic formats, and translations.
- If figures and/or tables were requested, they may be adapted or used in part.
- Please print this page for your records and send a copy of it to your publisher/graduate school.
- Appropriate credit for the requested material should be given as follows: "Reprinted (adapted) with permission from (COMPLETE REFERENCE CITATION). Copyright (YEAR) American Chemical Society." Insert appropriate information in place of the capitalized words.
- One-time permission is granted only for the use specified in your request. No additional uses are granted (such as derivative works or other editions). For any other uses, please submit a new request.

If credit is given to another source for the material you requested, permission must be obtained from that source.

[BACK](#)[CLOSE WINDOW](#)

Copyright © 2014 [Copyright Clearance Center, Inc.](#) All Rights Reserved. [Privacy statement.](#)  
Comments? We would like to hear from you. E-mail us at [customercare@copyright.com](mailto:customercare@copyright.com)